Online Condition Monitoring of Stator Winding Insulation State of Electric Machines in Electrified Vehicles

Ashutosh Patel

A Thesis

In the Department of

Electrical and Computer Engineering

Presented in Partial Fulfillment of the Requirements

For the Degree of

Doctor of Philosophy (Electrical and Computer Engineering) at

Concordia University

Montreal, Quebec, Canada

August 2024

CONCORDIA UNIVERSITY

SCHOOL OF GRADUATE STUDIES

This is to certify that the thesis prepared

By: Ashutosh Patel

Entitled: Online Condition Monitoring of Stator Winding Insulation State of Electric Machines in Electrified Vehicles and submitted in partial fulfillment of the requirements for the degree of

Doctor of Philosophy (Electrical and Computer Engineering)

complies with the regulations of the University and meets the accepted standards with respect to originality and quality.

Signed by the final examining committee:

_____Chair
Dr. Luis Amador

_____External Examiner
Dr. Xiaozhe Wang

_____Arm's Length Examiner
Dr. Chunjiang An

_____Examiner
Dr. Pragasen Pillay

_____Examiner
Dr. Mohsen Ghafouri

_____Thesis Supervisor
Dr. Chunyan Lai

Approved by: _____

Dr. Jun Cai, Graduate Program Director

August 6, 2024

_____

Dr. Mourad Debbabi, Dean,
Gina Cody School of Engineering and Computer Science

Abstract

Online Condition Monitoring of Stator Winding Insulation State of Electric Machines in Electrified Vehicles

Ashutosh Patel, Ph.D.

Concordia University, 2024

Electrified vehicles commonly use traction machines powered by voltage source inverters (VSI) for efficient speed and torque control. However, short circuit faults and insulation failures remain prevalent, accounting for approximately 30% of motor failures. Given the uncertainties surrounding insulation degradation, detecting degradations of insulation in an early stage can help prevent major failures. Therefore, this Ph.D. research focuses on online monitoring of electrical machine's winding insulation degradation.

A comprehensive review of literature revealed certain research gaps. The first one is on selection of the most effective insulation degradation indicator for online condition monitoring without increasing motor drive costs. To address this challenge, this research uses existing signals in EV motor drives, such as line current measurements. However, there is limited information on how insulation degradation can impact the line currents in the existing literature. Therefore, this Ph.D. work address this knowledge gap through conducting investigations of insulation indicators. It is found that the antiresonance oscillations in line current can serve as indicators for insulation degradation, which was not reported in the existing literature.

Existing literature on condition monitoring methods also presents notable limitations. Firstly, these techniques can not determine the degradation of groundwall (GW) or turn-to-turn (TT) insulations simultaneously. There is a need for a new approach for simultaneous condition monitoring of TT and GW insulations. This is crucial because different types of insulation are exposed to different temperatures, leading to a varied degradation rate. Additionally, current methods overlooked the variability of noise in measured signals, which can fluctuate due to various factors in real-world applications like EVs. This variability necessitates a condition monitoring approach that can handle noise while accurately determining insulation health. Moreover, existing methods rely on predefined thresholds and manual analysis, requiring expert interpretation, which limits their applicability across different machines and conditions. Hence,

this Ph.D. work proposes novel methodologies to address these limitations. A technique for simultaneous monitoring of TT and GW insulation conditions has been proposed. To address the limitation posed by noise variability and the reliance on manual analyses, a novel data-driven methodology for robust insulation condition monitoring has been proposed.

Acknowledgment

Firstly, I would like to express my heartfelt gratitude to my supervisor, Dr. Chunyan Lai, for her unwavering support, professional guidance, inspiration, and invaluable leadership. I am thankful for providing me with the incredible opportunity to achieve a goal that once felt like a distant dream. This journey has had its ups and downs, and her constant support motivated me to embrace the challenges that have contributed to my professional growth.

A special thanks to the committee members Prof. Pragasen Pillay, Prof. Mohsen Ghafouri, Prof. Chunjiang An, External examiner Prof. Xiaozhe Wang and Prof. Luiz A.C. Lopes. I am grateful for their valuable comments, suggestions, and generous time, which significantly improved the quality of the research and thesis.

I would like to highlight that this research work is done with support from Magna International Inc., Canada's Natural Sciences & Engineering Research Council (NSERC) and MITACS. A special thanks to Dr. K. Lakshmi Varaha Iyer for being a source of inspiration and motivation, and for providing support throughout this journey. I would also like to thank Philip Korta, and Animesh Anik for their support.

I express my heartfelt gratitude to the Power Electronics and Energy Research (PEER) group and Concordia University for providing an excellent research environment, state-of-the-art facilities, and support. I would also like to acknowledge my PEER group colleagues, whose camaraderie and support made this journey truly memorable. A special thanks to Dr. Daniel Legrand Mon Nzongo, Dr. Mathews Boby, Dr. Ying Zuo, Dr. Mohanraj Muthusamy, Dr. Akram, Amir, Bassam, Sumeet, Tamanwe, Nazanin, Shiva, Koteswara Rao, Neetusha, Solihah, Paul, Saheel, Ahmad, Sadam, Xizhe, Jia and many more for their support and time during this journey.

I would also like to thank my parents, in-laws, brother, and brother and sister-in-law for their unwavering support. Their encouragement and love have been invaluable to me throughout this journey. Last but not least, I would like to thank my wife, Meghavi, for her love and support throughout this journey. Her belief in me, even during the most challenging times, has been a constant source of strength and inspiration. Thank you for being by my side every step of the way.

This thesis is dedicated to you, Papa and Mummy.
Your sacrifices and unwavering belief in me have been the foundation upon which my dreams are built.

Contents

List of Figures

List of Tables

Chapter 1:Introduction

Electric vehicles (EVs) and electric aircrafts have proven their candidacy as a potential mode of transportation for the coming future. Substantial efforts are being made globally to encourage the adoption of electrified vehicles. As a result, about 14 million new electric vehicles were registered globally in 2023 compared to only 3 million in 2020 [1], this number is expected to grow significantly. To support the transition to EVs, various governments have implemented policies and programs. In Canada, the federal government has introduced the ZEV (Zero-Emission Vehicles) program, which aims to make EVs more affordable by providing monetary incentives [2]. Similarly, at the provincial level, incentives have been offered. For instance, the Quebec government proactively promotes the use of EVs by incentivizing both purchase and lease of electrified vehicles [3]. Moreover, considerable engineering and research initiatives are currently underway to enhance the infrastructure necessary to support the increasing numbers of EVs, which includes the development of more efficient and widespread charging infrastructure [4]. Overall, the potential benefits of electrified vehicles and government incentives are driving market growth and a shift towards electrified transportation. This shift plays crucial role for not only transportation sector but also in addressing carbon emissions and promoting a greener future.

In any electrified vehicle, a powertrain is considered as the core component. Typical drive system of EV is illustrated in Fig. 1-1, while schematic representation is shown in Fig. 1-2. Most

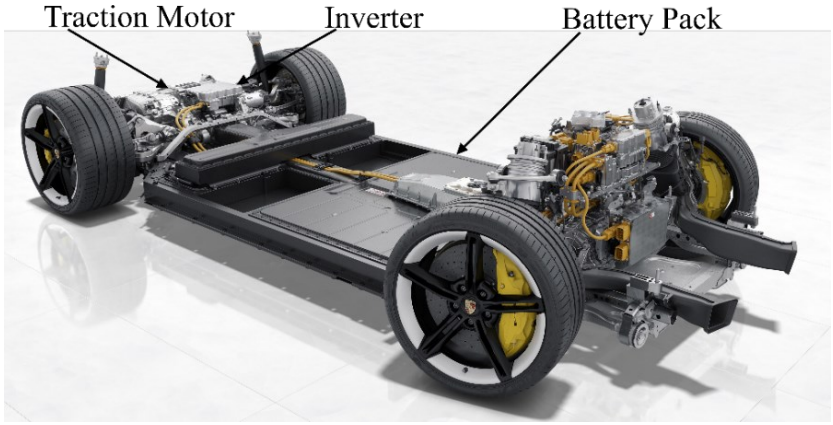

Fig. 1-1 Typical drive system of EV [5]

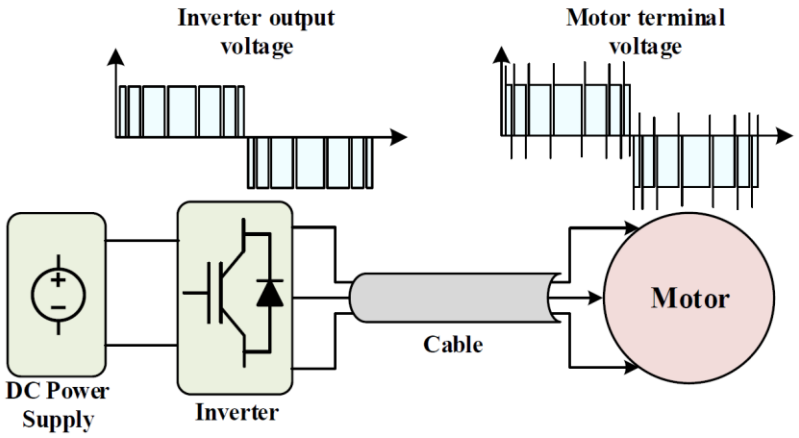

Fig. 1-2 Schematic representation of typical drive system [5]

of the electrified powertrain systems are equipped with batteries, electric machine and voltage source inverters (VSI). The batteries store the energy, while the inverter converts the Direct Current (DC) power into Alternating Current (AC) power to drive the motor over a wide speed-torque envelope.

Typical types of electric machines being used in the EVs are induction machine (IM), permanent magnet synchronous machine (PMSM) and synchronous reluctance machine (SynRM). Within these machines, stator and rotor are the key components. The stator is the stationary part of the machine which contains coils or winding. The winding produces the magnetic field necessary for motor operation when energized by the inverter. The rotor typically equipped with permanent magnets or windings, and it rotates within the magnetic field generated by the stator. The interaction between the fields generated from the stator and rotor ultimately propels the vehicle. Despite significant efforts to design the system in the best way possible, the reliability and safety of such electrified systems get compromised due to various faults. For instance, faults related to batteries include sensor faults, actuator faults, electromechanical faults, charge or discharge rate related faults, and thermal faults may occur [6]-[10]. While faults in inverters are mainly short-circuit fault, open circuit fault, capacitor faults, current/voltage sensor faults [11]-[14]. In electrical machines, faults such as bearing fault, shaft bending, shaft misalignment, eccentricity faults, magnet demagnetization faults, short circuit faults, etc. are prevalent [15]-[18]. Among such faults, short-circuit faults or insulation failures contribute to approximately 30% of motor failures [19]-[21]. There is a decent amount of research being

conducted to design and develop more reliable machine insulation [22]-[27]. However, the aging or degradation of insulation material remains unavoidable due to various internal and external factors [28], [29]. Moreover, the growing interest in utilizing higher DC bus voltages and faster wide-bandgap (WBG) based devices like gallium nitride (GaN) and silicon carbide (SiC) in VSI causes even higher stress on motor insulation [30]-[35].

Given the uncertainties associated with various stresses on insulation, monitoring the insulation condition becomes necessary to ensure the safe and reliable operation of the VSI-fed electric machines, especially in applications like EVs and aircraft where the safety of human life is crucial. Detecting and identifying types of insulation degradation in an early stage can help prevent major failures such as short circuits in the machine. Such information can also be used for predictive maintenance and fault-preventive control strategies to ensure the safe operation of the machine. Therefore, this paper focuses on online monitoring of stator winding insulation degradations in electrical machines. Firstly, the insulation system in stator winding and its degradation are discussed. Thereafter, a literature review on insulation condition monitoring methodologies is presented. Then, the problem statement and objective of the thesis are presented.

1.1 Insulation System

The stator of any machine typically comprises a stator core, winding and insulation system. The stator core is typically made of silicon steel and provides low reluctance path to the flux. The winding is made of copper or aluminum and are arranged in a specific pattern to creates rotating magnetic field when current flows through them. The insulation system comprises of different insulation materials like varnishes, polyimide material, mica, resins, and other

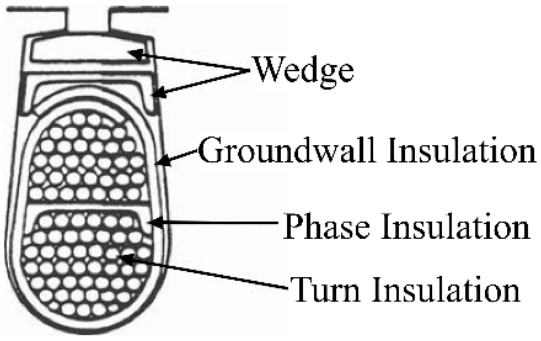

Fig. 1-3 Various types of insulation in stator [29]

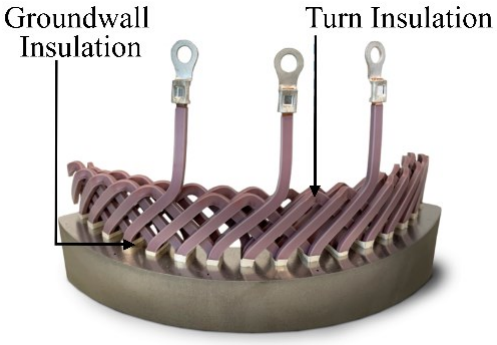

Fig. 1-4 Various types of insulation in hairpin stator [36]

insulating materials, which are essential for ensuring electrical isolation of coils from each other and from the stator. Insulation systems of different types of machines differ significantly from each other. For instance, the insulation system of low voltage machines (rated rms voltage < 700 V) are shown in Fig. 1-3 and Fig. 1-4.

Typically, in low-voltage machines, there are three main types of insulation. The first is referred as turn insulation which refers to the insulation over the wires that ensures separation between turns. Second is the groundwall (GW) insulation, which separates the copper winding from the stator. The third one is phase insulation, which can be found between the phases of the winding. However, it is important to note that phase insulation might not always be present, as it depends on the particular application or design. For instance, as shown in Fig. 1-4, the hairpin stator does not contain any phase insulation. Failure of the insulation system creates a short circuit, which puts the safety and reliability of the whole system at risk. Examples of the damaged winding due turn and groundwall insulation failure are shown in Fig. 1-5 and Fig. 1-6 respectively.

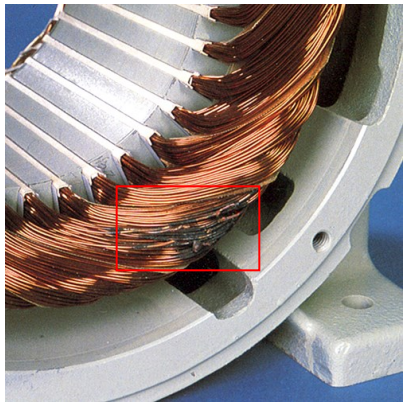

Fig. 1-5 Failure of turn insulation [37]

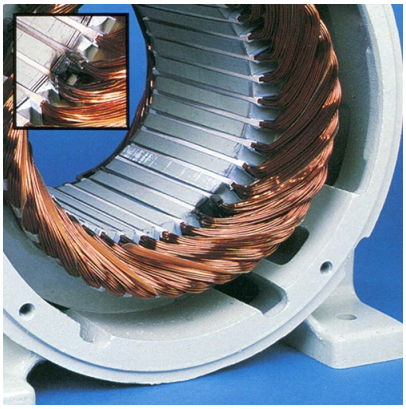

Fig. 1-6 Failure of groundwall insulation [37]

1.2 Insulation Degradation

Apart from improper insulation design and inappropriate operation of the machine, the insulation failure is primarily due to gradual degradation over time caused by TEAM stresses-thermal, electrical, ambient and mechanical stress.

1.2.1.Thermal Stress

Thermal stress is a critical factor in the degradation process of insulation. The insulation material undergoes cyclic exposure to varying temperatures during the operation of the machine. This temperature variation is caused due to generation of heat from losses like copper losses, core losses and stray losses. Due to such thermal stress, the chemical and dielectric properties of insulation are affected [29]-[39]. The thermal stress causes oxidation, where in the chemical bond with the insulation breaks down and oxygen replaces the destroyed bond. Such oxidation weakens the polymer chain and causes degradation. Fig. 1-7 shows the damaged insulation and delamination caused by thermal aging. Moreover, thermal stress also affects the dielectric properties of insulation, causing a reduction in dielectric strength, change in permittivity, change in dielectric loss, etc., which ultimately affect the performance and reliability of the insulation [40]-[42]. Hence, it is crucial to select appropriate insulation materials based on the operational temperature. Insulation materials are categorized into different temperature classes, ensuring they can withstand a specific temperature for approximately 20000 hours. This lifetime is usually approximated by the Arrhenius model, represented as equation (1.1).

$$L = A \cdot exp\left(\frac{R}{T_h + 273.15}\right) \tag{1.1}$$

Here, L is the lifetime of the material, T_h represents the temperature which is often derived from IEC or IEEE standards [43], [44]. Usually, the electrical machines are designed to have the

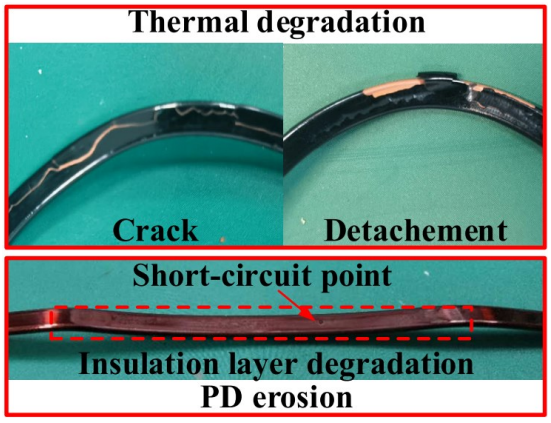

Fig. 1-7 Insulation failure due to thermal stress [45]

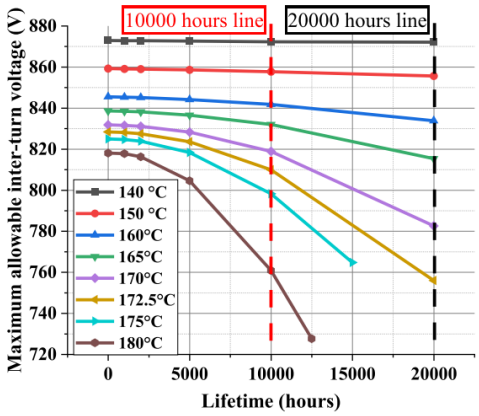

Fig. 1-8 Maximum voltage over the lifetime [46]

insulation class higher than the winding's hotspot temperature to ensure a decent safety margin. Every 10°C increase in the temperature causes a lifetime reduction of 50%. Despite the appropriate selection of temperature class, the performance of insulation suffers due to

degradation. For instance, Fig. 1-8 shows the capability to withstand voltages reduces due to degradation.

1.2.2.Electrical Stress

Due to the utilization of PWM inverters, the insulation of motor winding undergoes higher electrical stress compared to the grid-driven machines. This is due to the nature of the output voltage from the PWM inverter, the output voltages are essentially pulses with varying duty cycle and frequency. Moreover, these pulses reach the maximum value of the DC bus in a few nanoseconds, resulting in a high voltage slew rate or dv/dt, and hence the insulation of machine winding undergoes higher electrical stress which may cause premature insulation failure [33], [47]. The voltage stress on the GW insulation can be up to two times the DC link and may reach up to four times at a neutral point [48], [49]. Moreover, the growing interest to utilize even faster wide-bandgap (WBG) devices like gallium nitride (GaN) and silicon carbide (SiC) based transistors in VSI causes even higher stress on motor insulation. This stress can expedite insulation degradation and can cause insulation failure before its anticipated lifespan. If the voltage across the insulation exceeds the partial discharge inception voltage (PDIV), the partial discharge (PD) occurs. The PDs are the flow of electrons through the insulation or on the surface of the insulation, which degrades the insulation. Hence, there is ongoing research to investigate and understand such electrical stress, which may aid in the improvement and optimization of the insulation system in VSI fed machines [50]-[54].

1.2.3.Ambient Stress

Ambient stress represents the stress on the insulation due to the surrounding environment. Various environmental conditions such as the presence of foreign material, moisture, chemical contaminants, etc. affect the properties of insulation [29]. For instance, moisture condensation significantly increases the rate of degradation [55]-[57]. Moreover, the presence of moisture also affects the dissipation factor, insulation capacitance, permittivity and PDIV of the insulation, which affects the effectiveness of the insulation [58]-[61]. Similarly, other contaminants from the environment may compromise the heat dissipation capability, causing increasing in temperature. Some chemical contaminants react with the insulation material causing accelerated degradation, while some chemicals may affect the mechanical properties of the insulation [29]. Additionally, some conductive contaminants may cause electrical treeing and partial discharge (PD) activity [62]. Therefore, the prevention of electrical machines from ambient stressors is crucial.

1.2.4.Mechanical Stress

The insulation of the machine undergoes mechanical stress mainly due to vibration, transient forces caused by switching of power electronics, thermal expansion and contraction, etc. [29]. Such stresses weaken the insulation and may cause wear-related failure. The electrical motor insulation undergoes vibration due to electromagnetic forces, cogging in machine, operation condition of the vehicle etc. These vibrations may cause mechanical wear due to friction and potentially delamination can occur. Such consequences are further intensified due to loosened winding or inadequate impregnation. Similar mechanical wear occurs due to expansion and contraction of various materials in the motor.

1.3 Literature Review

Over the years, various online insulation condition monitoring techniques have been proposed, which focus on condition monitoring of one or multiple types of insulation degradations. These methods measure quantities such as partial discharge (PD) activity, common mode (CM) current, CM voltage, differential mode (DM) current, high-frequency line current, etc. to identify degradation. However, most of the existing methods pose unique challenges and constraints in implementation such as the necessity for additional sensors or hardware modifications. Such methodologies add complexity or cost to the existing system, making them impractical. Currently, there are a few methodologies that can detect degradation with great accuracy and minimal hardware modifications or additional cost to the typical motor drive system. Given their benefits, such methods are kept in primary focus in this thesis, and they can be mainly categorized into two categories: leakage current measurement based methods and line current measurement based methods. These methodologies, along with their limitations have been summarized in Table 1.1.

Table 1-1 Summary of Condition Monitoring Methodologies

Ref	Year	Measured Quantities	Focused Insulation	Degradation Symptom	Validation Approach	Limitations and Comments
[63]	2019	Leakage current and PG voltage	GW	Decrease in Cap.	Accelerated Thermal Degradation	(1) Additional sensors required (2) Degradations not classified (3) Overlooked variation in measurement noise (4) Lacked theoretical analysis (5) Limited validation

[64]	2022	Leakage current and voltages	GW	Increase in Cap.	Capacitance and resistance based emulation of degradation	(1), (2), (3), (4), (5)
[65]	2021	Leakage current and PG voltage	GW and PP	Increase in Cap.	Capacitance based emulation of degradation	(1), (3), (4), (5), and (6) Neglected simultaneous degradation in classification
[66]	2021	Leakage current and PG voltage	TT	Increase in Cap.	Capacitance based emulation of degradation	(1), (2), (3), (4), (5)
[67]	2023	Leakage current and PG voltage	GW and TT	Increase in Cap.	Capacitance based emulation of degradation	(1), (3), (4), (5), (6)
[68]	2018	Leakage current	NA (Overall)	Decrease in Cap.	Accelerated Thermal Degradation	(1), (2), (3), (4), (5)
[69]	2013	Leakage current	GW	NA	NA	(1), (2), (3), (4), (5)
[70]	2010	Leakage current	NA	Increase in Cap.	NA	(1), (2), (3), (4), (5)
[71]	2015	Line current	TT	Increase in Cap.	Capacitance based emulation of degradation	(2), (3), (4), (5)
[72]	2017	Line current	TT	Increase in Cap.	Capacitance based emulation of degradation	(2), (3), (4), (5)
[73]	2022	Line current	GW	Increase in Cap.	Capacitance based emulation of degradation	(2), (3), (4), (5)
[74]	2021	Line current	TT	Increase in Cap.	Capacitance based emulation of degradation	(2), (3), (4), (5)
[75]	2022	Line current	GW	Increase in Cap.	Capacitance based emulation of degradation	(2), (3), (4), (5)
[76]	2023	Line current	NA (Overall)	Decrease in Cap.	Accelerated Thermal Degradation	(2), (3), (4), (5)
[77]	2019	Line current	NA (Overall)	Increase in Cap.	Accelerated Thermal Degradation	(2), (3), (4), (5)

Leakage current measurement-based methods typically utilize the fact that the degradation in insulation causes deviation in the CM impedance spectrum, this variation is caused by variation in insulation capacitance due to degradation. For instance, in [63], GW condition monitoring

method based on the variation of capacitance is presented, and it utilizes measurements of phase-to-ground (PG) voltage and leakage current measurement to determine equivalent capacitance which is further utilized to determine insulation condition. In [64], a methodology that relies on the measurement of leakage current to identify the degradation in GW insulation is proposed, which uses characteristics such as initial oscillation amplitude, oscillation period, and attenuation time of leakage current to determine insulation condition. In [65], a methodology which can monitor both GW and phase insulation condition is presented. This method relies on the measurement of leakage current and PG voltages, it has the unique capability to monitor the phase-to-phase (PP) and GW insulation capacitance separately. In [66], a similar approach utilizing leakage current and PG voltages for TT insulation condition monitoring is presented. In [67], a unique method which can classify between the TT and GW degradation is proposed. The method requires leakage current and utilizes deviation in the CM impedance spectrum. This method can be considered as a data driven method since various degradation scenarios have been emulated and the corresponding impedance spectrum obtained by the proposed simulation model, thereafter the impedance data is further processed using the principal component analysis (PCA) method which works as features for the decision tree machine learning model and decision tree model estimates the insulation condition. In [68], an analog circuit has been proposed which is utilized to detect the peak value of the leakage current and deviation in the peak value of leakage current is utilized for insulation condition monitoring. In [69], GW condition monitoring based on only common mode leakage current measurement is presented. In [70], a leakage current measurement based methodology that estimates capacitance and dissipation factor has been presented. Nevertheless, the leakage current measurement-based methods are often considered less desirable due to the requirement of additional sensors for leakage current and/or voltage measurements, and hardware modifications. Integration of these additional sensors into a drive system leads to increased complexity and cost.

In contrast, line current based methods are preferable in general, as the current sensors are usually already integrated in a typical drive system. In [71] and [72], methods that utilize deviation in the frequency spectrum of measured high-frequency line current have been proposed. This is done by calculating the frequency spectrum of the transient current and identifying change with the reference frequency spectrum, which represents the healthy insulation state. Deviation between these two spectrums has been interpreted as a sign of

insulation degradation. These methods primarily focus on TT insulation condition monitoring. In [73], a GW insulation condition monitoring methodology that focuses on degradations in line-end coils is presented, which utilizes high frequency common mode current extraction from the line current oscillations. The high frequency common mode current extraction is done using the variable mode decomposition (VMD) algorithm. A similar approach that relies on transient line current is presented in [74], where low frequency common mode current, also referred to as 'tail current', is extracted from HF line current for condition monitoring of TT insulation. The root mean square (RMS) value of the tail current has been used as an indicator of the insulation state and deviation in this value is considered as an indicator of degradation. In [75], ringing in the transient line current has been analyzed for condition monitoring of the GW insulation, it was found that the RMS values and peak values of current ringing showed a quasi-linear increase with the change in parasitic capacitance. Moreover, various literature reports investigate the influence of different types of exposure on the line current. For instance, as in [76], investigations on the influence on the line current when accelerated aging has been performed. Similarly, in [77] investigations on the line current when the machine is exposed to high dv/dt PWM excitation show that line current can be utilized for reliable insulation condition monitoring. The leakage current measurement based methods are often considered less desirable because they require the inclusion of additional sensors for leakage current and/or voltage measurements, or hardware modifications. Given the advantages of the line current based approach, this thesis focuses on the line current measurement based approach. Therefore, this Ph.D. thesis focuses on methods that rely on measurement of line current.

1.4 Problem Statement

As summarized in Table 1.1, most of the existing literature lacks theoretical analysis on insulation condition monitoring methodologies, to conduct such analysis often lumped HF stator winding models are utilized [65],[66]. Such simpler models can be utilized for certain applications but cannot be used to simulate various insulation degradations accurately and investigate online insulation condition monitoring. Specifically, these models have limited capability in representing the accurate HF behavior of the winding and the distribution of voltages within the stator winding [53]. Effective investigations for insulation condition monitoring demand higher accuracy in HF winding models. Therefore, for the development of

accurate HF stator winding models which can be further utilized for the development of condition monitoring techniques.

Another limitation is that there exists a significant knowledge gap in understanding of the influence of insulation degradations on the line current, existing literature presents limited investigations. The existing literature presents limited investigations on the influence of insulation degradation HF line current and common mode/differential mode (CM/DM) impedance spectrum of the winding. Understanding the influence of insulation degradation on the HF line current and its corresponding impedance spectrum is crucial to understanding the influence of insulation degradation and development of condition monitoring methodology. A comprehensive investigation should be conducted to understand the influence of insulation degradation of both TT and GW insulation types with varying degradation severities and various locations within the winding.

Existing line current measurement based techniques can be considered fairly accurate, however, there exists a key limitation. Existing methodologies present condition monitoring of either GW insulation or TT insulation, which lack the ability to quantify TT and GW insulation degradations simultaneously. However, condition monitoring of both TT and GW insulations simultaneously is crucial because different types of insulation are exposed to different temperatures, potentially leading to a varied degradation rate. Additionally, the impedance spectrum deviations caused by the aging of TT insulation can be influenced by the degradation of GW insulation [67]. Therefore, accurately classifying the degradation of each insulation type is essential for a comprehensive assessment.

Another major shortcoming of existing methods is that the variability of noise in the measured current signal is disregarded. In practice, the noise level in the measured signal varies due to various factors. It is crucial to make sure that the method performs well across a wide range of noise levels, ensuring its viability in real-world applications. Additionally, the existing approaches rely primarily on predefined thresholds and manual analyses, which necessitates expert knowledge for data interpretation and feature analysis. Such dependency limits their adoption across different machine types and operational conditions. Such complexities associated with different degradation patterns and noise levels lead to a need for a more universal method that has the potential to be applied to any machine. Data-driven or machine learning

based approaches could be beneficial in condition diagnosis due to their ability to learn and adapt to any data. For instance, in [14], the application of a machine learning (ML) algorithm for leakage current measurement based insulation condition monitoring shows promising results. Due to the apparent advantages of such methods, this thesis proposes a novel data-driven line current based approach for insulation condition monitoring.

1.5 Objectives

The key limitations of the existing approach and open research problems in the field of line current measurement based condition monitoring have been discussed. The primary objective of this PhD research is to address these limitations and explore potential solutions. The problems that will be addressed as part of this research work are as follows:

- **Holistic investigation of insulation degradation:** This PhD research will conduct a comprehensive investigation into the influence of insulation degradation on HF line current and the common mode/differential mode (CM/DM) impedance spectrum of the winding. Such investigations are crucial for developing effective condition monitoring methodologies. To conduct such investigations, a simulation-based approach is employed. This is because the hardware based approach does not offer control over degradation location (TT and/or GW insulation) and degradation severity. Hence primarily a HF stator winding model is required to conduct such investigations.
  - Implementation of state-of-the art approach to develop a custom HF stator winding model: This PhD research aims to create a HF stator winding model for custom stator winding, that will enable comprehensive investigations to establish condition monitoring methodologies. This model is capable to represent the HF behavior of the winding and the inclusion of various insulation materials. This model would enable simulations of various types and severity of insulation degradations, laying the path for investigation on the influence of degradation on transient current as well as impedance spectrums.
- **Development of line current based condition monitoring methodologies:** Utilizing the learning from the previous investigations, the following areas will be focused on.

- To develop a condition monitoring methodology that utilizes line current to determine the State of Health (SOH) and facilitates the differentiation of insulation degradation types.
- To develop a condition monitoring methodology focused to address the variability such as noise in measured line current. The objective is to ensure this methodology's practical applicability, especially in environments with pronounced noise variability, such as EVs. The methodology should be capable of performing well across different levels of measurement noises.

1.6 Thesis Organization

Based on the research objectives, this thesis is organized into the following chapters.

Chapter 1 presents introduction to the insulation failure and emphasizes on the importance of insulation condition monitoring. A comprehensive review of existing condition monitoring methodologies has been presented. The research problem statement, objectives, and contributions have been presented.

Chapter 2 presents the development of the HF model of the stator winding. The modeling procedure and validation of the developed model have been discussed. The developed model enables detailed investigations required for understanding and development of online insulation condition monitoring methodology.

Chapter 3 presents comprehensive investigations on the influence of different insulation degradations on the HF line current, CM impedance and DM impedance. Based on the results of the investigations, the utilization of dominant antiresonance oscillations in line current has been proposed for insulation condition monitoring.

Chapter 4 proposes a novel insulation condition monitoring technique, which employs wavelet packet decomposition (WPD) to analyze high frequency (HF) line current and extract indicators for monitoring the state of health (SOH). The proposed technique can provide the SOH indicators of turn-to-turn (TT) and groundwall (GW) insulation simultaneously.

Chapter 5 presents a novel data-driven insulation condition monitoring methodology. The methodology utilizes a machine learning (ML) algorithm to quantify the insulation degradation by utilizing the features obtained by processing HF line current. This methodology utilizes

wavelet scattering transform (WST) to extract crucial features from HF line current. This chapter also presents a comprehensive framework designed for developing insulation condition monitoring using the proposed ML based approach.

Chapter 6 presents the conclusion of this thesis and possible future works.

1.7 Contributions

Journal papers:

- **A. Patel**, C. Lai and K. L. Varaha Iyer, " Wavelet Packet Decomposition based Detection and Classification of Stator Winding Insulation Degradation for Electric Machines," *in IEEE Transactions on Industry Applications* [Under second review]

- **A. Patel**, C. Lai and K. L. V. Iyer, " A Data-Driven Approach for Stator Winding Insulation Degradation Monitoring Considering Measurement Noise" *in IEEE Transactions on Industry Applications* [Under review]

- **A. Patel**, C. Lai and K. L. V. Iyer, " Online Insulation Condition monitoring based on Antiresonance Oscillation in Line Current" Will be submitted to the *IEEE Transactions on Industrial Electronics*.

Conference papers:

- **A. Patel**, C. Lai and K. L. Varaha Iyer, "A Machine Learning based Approach for Detection and Quantification of Insulation Degradations in Machines' Stator Winding," *2023 IEEE International Conference on Power Electronics, Smart Grid, and Renewable Energy (PESGRE),* Trivandrum, India, 2023.
- **A. Patel**, C. Lai and K. L. V. Iyer, "A Novel Approach towards Detection and Classification of Electric Machines' Stator Winding Insulation Degradation using Wavelet Decomposition," *2023 IEEE International Electric Machines & Drives Conference (IEMDC),* San Francisco, CA, USA, 2023.

Patent:

- **A. Patel**, C. Lai, N. C. Kar, G. Schlager, M. Winter, A. Exl and K. L. Varaha Iyer, "Determination and Classification of Electric Motor Winding Insulation Degradation" World Intellectual Property Organization (WIPO), WO2022094726A1. (Application filed in Nov, 2021)

Chapter 2:Development of Custom HF Stator Winding Model

2.1 Introduction

This chapter focuses on development of the high frequency (HF) modeling of the stator winding, development of the HF stator winding model plays a crucial role in investigating condition monitoring methodologies. Firstly, a brief overview of existing modeling approaches has been provided. Thereafter, the details on the HF modeling of stator winding using the multiconductor transmission line modeling (MCTL) approach have been presented. The developed model has the capability to incorporate frequency dependent resistance, frequency dependent inductances as well as detailed insulation system, leading to the accurate representation of the HF behavior of the winding. Moreover, the accuracy of this simulation model is investigated through an experimental investigation. The developed model will be utilized in the following chapters in studying insulation degradation and further developing condition monitoring methodologies.

2.2 Brief Literature Review on HF Stator Winding Modeling Methodology

There exist various winding modeling approaches in the literature. Some of the very first practices of HF stator winding modeling can be found in mid-1900s. For instance, in [78], the utilization of multiport networks for stator winding modeling has been presented. In 1983, as in [79], a scattering matrix solution-based approach was presented to investigate interturn voltages. Different approaches have been presented over the years. For instance, lumped parameter equivalent RLC circuit-based approach [79]-[81], transmission line based approach [82]-[85], finite element based approach [86], [87], [88], and multiconductor transmission line (MCTL) based approach [89]-[94]. Detailed comparative comparison of various modeling approaches has been presented to determine the most promising approach, taking into account both the advantages and limitations [95], [96]. Among the existing approaches there are two approaches that show great results due to their capability to consider frequency dependent parameters and capability to consider detailed insulation material, these approaches can be considered state-of-the-art. These approaches are 1) Finite element (FE) based approach [86], [87], [88], and 2) multiconductor transmission line (MCTL) based approach [91], [92], [90]. In the context of HF

modeling, it is critical to consider frequency dependent behavior in the winding's resistance and inductance. In [86], the FE based model was used to analyze voltages stress during switching transients, the model considered frequency dependent inductance, but frequency dependent resistance was not considered, which shows fairly good match between the predicted and actual voltages. However, this approach requires extremely large computation resources since the magnetic field solver to determine frequency dependent parameters are solved for each time-step, which is less feasible. On the other hand, the MCTL based approach effectively addresses the limitation of the FE based approach by including frequency dependent inductance as well as resistance. Moreover, the MCTL approach significantly reduces the computational requirements compared to the FE method. However, the initial complexity and effort required for the MCTL model are much more than the FE based approach. However, it can be viewed as a worthwhile investment. Once the model is developed, it requires much less computation resources and less time to utilize the model. As discussed, the developed model will be utilized to conduct investigations on insulation degradation and the development of condition monitoring methodology. Such investigations require repetitive simulations of various degradation scenarios. Furthermore, the ability to conduct these simulations with fewer computational resources and less time, makes it suitable for ongoing condition monitoring. Hence, this thesis work utilizes the MCTL based approach due to the promising results, reduced computation cost and ability to provide faster results.

2.3 HF of Stator Winding using MCTL approach

This section discusses the HF modeling of stator winding using the MCTL approach. The key processes involved in the modeling are presented in Fig. 2-1. A stator of any machine mainly consists of three components: the stator core, conductors or wires, and insulation. Hence the first step involves the creation of a detailed slot model in the FEA tool, Ansys Electronics Desktop (AEDT). The created slot model should include detailed arrangements and properties of wires, insulation material and iron core. In order to simplify investigations and modeling, a winding with 8 coils or 24 turns is developed and modeled using MCTL approach. The developed model adequately serves the purpose of investigating online insulation condition monitoring methodologies. The properties of stator and insulation systems are summarized in Table (2.1). The experimental stator winding is shown in Fig. 2-2, while Fig. 2-3 shows the winding pattern and slot model created model in AEDT. The cross section of a slot shows the arrangement of

wires and the insulation system. The winding consists of a total of 8 coils or 24 turns (3 turns per coil). The total number of turns in each slot is 6 and there are 16 wires per turn. Hence there are 96 wires in each slot. The TT insulation is the insulation over the wires while the GW insulation is the insulation that separates wires from the stator. It is important to note that the developed model assumes the same arrangement of wires in all slots, as the model is primary utilized to investigate the impact of insulation degradation.

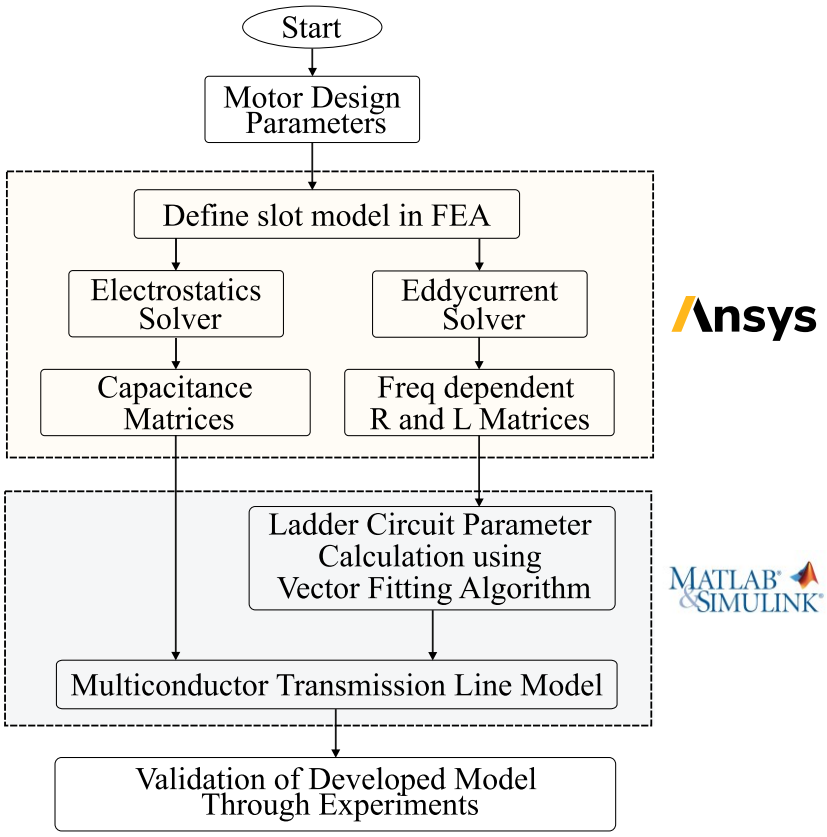

Fig. 2-1 HF stator winding modeling using MCTL approach

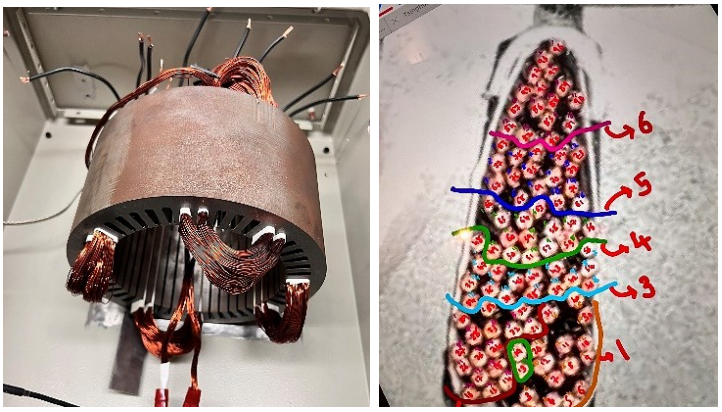

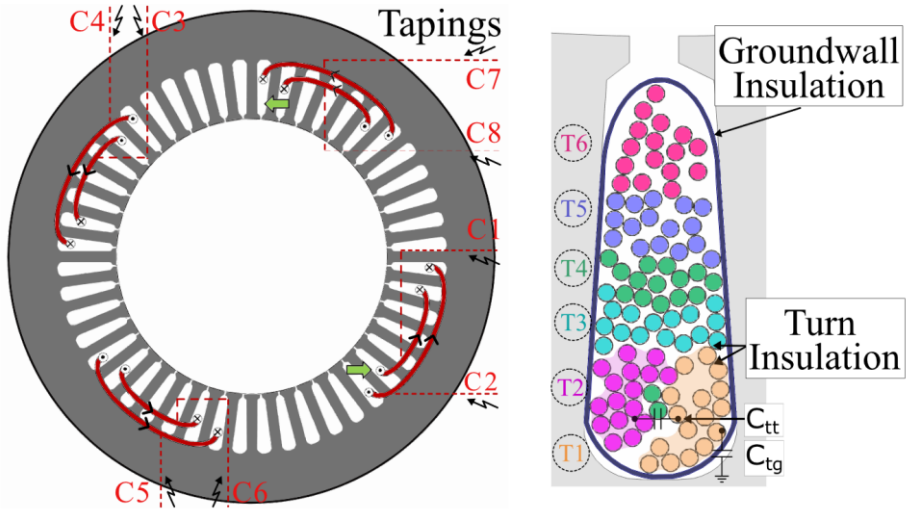

Fig. 2-3 Ilustation of stator winding and slot cross-section in FEA

Table 2-1 Properties of Insulation

Insulation Type	Material	Thickness (mm)	Dielectric Constant
Groundwall insulation	Nomex® 410	0.18	2.7
Wire Insulation (Enamel)	Epoxy Kevlar	0.07	4.88

After defining the slot model in the FEA tool, the next step involves the computation of parameters. The inductance and resistance of the winding changes significantly with the frequency. Moreover, the wires or turns inside the slot have mutual coupling among them, which varies with the frequency. Apart from such electromagnetic coupling, there exist capacitive coupling among the turns as well as with the iron core. It is crucial to incorporate such capacitive and electromagnetic coupling to obtain an accurate HF winding model. Hence, an electrostatics solver is utilized to obtain the capacitive coupling. To solve electromagnetic coupling and obtain frequency dependent resistance and inductances, the eddy-current solver has been utilized. The detailed parameter computation is discussed in the following section.

The next step after parameter computation involves the computation of ladder circuits (LCs) parameters from the frequency dependent resistances and inductances obtained from the previous stage. To model frequency dependent resistance and inductance, a ladder circuit (LC) can be used. A LC comprise of various inductances and resistance organized in a ladder formation and,

which can replicate the frequency dependent behavior. A vector fitting (VF) algorithm has been utilized to extract these LC parameters from the previously calculated frequency dependent resistance and inductances. The comprehensive procedure to determine LC parameters is discussed in the next section.

Once the required parameters and LCs are obtained, the MCTL model can be created as shown in Fig. 2-4. The developed model shows 8 coils, each coil containing 3 turns totaling 24 turns. The inductance and resistance of each turn can be modeled using equation (2.1), where V_i is the voltage across one turn i, which represents the voltage due to self impedance and mutual coupling with other turns. For each turn i, R_{ii} and L_{ii} represents the self-resistance and inductance respectively, while I_i is the current flowing through it. Hence, the first term in equation (2.1) represents voltage V_{ii} due to self parameters. In the second term, parameters R_{ik} and L_{ik} represent the resistive and inductive coupling between turns i and k, while I_k is the current through the k^{th} turn. Here, the term restive coupling refers to the voltage drop caused due to skin and proximity effect. Hence, the second term represents turn voltage due to mutual coupling V_{ik} with other turns. Here, the term N_t represents the total number of turns per coil. Utilizing the equation, the equivalent MCTL model of the winding can be created as shown in Fig. 2-4.

$$V_i = \left(R_{ii}(f)I_i + L_{ii}(f)\frac{dI_i}{dt}\right) + \sum_{\substack{k=1 \\ k\neq i}}^{N_t} \left(R_{ik}(f)I_k + L_{ik}(f)\frac{dI_k}{dt}\right) \tag{2.1}$$

To represent the first term in the equation in frequency dependent manner, an LC is utilized which replicates frequency dependent self resistance and self inductance. The second term in the equation represent the voltage drop V_{ik} due to currents mutual coupling, which is due to the effect of skin and proximity effect and mutual coupling. Which is modeled using the current dependent voltage source. For each turn i, the current in each coupling turn (I_k) causes opposing voltage drop due to the mutual coupling. This coupling is also frequency dependent, which can be represented using a LC as well. To model this the voltage drop V_{ik}, current dependent voltage source can be utilized which represents the voltage drop due to the mutual coupling. Hence, when considering a coil with 3 turns, a single LC circuit captures the voltage drop from the turn's self parameters. While 2 distinct LC can be utilized to model the voltage

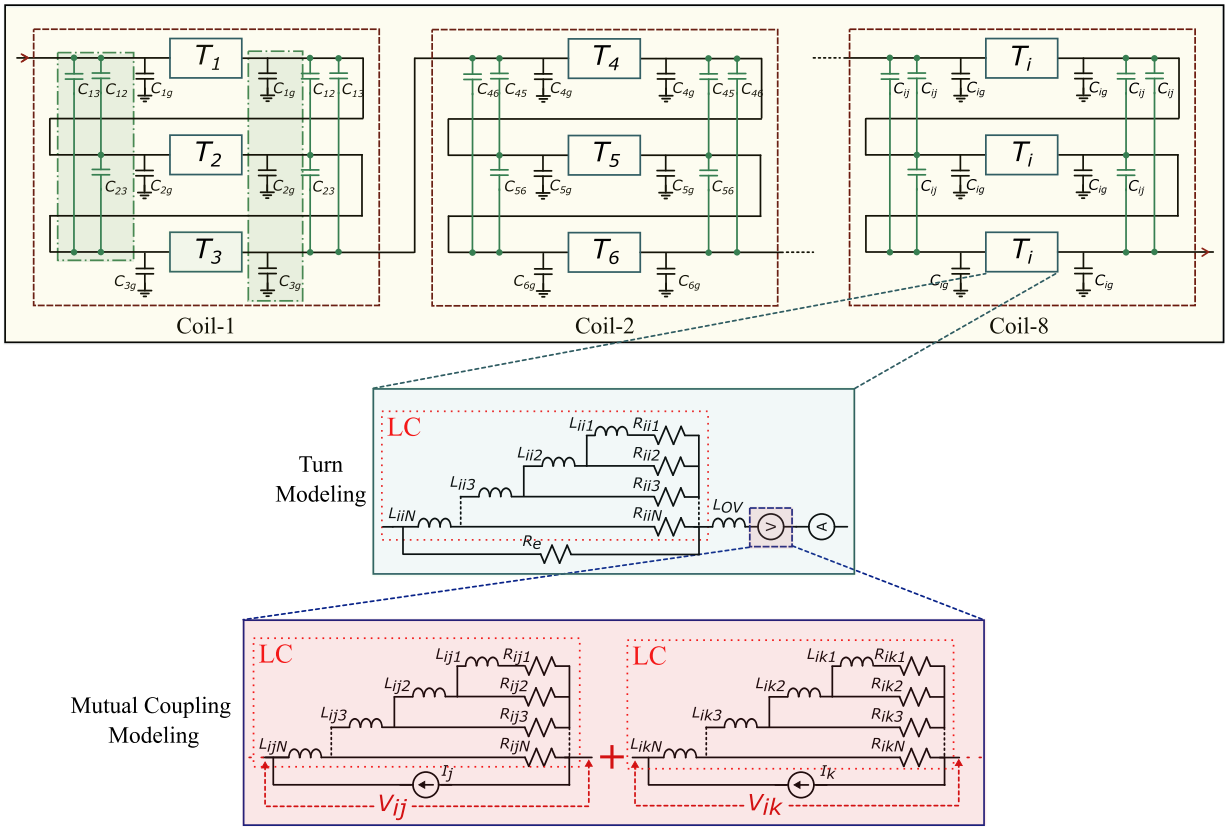

Fig. 2-4 HF Modeling of Stator Winding using MCTL approach

drops due to mutual coupling with remaining turns. Apart from LCs and current-dependent voltage sources, there are other parameters including: 1) L_{ov} represents the overhang inductance per turn 2) R_e which represents per turn core loss 3) C_{ij} represents the capacitance between two turns, (π representation) 4) C_{ig} represents half the value of turn to ground capacitance (π representation). The details of the calculation of these parameters are discussed in the following section. The model can be built in any circuit simulation tool, this thesis work utilizes MATLAB/Simulink environment.

2.4 Parameter Computation for MCTL Model

As briefly discussed in the previous stage, parameters such as capacitances, frequency dependent resistance and inductances, ladder circuit (LC) parameters, overhand inductance per turn (L_{ov}) and core loss resistance per turn (R_e) are required to be calculated. This subsection discussed the procedure to calculate the aforementioned parameters.

2.4.1.Capacitance Calculation

Electrostatics solver in the AEDT has been utilized to compute capacitance. The electrostatics computes the static electric field that exists in a structure given a distribution of DC voltages and static charges and provides a capacitance matrix, which can be further processed to compute the capacitive coupling among the conductors [97]. The capacitance represents the amount of energy stored in the electric field due to a voltage differential across a dielectric. This energy can be given by the equation (2.2).

$$W_e = \frac{1}{2}CV^2 \tag{2.2}$$

Here, the W_e is the stored energy, C is the capacitance and V is the voltage across the dielectric. The Electrostatics solver computes the capacitance between two conductors by simulating the electric field due to various voltage excitations. Then the energy stored in the field is computed followed by calculating the capacitances. Each turn in the winding is mainly distributed over two different regions: 1) slot region where the wires are covered by the core. And 2) overhang region or end winding region where the wires are in the air. For both regions, the capacitive coupling among the turns is different. It is important to consider this variation in parameters.

Capacitance Calculation in Slot Region: The first step is to assign voltage excitation to the turns of the coil among which the capacitance coupling will be calculated. The standard practice is to assign 1V to one of the turn voltages and the rest can be assigned 0V. Moreover,

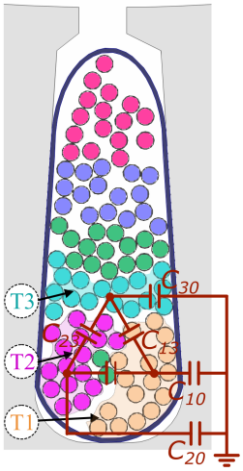

Fig. 2-5 Illustration of capacitance coupling in the slot

the stator is also assigned a voltage. The next step includes the assignment of appropriate matrix, boundary conditions, mesh settings, and analysis settings. Thereafter, the electrostatics solver calculates the capacitance coupling among the conductors with excitation and provides a maxwell capacitance matrix. Here, each coil contains 3 turns, the resultant capacitive coupling is as shown in Fig. 2-5. The capacitor C_{ij} represents the capacitor between turn i and turn j. While capacitor C_{i0} represents the capacitance with respect to the stator. The capacitance matrix provided by the solver is shown in equation (2.3), while for a system with N conductors, the matrix can be given by following equation (2.4). Here, diagonal elements in the matrix represent the self-capacitance of each turn while off-diagonal elements represent mutual capacitances. Using the given relation, C_{ij} and C_{i0} capacitances can be obtained. It is important to know that the matrix obtained provides capacitance per meter. Depending on the length, the matrix must be converted to obtain correct capacitances.

$$\begin{bmatrix} Q_1 \\ Q_2 \\ Q_3 \end{bmatrix} = \begin{bmatrix} C_{10} + C_{12} + C_{13} & -C_{12} & -C_{13} \\ -C_{12} & C_{20} + C_{12} + C_{23} & -C_{23} \\ -C_{13} & -C_{23} & C_{30} + C_{13} + C_{23} \end{bmatrix} \begin{bmatrix} V_1 \\ V_2 \\ V_3 \end{bmatrix} \tag{2.3}$$

$$\begin{pmatrix} Q_1 \\ Q_2 \\ \vdots \\ Q_N \end{pmatrix} = \begin{bmatrix} \sum_{\substack{i=0 \\ i\neq 1}}^{N} C_{1i} & -C_{12} & \cdots & -C_{1N} \\ -C_{21} & \sum_{\substack{i=0 \\ i\neq 2}}^{N} C_{2i} & \cdots & -C_{2N} \\ \vdots & \vdots & \ddots & \vdots \\ -C_{N1} & -C_{N2} & \cdots & \sum_{\substack{i=0 \\ i\neq N}}^{N} C_{Ni} \end{bmatrix} \begin{pmatrix} V_1 \\ V_2 \\ \vdots \\ V_N \end{pmatrix} \tag{24.}$$

Overhang region capacitance: In the overhang region, the winding is in the air so there is no capacitive coupling with the stator. Only the capacitances between turns (C_{ij}) required to be considered and capacitances with respect to the stator (C_{i0}) can be disregarded. A similar procedure as can be followed to obtain the capacitance matrix for the overhang region.

Here, it is crucial to note that the accurate properties of insulation and the properties of wires are required to be considered while developing a slot model in AEDT. Moreover, it is extremely important to replicate the accurate arrangement of wires and insulation. The properties of insulation are presented in Table (2.1). The required properties of GW insulation including thickness and dielectric constant have been obtained from the datasheet. However, information

on turn insulation is readily available. Given the importance of the accurate parameters in capacitance calculation, these properties have been approximated through some measurements. The details are discussed in the following subsection.

2.4.2.Determination of Turn Insulation Properties

The required properties are thickness and the insulation dielectric constant. The accurate information on these parameters is not available in the datasheet, especially the dielectric constant. To obtain the insulation thickness, the overall diameter of the wire is measured which was 0.81mm while the copper wire diameter is 0.67mm (from the datasheet) [98]. Hence, the insulation thickness is determined to be 0.07mm. To obtain the dielectric constant of the insulation, a capacitance measurement-based technique is used. It is common practice to use wires of twisted pair (two wires twisted against each other) for the capacitance of dielectric material and partial discharge inception voltage (PDIV) correlation investigations [99], [100], [101] . Hence, a similar approach is used to determine the dielectric constant of the insulation. Firstly, a total of 22 twisted pairs of different lengths were created, which are shown Fig. 2-6 and Fig.2-7. Then using an impedance analyzer, the capacitance between two wires is obtained, which is due to 0.14mm (for one wire thickness is 0.07mm) of insulation. The average capacitance is calculated from all the samples. Table (2.2) summarizes the average capacitance obtained from 22 twisted pairs.

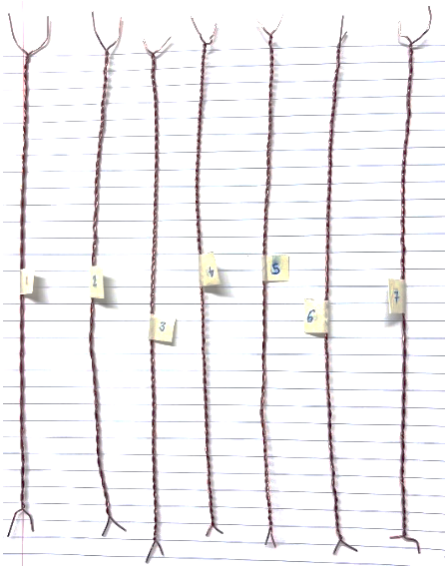

Fig. 2-6 Twisted pairs of wires (130mm)

Fig. 2-7 All the samples of twisted pairs of wires

Table 2-2 Measured capacitances for various twisted pairs of wires

Approx. Twisted Pair Length	Sample No.	Measured Capacitance (pF)	Actual Length (mm)
130 mm	1	17.1	132
	2	16.5	131.5
	3	15	127.5
	4	15.6	129.5
	5	15.3	127.5
	Average	**15.9**	**129.6**
	Capacitance/100mm		**12.26 pF**
200 mm	1	21.7	195.5
	2	21.1	202.5
	3	23.7	207.5
	4	23.2	208.5
	5	21.2	208
	6	21.8	208
	7	22.2	204
	Average	**22.13**	**204.85**
	Capacitance/100mm		**10.8 pF**
400 mm	1	45	394
	2	45.9	395.5
	3	47	397
	4	44.8	395.5
	5	46.7	397
	Average	**45.88**	**395.8**
	Capacitance/100mm		**11.59 pF**
600 mm	1	65.9	575
	2	62.4	569.5
	3	66.8	570
	4	66	571
	5	64.3	570.5
	Average	**65.08**	**571.2**
	Capacitance/100mm		**11.39 pF**
All samples	**Capacitance/100mm**		**11.51 pF**

The average capacitance is 11.51 pF/100 mm. This information is further used to determine the dielectric constant is determined using the electrostatics solver in AEDT. In AEDT, two wires are modeled to be in close contact with each other. The diameter of the wire is 0.67mm and the thickness of the insulation is 0.07mm. Each wire is assigned voltage excitation, other necessary settings are done, and the capacitance is obtained between two wires. Then the dielectric constant is adjusted to obtain the same capacitance which was obtained from the measurement i.e. 11.51pF/100 mm. The determined dielectric constant is 4.88.

2.4.3.Frequency Dependent Resistance and Inductance Calculation

Resistance and Inductance of the wires vary depending on the frequency due to skin and proximity effects. Pulses from a PWM inverter can be considered as a superposition of multiple frequency components. For instance, machine operating frequency, switching frequency, the frequency corresponding to the rise time of the pulse, etc. For accurate determination of electrical stress, it is important to consider variations in resistance and inductances due to the frequency. The excitation pulse is a typical voltage pulse that can be considered as HF excitation to the winding, with an excitation frequency that extends up the frequency of $f_{max} = 1/\min(t_r, t_f)$. Here, t_r is rise time and t_f is the fall time of the PWM pulse. Ideally, inductance and capacitance variation up to f_{max} should be considered. Here, the minimum rise or fall time is 20ns, which corresponds to the f_{max} of 50Mhz. So, the model has been developed to replicate the frequency dependent behavior up to 55MHz. So, the eddy current solver in AEDT has been utilized to calculate frequency dependent resistance and inductances. This also includes the calculation of mutual resistive and inductive coupling among various turns in a slot also varies with the frequency which is also obtained using the eddy current solver. Similar to the capacitance calculation, each turn in the coil is assigned with a current excitation of 1A. Apart from this, appropriate matrix, boundary conditions, mesh settings, frequency sweep, and analysis settings are applied. The solver solves the electromagnetic field within the coil and provides a matrix for each frequency point.

The diagonal elements in the matrix represent self impedance while the off-diagonal elements represent the mutual coupling among the turns. Hence, the impedance matrices for seven frequency points (50Hz, 500Hz, 5KHz, 50KHz, 500KHz, 5MHz, and 55MHz) are obtained. These parameters will be further used to create various ladder circuits (LCs), which are discussed in the next subsection.

2.4.4.Overhang Inductance Calculation

The total overhang inductance of the winding is considered to be constant. This is because the wires are placed in the air and the influence of frequency is comparatively smaller than in the slot region. The overhang inductance per turn has been determined using the equation (2.5).

$$L_{ov} \cong k_r \cdot \frac{1}{N} \cdot \left(\mu_0 N^2 \cdot \left(\frac{2}{P}\right) \cdot \lambda_b \cdot l_{ov}\right) \tag{2.5}$$

Here, k_r is a constant that accounts for the reduction in inductance due to skin effect, N is the number of turns per phase, λ_b is geometry coefficient and l_{ov} is the length of the overhang in each turn. The determined L_{ov} per turn is 1.016 μH.

2.4.5.Core loss Resistance Calculation

There is not enough research or established methods for the calculation of R_e. However, there is a relation between the core loss resistance and the stator outer diameter, which can be used to determine R_e [92], [102]. According to [92], core loss resistance per phase is estimated at 2 kΩ for a stator with a diameter of 16.19 cm, (2010 Toyota Prius machine). The winding has 11 turns per coil and 8 series coils per phase, hence the value of R_e determined to be s 22.73 Ω. The developed winding in this thesis has a stator has a diameter of 20 cm, hence using the same approximation the core loss resistance per phase would be 2470 Ω. The winding has 3 turns per coil and 8 series coils per phase. Based on the winding arrangement, the core loss resistance per turn R_e is obtained as 102.91 Ω.

2.4.6.Ladder Circuit Parameters Calculation

This subsection presents the procedure to obtain the LC parameters from frequency dependent resistances and inductances acquired. The Ladder circuit is essentially multiple inductances and resistances connected in step format to approximate the variation in parameters due to frequency. The parameters obtained from the eddy current solver are required utilized to create LCs so the frequency dependent winding parameters can be modeled. To calculated LC parameters, a vector fitting (VF) based algorithm has been employed. As shown in Fig. 2-8, this algorithm processes the parameters derived from the previous stage to determine the final LC values. Detailed procedures to obtain parameters of LC are shown in Fig. 2-9.

As outlined in the provided flowchart, the LC parameters for each level are sequentially calculated. The process is repeated for each level until all LC parameters are obtained. Once all the parameters for LC are obtained, the frequency response of the LC can be compared against the desired response or (parameters from the eddy current solver) to ensure that the LC is capable of replication similar behavior. For instance, Fig. 2-10 and Fig. 2-11 show parameters obtained from the eddy current solver and the response of an LC, it is quite clear that LC can replicate input behavior.

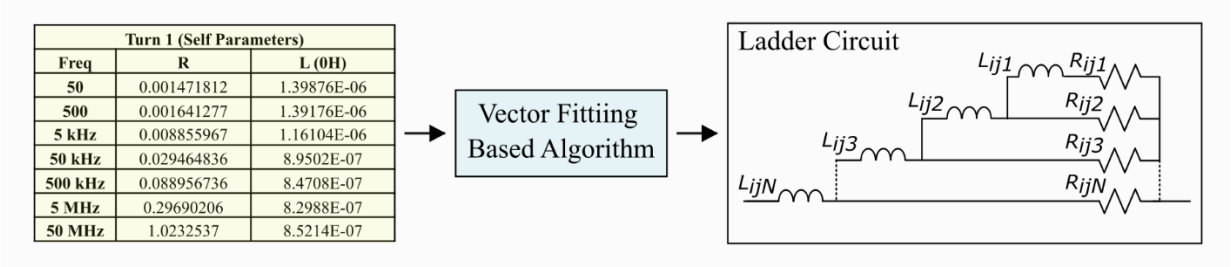

Fig. 2-8 High level overview of procedure to obtain LCs

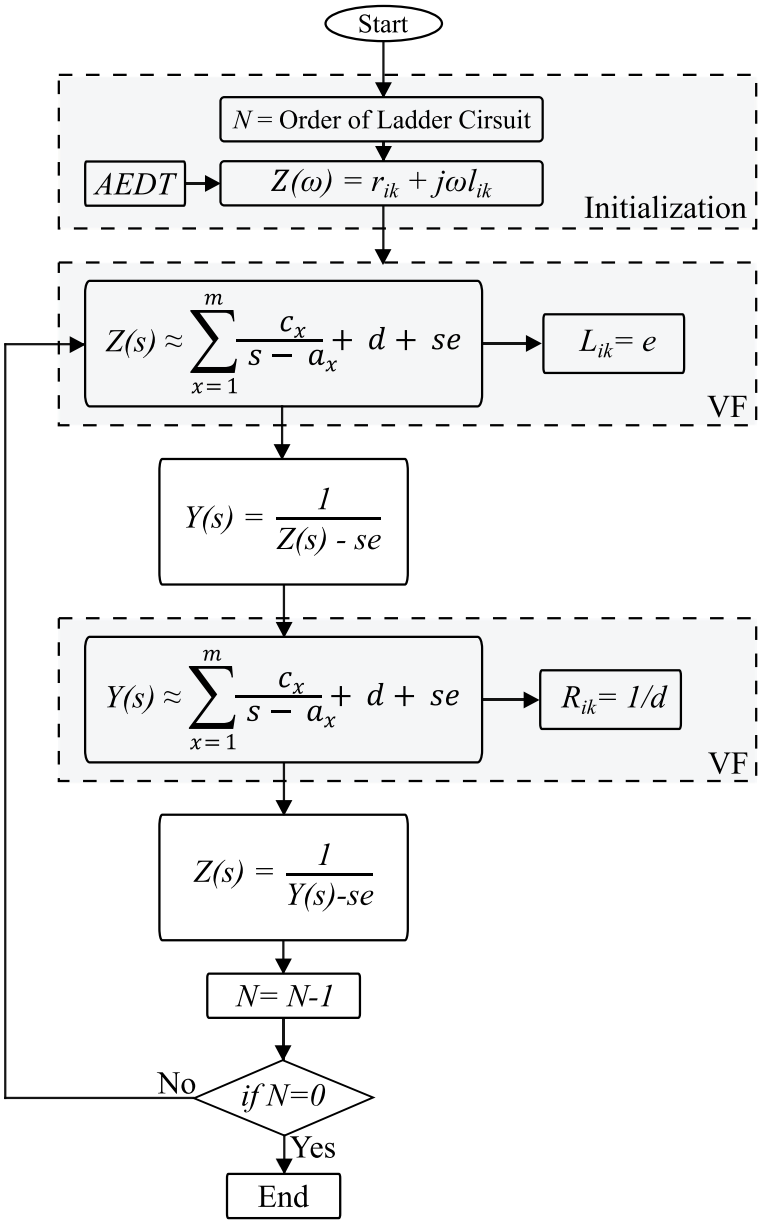

Fig. 2-9 LC parameter computation using VF algorithm

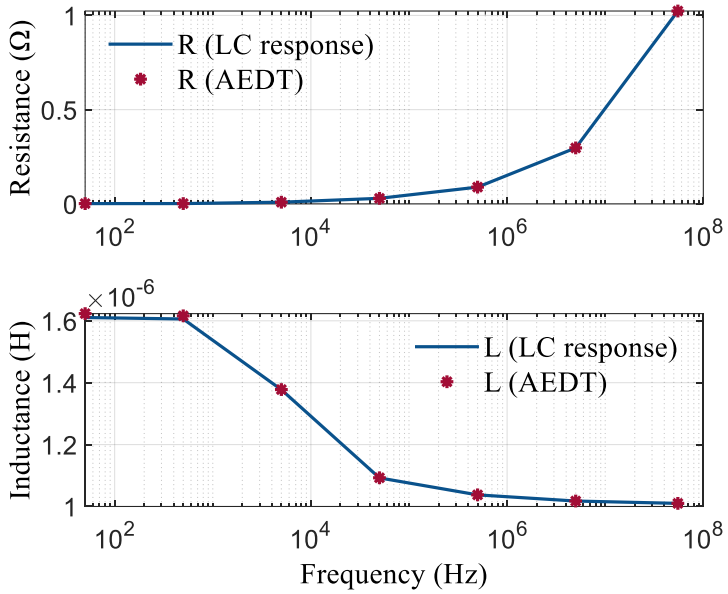

Fig. 2-10 Turn 1 self parameters: LC response vs desired response (parameters from AEDT)

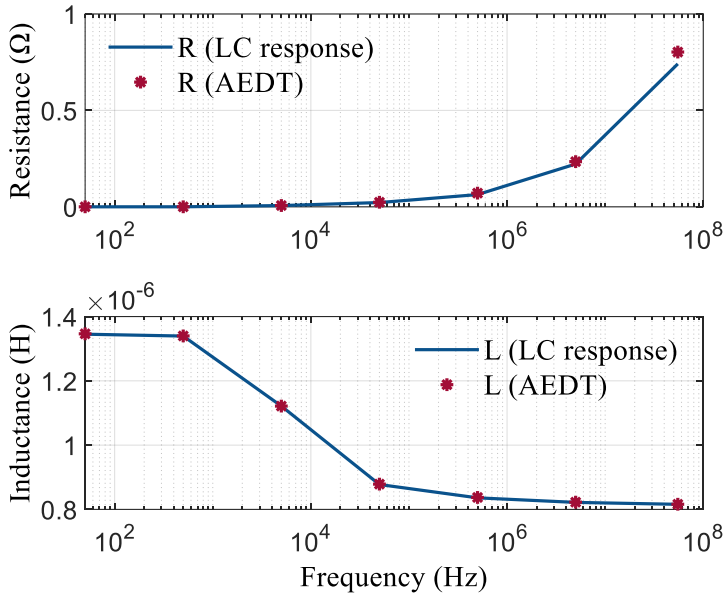

Fig. 2-11 Turn 1 and turn 2 mutual parameters: LC response vs desired response (parameters from AEDT)

To model each coupling this procedure is followed and corresponding LC parameters are obtained. The implementation of the aforementioned VF based algorithm is carried out in MATLAB. The implementation is very challenging due to uncertainties associated with the VF algorithm. Implementation is not straightforward, there is no single code that would work for all the cases. It is crucial to understand and optimize various settings at each level of ladder circuit calculation to ensure that the obtained ladder circuit accurately replicates the desired behavior.

Moreover, the VF algorithm is typically considered as a black box. which is often used in various literature. Ultimately, the critical measure of success for the VF based algorithm is its ability of LC to accurately replicate the desired frequency dependent parameters.

2.5 Experimental Validation: Validation of the Developed HF Winding Model

The developed model has been developed to conduct investigations on insulation degradation and the development of insulation condition monitoring methodologies, which require accurate replication of HF behavior of the winding. To validate the developed model various experiments have been conducted. Various measurements from simulation and experiments have been obtained for comparative analysis of 1) Common mode (CM) and Differential mode (DM) impedances and 2) voltage distribution inside the winding. These comparisons of the CM and DM impedances reflects the parasitic couplings of the winding. Therefore, the comparison of CM and DM impedance from the HF model with the experimental measurement is a common practice to validate the model [53],[54],[91]. This ensures validation of the model over a wide frequency range. On the other hand, other common approach to validate such HF models is through comparison of voltage distribution inside the winding. A typical inverter is applied to the winding and voltages at various locations inside the winding are measured and compared, such comparison validates the model in time-domain.

2.5.1. Comparison of Common mode (CM) and Differential mode (DM) impedances

The CM and DM impedances from both the developed model and experimental setup have been acquired for comparison. The model has been implemented in Matlab/Simulink environment, and the impedances have been acquired using the Impedance Measurement block functionality in Simulink. The impedance measurements from the experimental setup are acquired using OMICRON Lab manufactured Bode100 impedance analyzer. The Bode 100 impedance analyzer can measure the impedance over a frequency range frequency range from 1 Hz to 50 MHz. The complete setup is illustrated in Fig. 2-12, Bode100 impedance analyzer is connected to the stator winding, and the measurement data has been acquired from PC connected to Bode100. As shown in Fig. 2-13, the connections to acquired CM and DM impedances have been made. The CM impedance is measured between the shorted terminals of the winding and stator core. The DM impedance is measured between the terminals of the winding and the stator core kept floating.

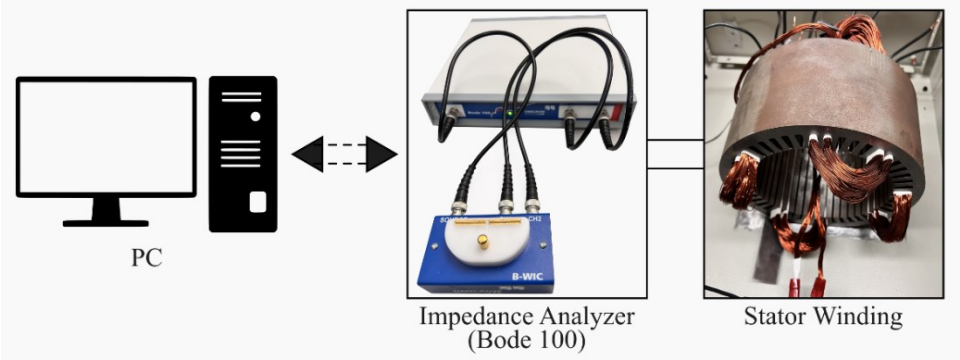

Fig. 2-12 Experimental setup for CM and DM impedance measurement

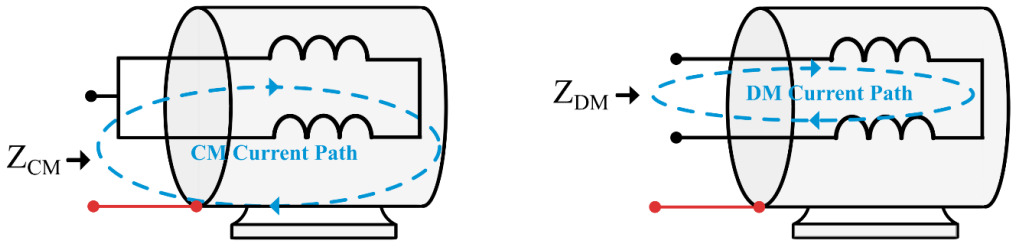

Fig. 2-13 Schematic of CM and DM impedance measurement

The comparison of CM impedances and DM impedances from hardware and simulation is shown in Fig. 2-14 and Fig. 2-15 respectively. The impedances show good agreement, indicating that the developed HF model is accurate. Moreover, it is crucial to note that the resonance and antiresonance frequencies match quite well.

The resonance in electrical circuits is characterized by a significant increase in the circuit's impedance response at a specific frequency, known as the resonance frequency. Conversely, the antiresonance frequency is the frequency where the circuit's impedance response reaches minima. In CM impedance, the first antiresonance frequency (f_{CM_ar1}) from the HF model is at 1.92 MHz while the hardware results show antiresonance at 1.88 MHz. Similarly, the second antiresonance frequencies (f_{CM_ar2}) are also in close proximity, 22.5 MHz from simulation and 19.8 MHz from hardware measurements. In DM impedance, the resonance and antiresonance frequencies can be found in close proximity. For instance, the resonance frequency (f_{DM_r1}) from the HF model is at 2.1 MHz while the measured resonance frequency is at 2.35 MHz. Apart from resonance and antiresonance frequencies, the amplitude of impedance and phase also show great agreement with each other, highlighting the model's capability to replicate the HF behavior of the winding.

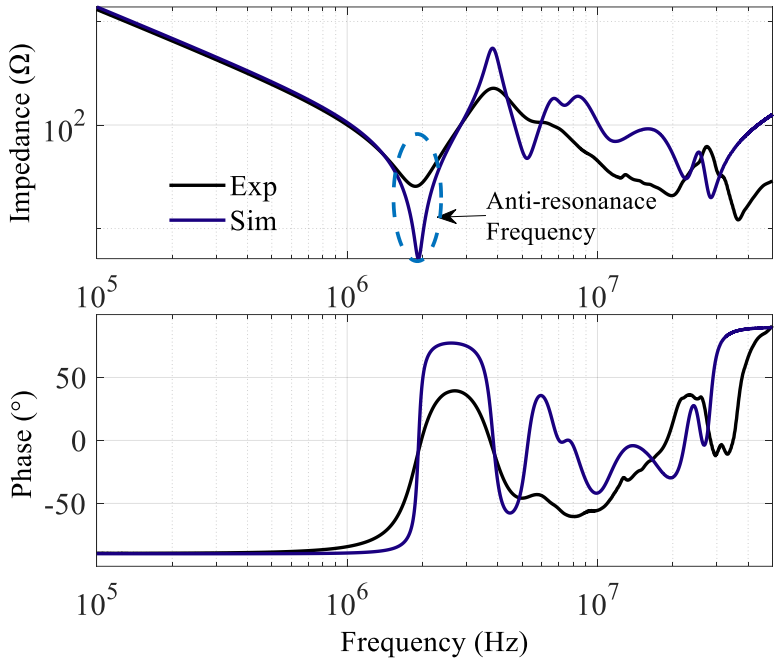

Fig. 2-14 Comparison of CM impedance acquired from MCTL model and hardware

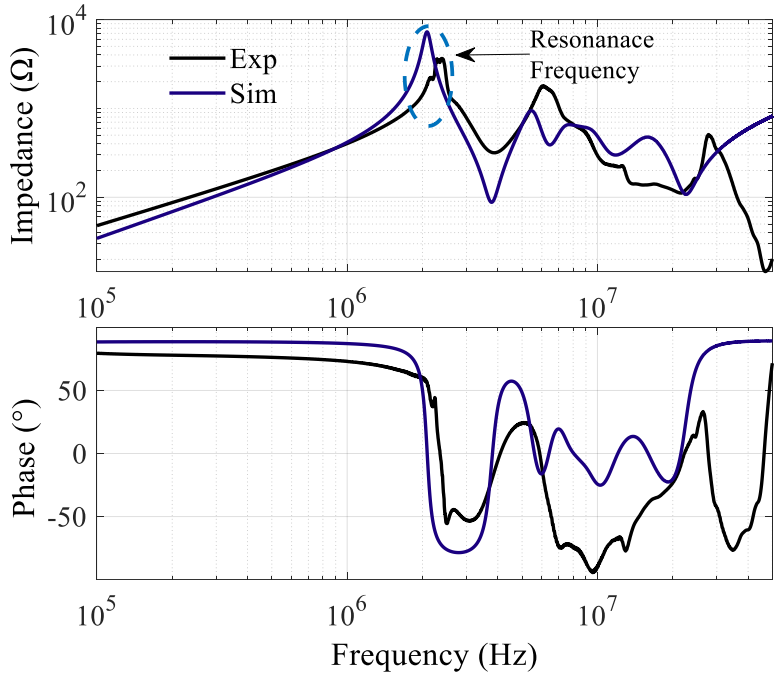

Fig. 2-15 Comparison of DM impedance acquired from MCTL model and hardware

Table 2-3 Comparison of antiresonance and resonance frequencies from simulation and experiment

Impedance	Freq	Experiment	Simulation
CM Impedance	f_{CM_ar1}	1.88 MHz	1.92 MHz
	f_{CM_ar2}	19.8 MHz	22.5 MHz
	f_{CM_r}	3.84 MHz	3.81 MHz
DM Impedance	f_{CM_ar1}	3.87 MHz	3.78 MHz
	f_{CM_ar2}	21.6 MHz	22.6 MHz
	f_{CM_r}	2.35 MHz	2.1 MHz

However, the developed model is not perfect due to uncertainties involved with the modeling and measurement procedure. These discrepancies can be due to the unknown position of wires inside the slot, approximation of dielectric properties of insulation, negligence of nonidealities, lumped end-winding modeling, etc. However, it should be acknowledged the MCTL modeling approach used is considered state-of-the-art and outperforms other modeling approaches [54], [90], [91], [92]. Moreover, even though such discrepancy does impact the time domain model performance, it does not do so in a manner, which significantly impedes the model performance for the purpose of voltage distribution [91]. There could be some improvements made to improve the model. However, this thesis does not focus on the improvement of HF modeling, rather it focuses on the utilization of such a model for investigating the influence of insulation degradation on CM/DM impedances and the development of condition monitoring methodologies. In summary, the CM and DM impedance fairly match with the hardware measurement including resonance frequencies and antiresonance frequencies. Thus, this HF model is utilized for investigations on condition monitoring methods.

2.5.2. Comparison of Voltage Distribution

As discussed, the developed HF model through experiments, a voltage distribution measurement-based approach is used. This involves application of an inverter pulse and measurement of voltages at various locations inside the winding. Thereafter, the measured voltages from experiment and simulation are compared. The experimental setup is shown in Fig. 2-16.

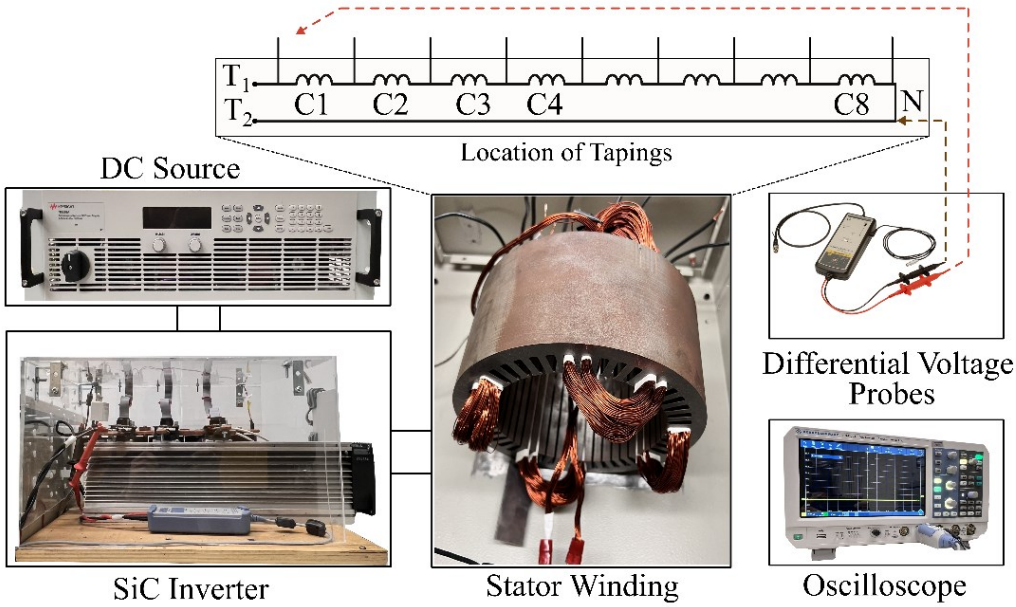

Fig. 2-16 Experimental validation setup for comparison of voltages

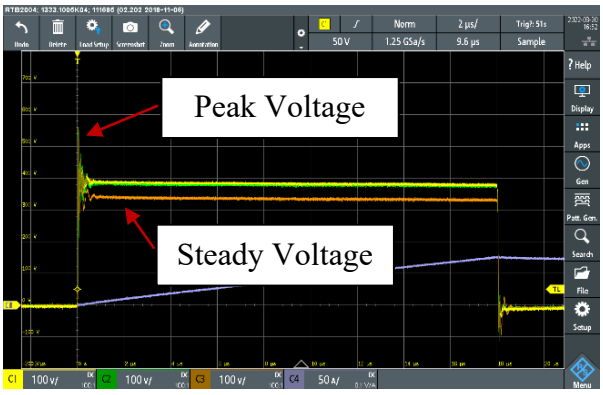

Fig. 2-17 Typical measurement for measured voltages

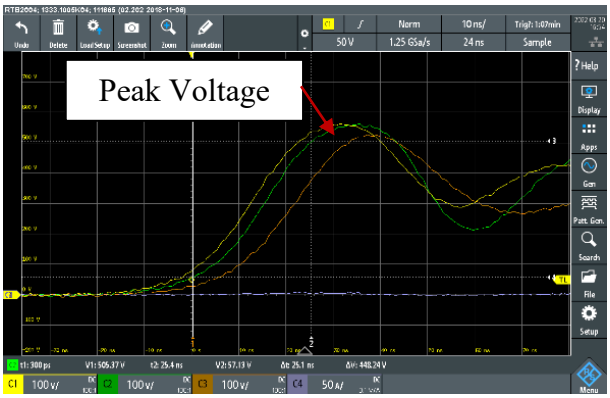

Fig. 2-18 Typical measurement for measured voltages (Enlarged View)

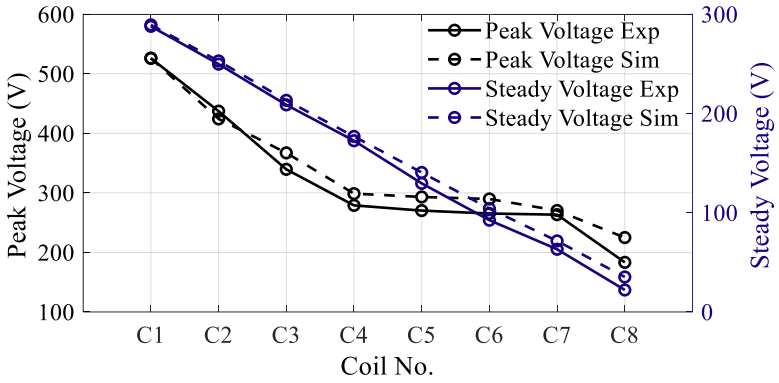

Fig. 2-19 Comparison of peak and steady voltages from simulation and experiment

A high dv/dt (17.7 kV/μs) voltage pulse to the winding using a half-bridge SiC inverter module. The utilized SiC module is Wolfspeed CAB450M12XM3 with a peak voltage rating of 1200V and peak current of 450A. After the application of voltage pulse, voltages at the terminals as well as the at each coil are measured. The voltages have been measured using Yokogawa differential probes with a bandwidth of 100 MHz and measure voltages up to 1400V. The utilized oscilloscope is Rhode & Schwarz RTM3004 with a bandwidth of 500 MHz. Typical measurements of voltages are shown in Fig. 2-17 and 2-18. The peak voltage refers to the maximum voltage measured, while steady voltage corresponds to the voltage level after initial oscillations in the voltages have been damped. After acquisition of these voltage from experiment, the same applied voltages as in the experiment is fed to the HF model to obtain voltages at each coil of the winding. Obtained voltages at each coil through experiment and simulation are compared with each other, and results are shown in Fig. 2-19 and Table (2.4). The steady and peak voltages match quite well, indicating that the developed HF model is accurate. As discussed, these exists some discrepancies due to the unknown position of wires inside the slot, approximation of dielectric properties of insulation, negligence of nonidealities, lumped end-winding modeling, etc. These are some potential improvements that can be made.

Table 2-4 Comparison of peak and steady voltages from simulation and experiment

Applied Pulse dv/dt	**Coil No.**	**Peak Voltage (V)**		**Steady Voltage (V)**	
		Simulated	**Experiment**	**Simulated**	**Experiment**
dv/dt: 17.7 kV/μs	C1	526.074	526.07	289.272	287.79
	C2	424.1954	437.21	252.9208	249.71
	C3	367.1785	339.55	213.22	208.69
	C4	298.7104	279	176.8681	172.56
	C5	293.1471	270.22	140.5151	129.59
	C6	289.7331	265.33	104.1624	92.48
	C7	270.3356	263.38	71.57419	63.18
	C8	224.9542	183.3	35.22583	22.17

2.6 Summary

This chapter briefly discusses the HF modeling of stator winding using the multiconductor transmission line modeling (MCTL) approach, which has been further utilized for the investigations on condition monitoring methodology. In order to simplify modeling and validation, a winding with 8 coils or 24 turns is modeled, which adequately serves the purpose of investigating online insulation condition monitoring methodologies. The developed model incorporates frequency dependent resistance and inductances, leading to the accurate representation of the HF behavior of the winding. A comparative study was carried out to validate the developed model against experimental results. The comparative analysis covered common-mode (CM) impedance, differential-mode (DM) impedance, and peak and steady-state voltages at various coils. The results show a good match between simulation and hardware. However, this model shows some discrepancies due to various uncertainties associated with the modeling procedure. Nonetheless, it's crucial to acknowledge that the model demonstrates a reasonable level of accuracy when compared to actual hardware measurements, particularly in terms of matching resonance and antiresonance frequencies, which proves the model's effectiveness in capturing key electrical characteristics. Consequently, despite the identified limitations, this high-frequency (HF) model proves to be crucial for investigations on condition monitoring methods. Comprehensive investigations on the influence of various types of insulation degradation on transient line current and corresponding frequency spectrum can be conducted which would help in developing accurate condition monitoring methodologies.

Chapter 3: Utilization of Antiresonance Oscillations for Insulation Condition Monitoring

As discussed, one of the limitations in existing literature is that there exists a significant knowledge gap in understanding of the influence of insulation degradations on the HF line current. There is a need to address this knowledge gap through investigations, and learning can be further utilized to develop appropriate condition monitoring methodology. Hence, his chapter presents comprehensive investigations on the influence of different insulation degradations on the HF line current. The investigations aim to identify the underlying mechanisms and patterns associated insulation degradation and HF line current. To conduct these investigations, HF stator winding model presented in the previous section has been utilized. Based on the investigations results, utilization of the dominant antiresonance oscillations in line current for condition monitoring has been proposed. The first subsection introduces characteristics of the oscillation in the line current due to inverter switching. The second subsection presents investigations on the influence of various degradations on the line current and CM impedances, proposing the utilization of dominant oscillation in condition monitoring.

3.1 Dominant High Frequency Line Current Oscillations

The HF current oscillations during the switching of power electronics devices carry information related to the HF behavior of the winding. This information can be extracted using the PWM voltage pulses from the inverter, these pulses can be considered as HF excitation which spreads up to a maximum frequency of $f_{max} = 1/\min(t_r, t_f)$. Here, t_r is rise time and t_f are and fall time of the PWM pulse. A typical PWM pulse and corresponding spectral envelope are show in Fig. 3-1. A typical PWM pulse from an inverter can be considered as an asymmetrical trapezoid as illustrated in in Fig. 3-1. The key properties that define such trapezoid pulse are the rise time (t_r), fall time (t_f), duty ratio (D), switching period (T). The corresponding spectral envelope is shown in Fig. 3-1. The spectral envelope can be mainly divided into three regions. In the first region, the amplitude remains constant up to frequency of $f_{sw}/\pi D$, which is mainly the function of switching frequency f_{sw} and duty ratio. In the next region, the amplitude reduces at the rate of -20db/dec as the frequency increases. This decrease is up to a frequency of $1/\pi t_r$, hence mainly

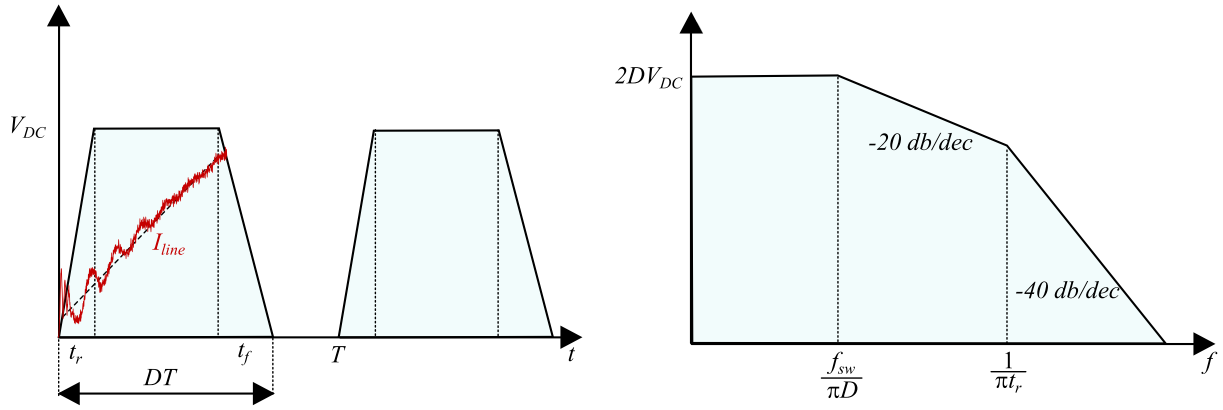

Fig. 3-1 Typical PWM inverter pulse and corresponding spectral envelop

determined by the rise time of the pulse. In the third region, the amplitude decreases even faster at the rate of -40db/dec and extends up to frequency of $1/\min(t_r, t_f)$. However, as a rule of thumb, typically this maximum frequency is considered to be $1/(\pi \cdot \min(t_r, t_f))$ as the spectral component after this frequency are insignificant. Hence, the rise and fall times are critical parameters as they determine the highest frequency components present in the PWM signal. A shorter rise or fall time results in higher frequency components. Hence, a PWM pulse works as a HF excitation which can be utilized to extract the information on the HF impedance of the winding. This can be achieved through understanding the HF line current and it's oscillations behavior due to the application of such PWM voltage pulse. The HF excitation to the winding induces the resultant line current to contain HF component which are function of CM and DM impedances. To conduct the investigations, the HF stator winding model have been utilized. The illustration of the setup is shown in the Fig. 3-2, it contains a half-bridge inverter to apply a PWM voltage excitation pulse (V_{PWM}) to the winding and the HF line current i_{line} is measured. Here, i_{line} rises as a steady rate and there exists some oscillations, which can be represented by equation (3.1).

$$i_{line}(t) = i_{trans}(t) + \frac{1}{L_M}\int_0^t V_{PWM}(t)\, dt \tag{3.1}$$

Here, i_{line} is the line current that rises at a steady rate due to the winding's inductance L_M, V_{PWM} is voltage excitation pulse, and i_{trans} represents the high frequency current which mainly represents current through the high-frequency CM and DM coupling paths. Hence, i_{line} can be utilized to extract the information on the CM and DM impedances.

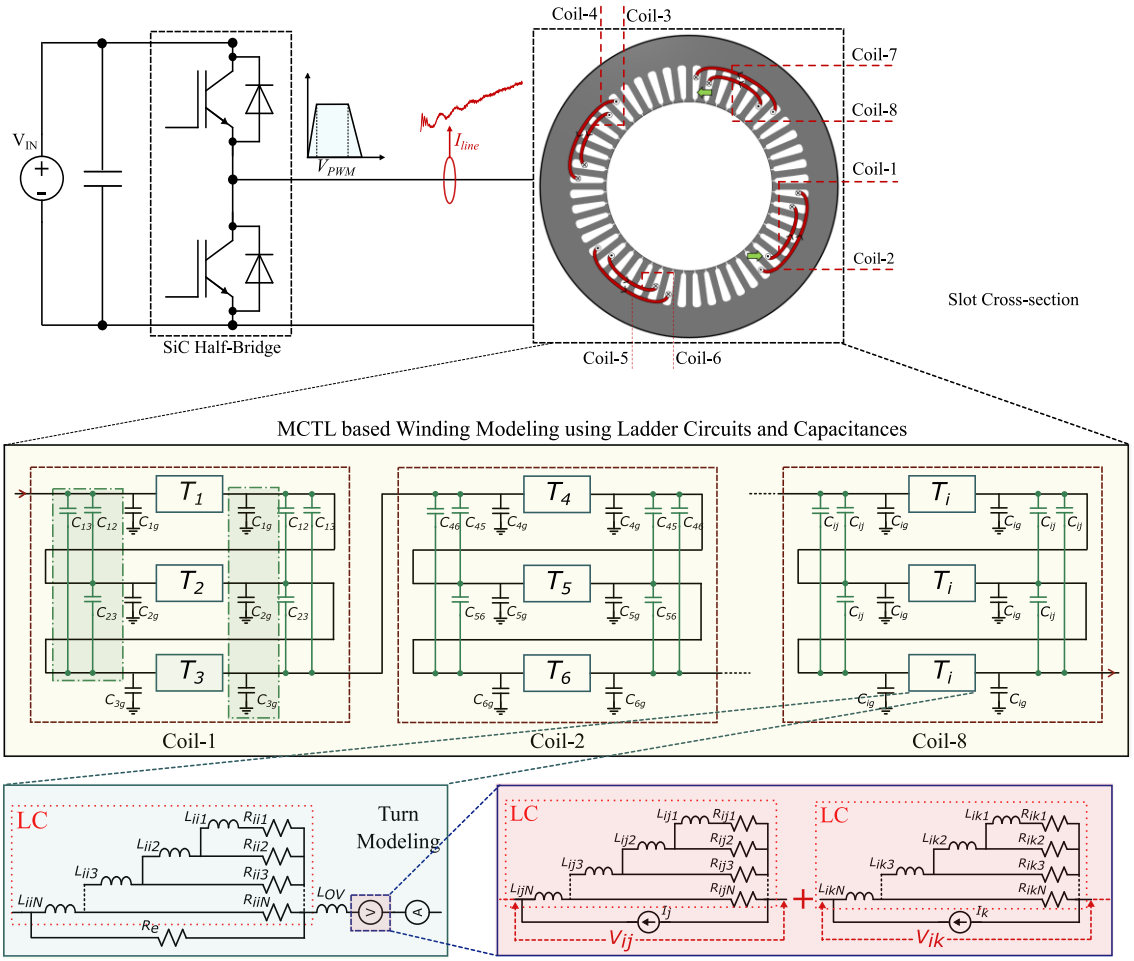

Fig. 3-2 Prominent oscillations in i_t and i_{trans} during inverter switching

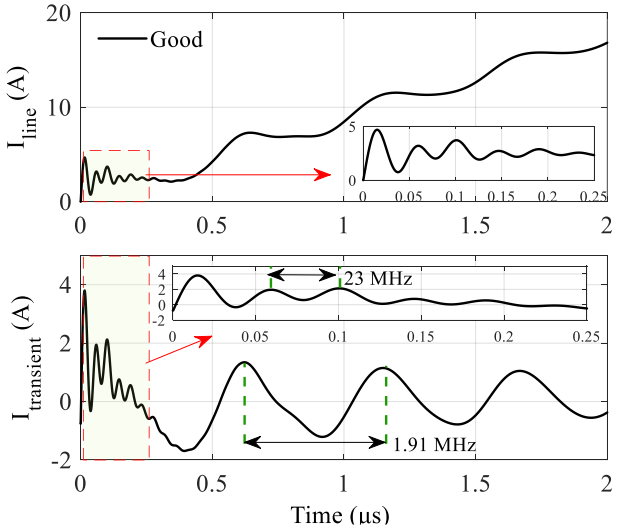

Fig. 3-3 Prominent oscillations in i_{line} and i_{trans} during inverter switching

To extract i_{trans} from, firstly linear trend in the current needed to be captured and mitigated. A steady increase in i_{line}. Fig. 3-3 shows i_{line} and i_{trans} obtained, the prominent oscillations can be clearly observed in both the currents. first-order polynomial is sufficient to capture this trend, this is represented by equation (3.2). In MATLAB, the coefficients p_0 and p_1 can be determined using the 'polyfit' function, which can fit a first-order polynomial to i_{line}. Once the coefficient p_0 and p_1 are obtained, the transient current i_{trans} can be obtained using equation (3.3), which essentially subtracts the linear trend from the i_{line}.

$$f(t) = p_1 t + p_0 \tag{3.1}$$

$$i_{trans}(t) = i_{line}(t) - p_1 t - p_0 \tag{3.2}$$

As shown in Fig. 3-3, the obtained transient current i_{trans} can be characterized by two prominent oscillations. The first is the HF oscillations observed in the beginning and the second is the subsequent low frequency (LF) oscillation. The HF oscillations oscillate at 22.5 MHz, corresponding to the second antiresonance frequency (f_{CM_ar2}) of the CM impedance. The LF oscillations oscillates at 1.92 MHz, the first antiresonance frequency (f_{CM_ar1}) of the CM impedance. This oscillatory behavior has significant potential for insulation condition monitoring. By understanding the relationship between these oscillations and insulation degradation, insulation condition monitoring strategies can be developed. However, the existence and nature of this relationship require thorough investigation to establish a robust correlation. This chapter presents such investigations using the developed HF model

3.2 Analysis of Influence of TT and GW Insulation Degradation on the CM/DM Impedance Spectrum and HF Line-current

This subsection presents analysis on the influence of various degradation scenarios on the CM impedance, line current i_{line} and transient current i_{trans}. Using the HF winding model, both frequency and time domain analysis have been conducted for various insulation condition scenarios, including: 1) good insulation 2) GW insulation degradation 3) TT insulation degradation 4) overall degradation where both TT and GW insulation degrades. As discussed in the Chapter 1, increase in capacitance is the most common symptom of degradation, this increment can be up to 40-50% before failure. Hence, this section presents a comprehensive analysis of the implication of aforementioned insulation condition scenarios with varying degradation severity ranging from 10% to 40% on CM impedance, line current i_{line} and transient

current i_{trans}. The analysis has been done using the HF model. Firstly, the analysis begins under good insulation conditions which serves as the baseline. The capacitances in the model kept the same as determined using an electrostatics solver in AEDT during the model development stage. Thereafter, other degradation scenarios are simulated for varying degradation severity. To simulate TT degradation scenario, where on the turn insulation or the insulation over the wires degrade, the values of the capacitances representing TT insulation are increased by 10% to 40%. Similarly, to simulate GW degradation, the capacitances corresponding to GW insulation are adjusted to reflect the same range of degradation severity. In the overall degradation scenario, both TT and GW insulation are simultaneously degraded. This has been achieved through adjustment of capacitances representing both TT and GW insulation are increased by 10% to 40%. For each of the degradation case, the frequency domain and time domain analysis have been conducted. Frequency domain analysis reveals how the spectrum, resonance and antiresonance frequencies get affected with increasing capacitance due to insulation degradation. This is critical for understanding the high-frequency behavior of the winding and identifying specific frequency ranges where degradation effects are most pronounced. The frequency domain analysis comprises an investigation on both CM and DM impedances. However, this subsection focuses on CM impedance only. The impedance measurement functionality in MATLAB/Simulink environment have been utilized to measure CM impedance, it is measured between the shorted terminals of the winding and stator core. In the time domain, line current i_{line} and transient current i_{trans} are acquired and investigated for each degradation case. The analysis shows how the amplitude and frequency of these currents change with varying degrees of insulation degradation, providing insights into the influence of degradation on these current. The investigations elucidate the relationship between insulation degradation and its impact on CM impedance, i_{line} and i_{trans}. By understanding these relationships, effective insulation condition monitoring methodologies can be developed.

3.2.1. Analysis of CM impedance for Various Degradations

For the aforementioned degradation scenarios, Fig. 3-4 illustrates CM impedance for TT degradations, Fig. 3-5 for GW degradations, and Fig. 3-6 for overall degradations. Each figure contains two subfigures: (a) shows the CM impedances for different levels of degradation, while (b) shows the deviation from the good insulation condition. For the aforementioned degradations, analysis from these plots are crucial as they provide detailed insights into how CM impedance

varies across different degradation levels, and their deviation from the baseline good insulation condition is clearly depicted.

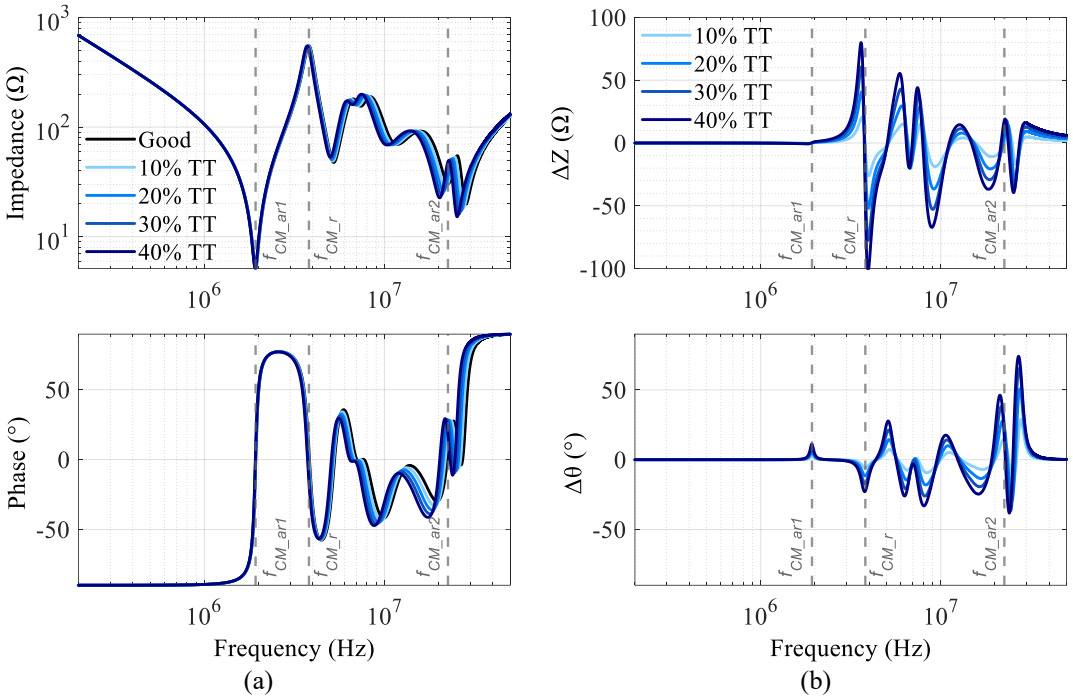

Fig. 3-4 TT degradation: (a) CM impedances for various degradation scenarios (b) Deviation in CM impedances due to degradation

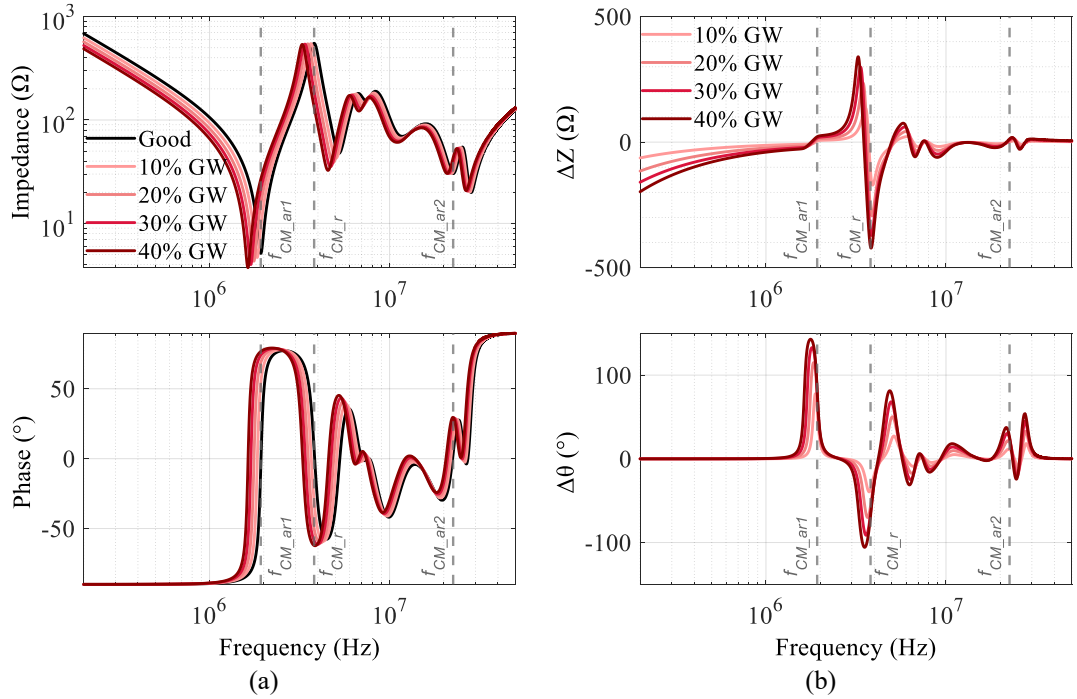

Fig. 3-5 GW degradation: (a) CM impedances for various degradation scenarios (b) Deviation in CM impedances due to degradation

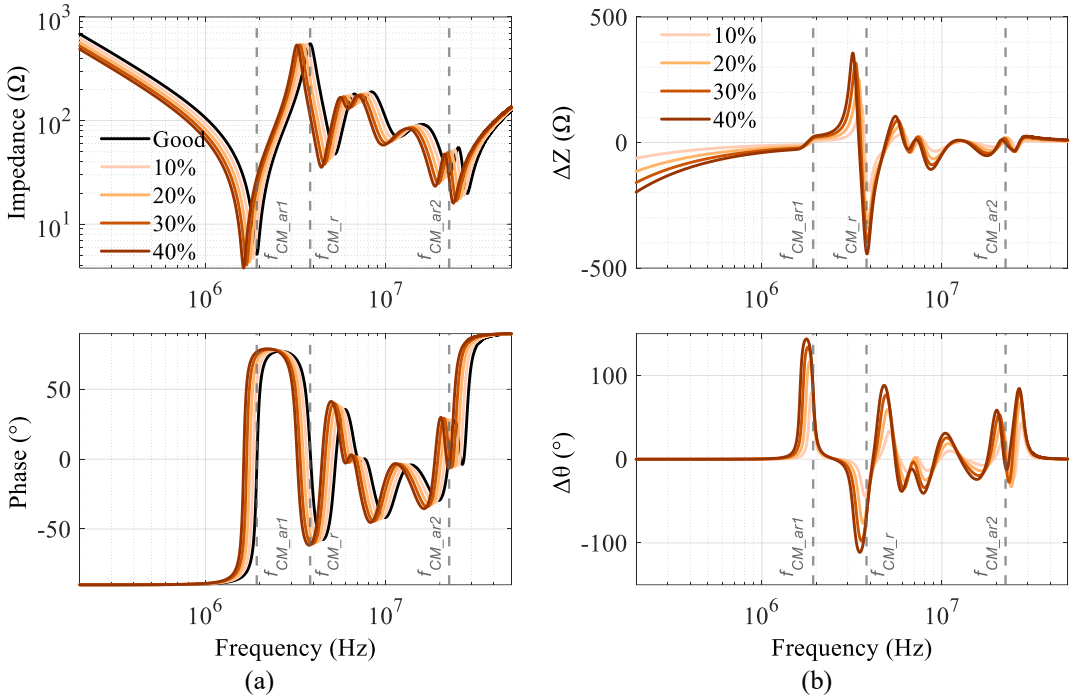

Fig. 3-6 Overall degradation: (a) CM impedances for various degradation scenarios (b) Deviation in CM impedances due to degradation

For good insulation scenario, as seen from the CM impedance, it exhibits the f_{CM_ar1} at about 1.92 MHz, and f_{CM_ar2} at about 22.5 MHz. For TT degradation scenarios, the CM impedances and deviation in CM impedance from the good insulation scenario shows deviations in the amplitude (ΔZ) throughout the CM spectrum for all degradation severities. Below 2.5 MHz, these deviations are relatively minor while the most deviation can be observed at about resonance frequency (f_{CM_r}). This indicates that the low-frequency components of the CM impedance are less sensitive to TT degradation. Moreover, minor deviation near the f_{CM_ar1}, these changes are comparatively smaller than those at the resonance frequency, they are still indicate some sensitivity to TT degradation. In the 3-50 MHz range, more significant changes can be observed, including at f_{CM_ar2}. With increasing levels of degradation severity, more deviation can be observed. The increase in amplitude deviations as the degradation severities increase indicates that this frequency range could be critical in detecting and assessing TT insulation degradation. For GW degradation scenarios, the results are shown in Fig. 3-5 (a) and 3-5 (b). Analysis shows similar findings where noticeable deviation can be found throughout the frequency range. However, the deviations are more substantial than in the TT degradation scenarios, particularly below 2.5 MHz. Moreover, the deviation near the resonance frequency is

about four times more compared to TT degradation scenarios. This indicates a greater sensitivity of the low-frequency components to GW degradation. Unlike the TT degradation scenario, significant deviation near to the f_{CM_ar1} and f_{CM_r} can be observed. Near to these frequencies, the deviation is significantly greater compared to the TT degradation scenarios. This suggests potential that GW degradation has a much more pronounced effect on the impedance than the TT degradation. However, a contrasting trend near to the f_{CM_ar2} can be observed, where the deviation is not as significant as in the TT degradation scenario. This suggests that GW degradation impacts the frequency components near the f_{CM_ar2} differently compared to TT degradation, with less pronounced changes in this frequency range. Fig. 3-6 (a) and Fig. 3-6 (b) shows the results for the overall degradation, a similar trend as in the GW degradation can be found. However, due to the inclusion of TT degradation, comparatively more deviation near to the f_{CM_ar2} can be observed. Due to the inclusion of TT degradation, there is comparatively more deviation near f_{CM_ar2}. This indicates that overall degradation affects both the high and low-frequency components more significantly than either TT or GW degradation alone. Key takeaways from frequency domain analysis are: 1) all three degradation scenarios cause deviation in the impedance throughout the frequency spectrum. 2) identifying the frequency range that uniquely represents the TT degradation is extremely difficult, this makes simultaneous SOH determination of TT and GW challenging. 3) Only GW degradations cause significant deviation below the frequency f_{CM_ar1}, unlike TT degradations. 4) GW degradations cause significant reduction in f_{CM_ar1} and f_{CM_r}, with noticeable effect on f_{CM_ar2}. 5) TT degradations lead to significant reduction only in f_{CM_ar2}, with negligible deviations in f_{CM_ar1} and f_{CM_r}. The frequency domain analysis provides good intuition of deviation in impedance spectrum, resonance frequency and antiresonance frequencies associated with various insulation degradation scenarios. However, it is importation to assess the ability of i_{trans} in capturing crucial information for condition monitoring. Given that i_{trans} is sensitive to both CM and DM impedances, the spectrum of i_{trans} would reflect both CM and DM impedances. Therefore, brief analysis on potential utilization of i_{trans} for condition monitoring is presented.

3.2.2.Analysis of HF line Current for Various Degradations Considering CM Impedance

For the aforementioned degradation scenarios, a PWM voltage excitation pulse V_{PWM} of 500V and 20 ns of rise time is applied to the HF winding model and the line current i_{line} is obtained.

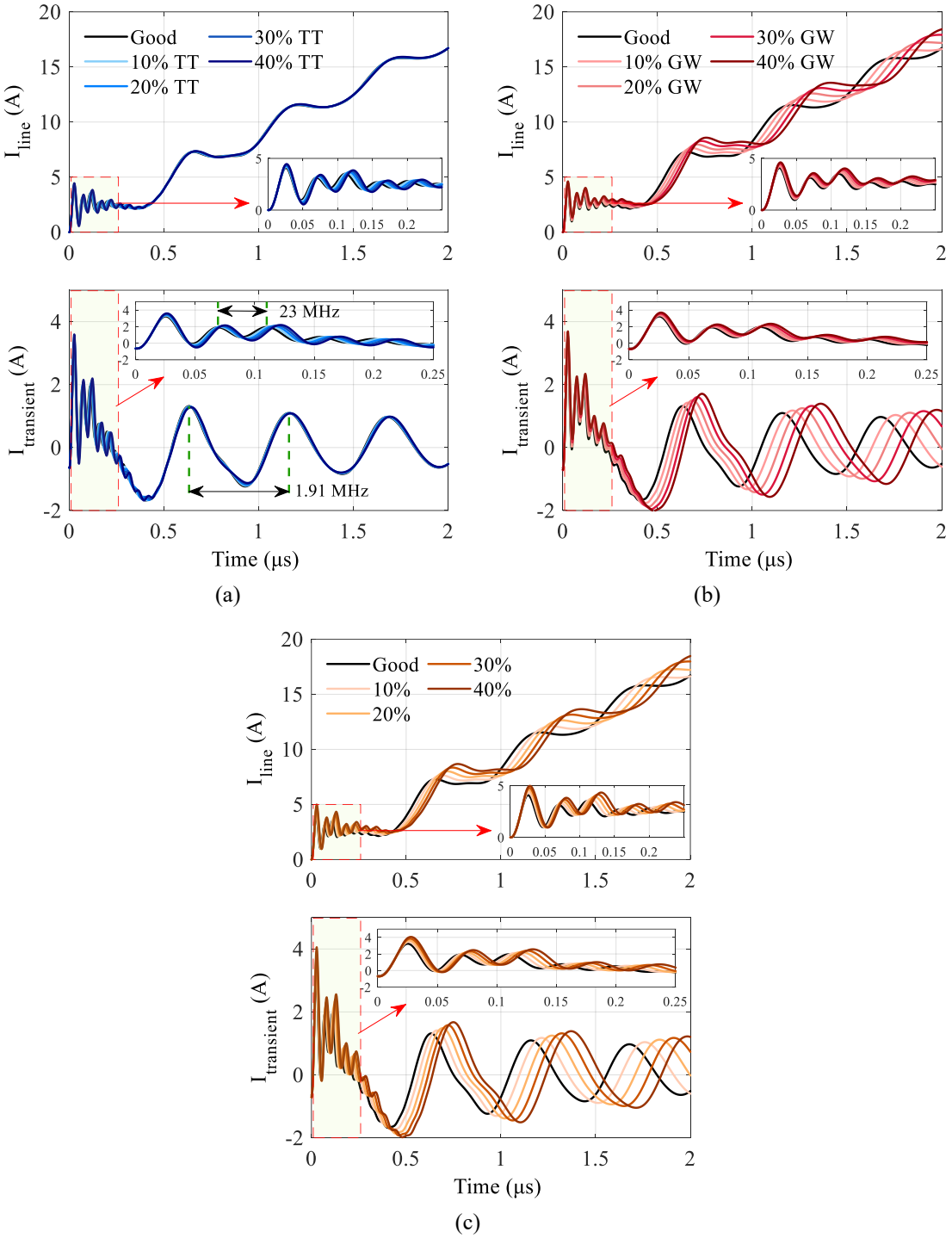

Fig. 3-7 Current i_t and i_{trans} for various degradation scenarios. (a) TT degradation (b) GW degradation (c) Overall (TT and GW) degradation

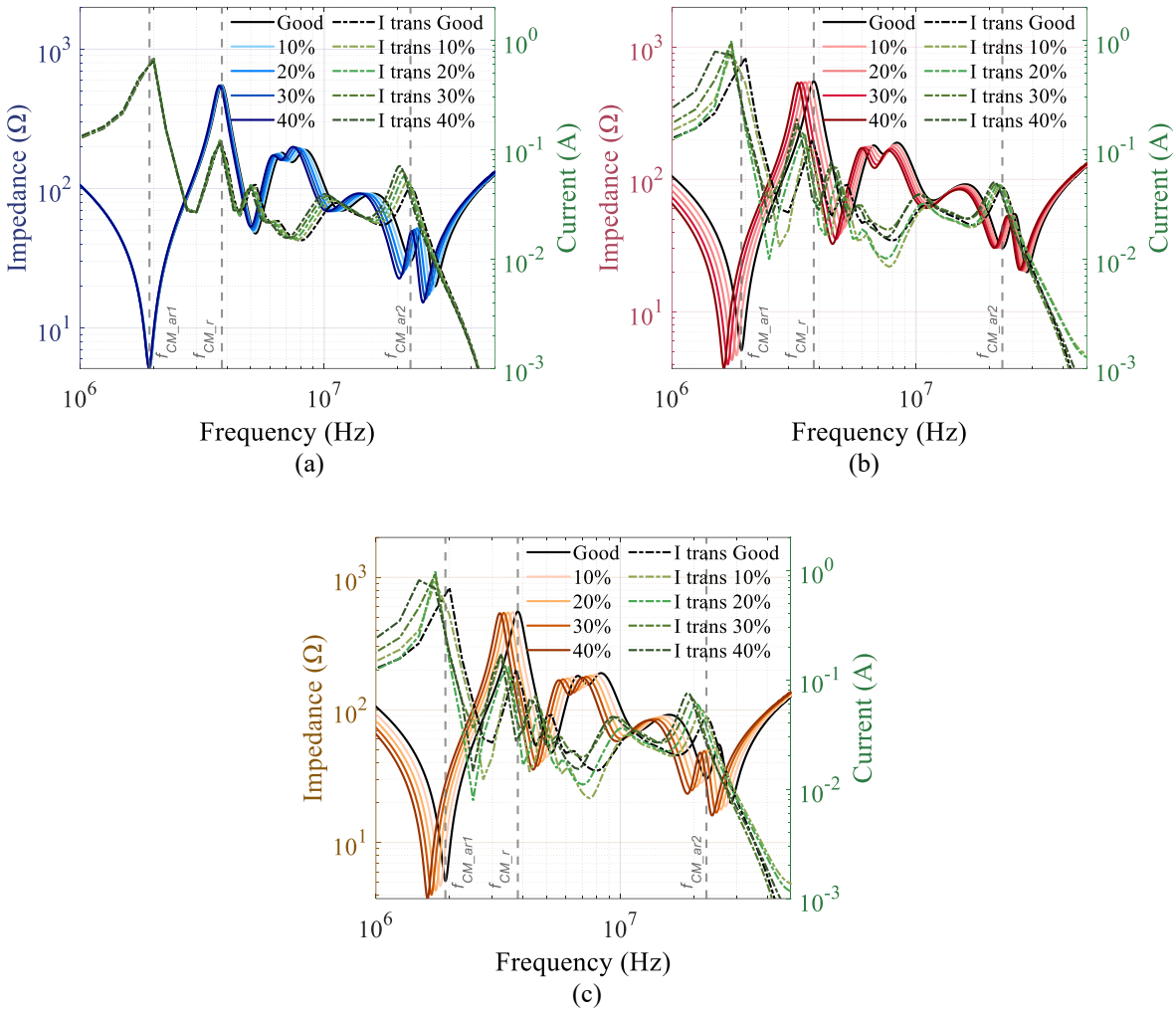

Fig. 3-8 CM impedance and FFT spectrum of i_{trans} for degradation scenarios (a) TT degradation (b) GW degradation (c) Overall (TT and GW) degradation.

This current is further processed to obtain i_{trans}, the currents are shown in Fig. 3-7. Moreover, the FFT spectrum of superimposed with CM impedances is presented in Fig. 3-8. As discussed, the prominent oscillations in current i_{trans} are occurring at the antiresonance frequencies of the CM impedance. For good insulation scenario, i_{trans} depicts HF oscillations at about 23 MHz and LF oscillations at about 1.91 MHz, corresponding to the antiresonance frequencies. More specifically, the initial HF oscillations are at f_{CM_ar2} while the following LF oscillations are at f_{CM_ar1}. For TT degradation, with increasing levels of degradation severity the HF current amplitude increases while the oscillation frequency decreases from 23 MHZ to 20.9 MHz. Contrastingly, the LF oscillations barely show any deviations. This behavior of i_{trans} reflects the findings from the frequency domain analysis. Specifically, with increasing TT degradation

severity, the f_{CM_ar2} and impedance amplitude both decrease, while the f_{CM_ar1} remains constant and the amplitude of impedance increases. For increasing severity of GW degradation, the transient current i_{trans} shows deviations in both HF and LF oscillations. The LF oscillation frequency decreases from 1.91 MHZ to 1.6 MHz and the amplitude of current shows some increase as the degradation severity increases. The HF oscillation frequency decreases from 23 MHZ to 21.1 MHz, but the impact is less significant compared to the LF range. The deviations observed in the current clearly correlate with the behavior of CM impedances. For the overall degradation scenarios, the i_{trans} shows cumulative effects as both TT and GW insulations are degraded. The FFT spectrum shows the combined effects on the CM impedance, with significant deviations across the entire frequency range including antiresonance frequencies f_{CM_ar1} and f_{CM_ar2}. The decrease in these frequencies and increase in amplitude can be observed as the degradation increases.

In summary, the analysis of i_{trans} for various degradation scenarios reveals distinct impacts on HF and LF oscillations, reflecting the corresponding changes in CM impedance. Moreover, these findings consolidate that the i_{trans} and the prominent oscillations can be utilized the extract information on CM impedance, especially around the antiresonance frequencies. Moreover, the temporal isolation of prominent oscillations within the time domain is crucial, simplifying the extraction of information related to both the first and second antiresonances. Hence, characteristic behavior of i_{trans} make it invaluable for the development of condition monitoring methodology.

3.3 Analysis of DM Impedance for Various Degradations

This subsection presents an analysis on the influence of various degradation scenarios on the DM impedance, line current i_{line} and transient current i_{trans}. Fig. 3-9, Fig. 3-10 and Fig. 3-11 illustrate the impedances for various degradations and deviation in the impedance from good insulation scenario.

The change DM impedance for TT degradation has been presented in Fig. 3-9 (a). Firstly, it is crucial to understand the behavior for the scenario when there is no degradation or when the insulation is good. As seen from the DM impedance, it exhibits the resonance frequency (f_{DM_r}) at about 2MHz, first anti-resonance frequency (f_{DM_ar1}) at about 3.9MHz and second anti-

resonance frequency (f_{DM_ar2}) at about 22.5 MHz. The change DM impedance due to TT degradation is shown in Fig. 3-9, the deviation in the amplitude of impedance throughout the spectrum can be observed. Here, it is crucial to note that the deviations in the resonance frequency are comparatively smaller that the deviations in the antiresonance frequencies. However, the most deviations in the amplitude can be found at near the resonance f_{DM_r}. For varying levels of GW degradation, the DM impedances are shown in Fig. 3-10, the most significant deviation in the impedance is observed near the f_{DM_r} at around 2.1 MHz. Moreover, compared to the TT degradations, more significant decrease in the resonance frequency can be observed. The deviations in both resonance and anti-resonance frequencies can be observed. These deviations in f_{DM_r} and f_{DM_ar1} are more pronounced compared to those seen in TT degradation scenarios, while the deviation in $f_{DM_ar1}$are comparative less. As discussed in the previous section, the anti resonance frequencies f_{DM_ar1} and f_{DM_ar2} behave the same way as found in the CM impedance investigations. The influence of GW degradation on f_{DM_r} could be potentially utilized for condition monitoring. For overall degradation scenarios, the combined effect of TT and GW degradation can be observed. Where the deviations in the resonance and antiresonance frequencies are more pronounced.

The investigations on DM impedance highlight the potential for utilizing resonance frequencies for condition monitoring. These findings from DM impedance support and strengthen the results from CM impedance. The clear changes at the resonance and anti-resonance frequencies show their potential for effective condition monitoring. While the potential for utilizing i_{trans} and anti resonance oscillations for condition monitoring has been explored with respect to CM impedance, it is equally important to evaluate its effectiveness in relation to DM impedance. Moreover, it is crucial to investigate if there exist resonance oscillations in i_{line} and if they can be utilized for condition monitoring. Therefore, the following section presents a brief analysis on DM impedance characteristics and i_{line} for condition monitoring.

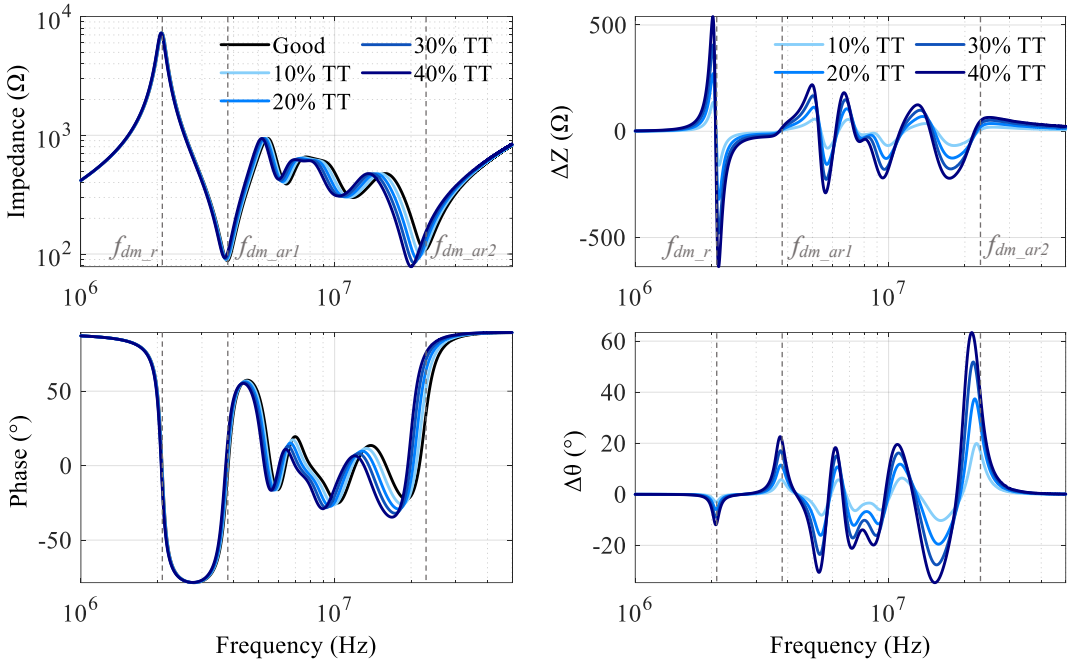

(a) (b)

Fig. 3-9 TT degradation: (a) DM impedances for various degradation scenarios (b) Deviation in DM impedances due to degradation

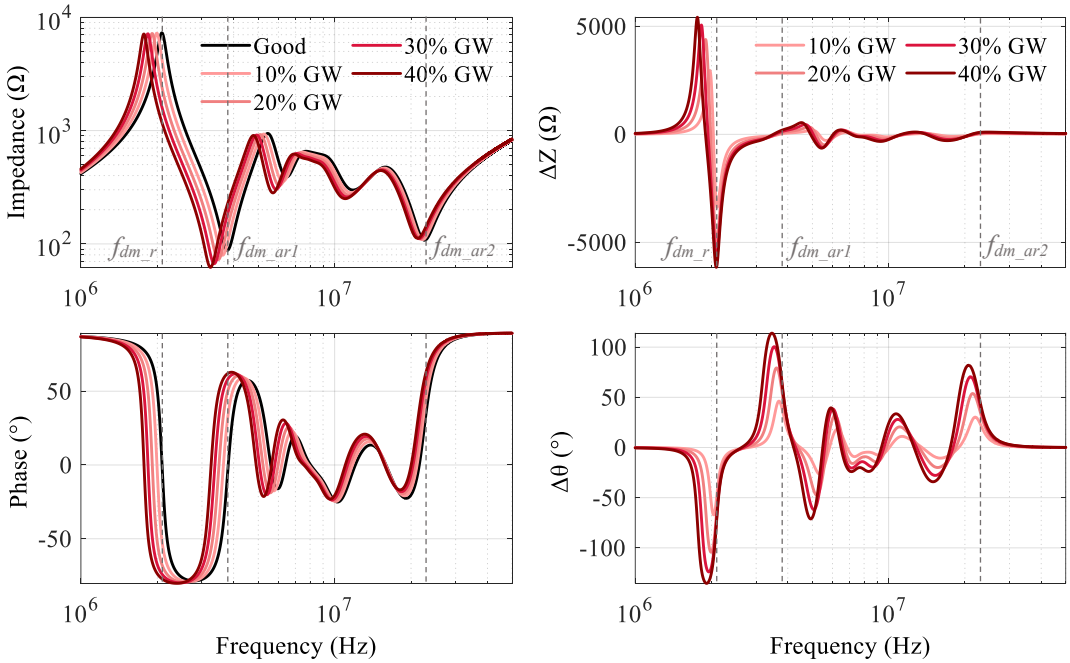

(a) (b)

Fig. 3-10 GW degradation: (a) DM impedances for various degradation scenarios (b) Deviation in DM impedances due to degradation

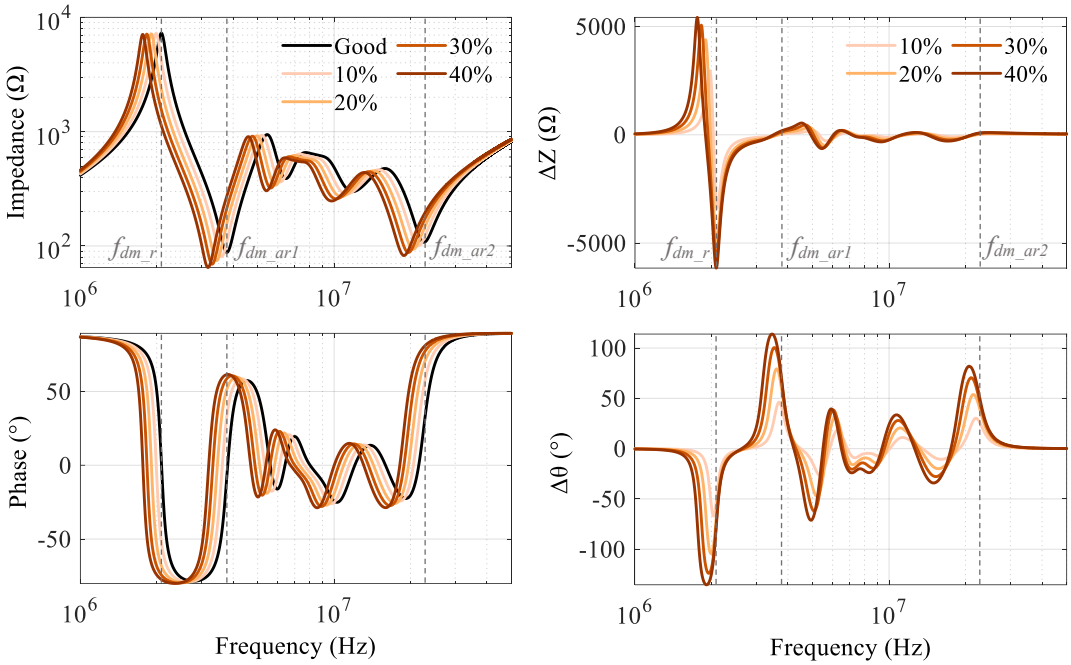

Fig. 3-11 Overall degradation: (a) DM impedances for various degradation scenarios (b) Deviation in DM impedances due to degradation

3.3.1.Analysis of HF line Current for Various Degradations Considering DM Impedance.

This subsection presents analysis on the influence of various degradation scenarios on the DM impedance and transient current i_{trans}. For various degradation scenarios, the FFT spectrum of i_{trans} superimposed with DM impedances are presented in Fig. 3-12. The deviation in oscillations in the i_{trans} have been already discussed previously. A similar correlation on the anti resonance oscillations and DM impedance is evident. However, it is crucial to note that oscillations at the resonance frequency are not observed. The dominant oscillations are only at the antiresonance frequencies, these oscillations and deviations observed in the current clearly correlates with the behavior of DM impedances. As determined from the frequency domain investigations, the FFT spectrums clearly show that the antiresonance oscillation in i_{trans} clearly correlates with the behavior of DM impedances. These findings consolidate that the i_{trans} and the dominant oscillations at antiresonance can be utilized to extract the information on CM/DM impedance at the antiresonance frequencies. Moreover, as the degradation increases the decrease in the resonance frequency and increase in the amplitude clearly show correlation with the degradation. Moreover, the temporal isolation of dominant oscillations within the time domain

plays a crucial role in simplifying the extraction of information related to both the first and second antiresonances. Hence, characteristic behavior of i_{trans} make it invaluable for insulation condition monitoring.

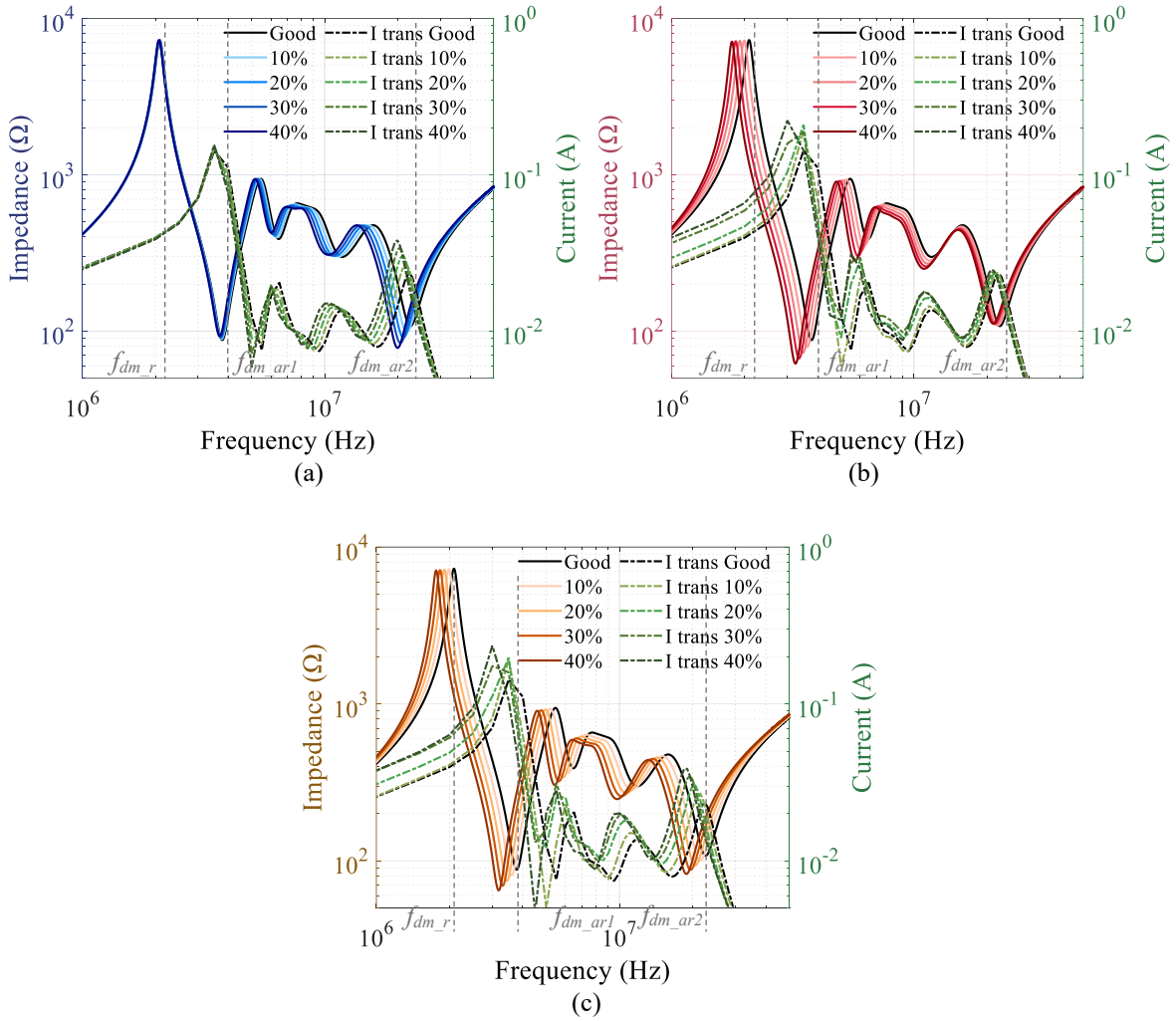

Fig. 3-12 DM impedance and FFT spectrum of i_{trans} for degradation scenarios (a) TT degradation (b) GW degradation (c) Overall (TT and GW) degradation.

3.4 Summary

In this chapter, comprehensive investigations on the influence of various degradations including turn-to-turn (TT) degradation, ground wall (GW) degradation on the line current (i_t), transient line current (i_{trans}) and the common mode (CM) impedance spectrum have been presented. The transient line current (i_{trans}) show unique behavior, which contains high-frequency (HF)

oscillations in the beginning followed by subsequent low-frequency (LF) oscillation, these oscillations are directly linked with the antiresonance frequencies of the CM/DM impedance. Further investigations reveal how different levels of insulation degradation affect impedance, which gets distinctly reflected in the i_t and i_{trans}. Specifically, the i_{trans} and the prominent oscillations at antiresonance frequencies can be utilized the extract information on CM impedance. This chapter emphasizes on the potential utilization of the HF line current oscillations for monitoring insulation condition.

Chapter 4:A Novel Methodology for Simultaneous Condition Monitoring of TT and GW Insulation

4.1 Introduction

A novel condition monitoring methodology for TT and GW insulation is presented. This method proposes indicators that have the capability to determine the SOH of insulation and classify between TT and GW insulation degradations. The proposed method employs wavelet packet decomposition (WPD) to analyze high frequency (HF) line current and extract indicators for monitoring the state of health (SOH). Compared with existing methods, the proposed technique can provide the SOH indicators of turn-to-turn (TT) and groundwall (GW) insulation simultaneously through the analysis of HF line current. Moreover, antiresonance oscillations in the HF line current are also explored to determine insulation SOH. The results on validation of the proposed methodology through simulation as well as experiments have been presented. In this chapter, firstly, the proposed methodology is presented. Thereafter, validation of the proposed methodology through simulation studies has been discussed. Thereafter, the experimental setup and investigations of the proposed methodology through experiments have been presented.

4.2 Overview of the Proposed Methodology

The proposed methodology relies on the fact that the degradation of insulation leads to a change in the capacitance of the insulation, resulting in a change in the high-frequency (HF) impedance of the winding. The previous section presented the prominent oscillations in the HF transient current i_{trans}, which reflects the CM impedance at anti-resonance frequencies. Additionally, analysis of the influence of various insulation degradation on i_{trans} confirms its viability in assessing insulation condition. Utilizing such distinctive behavioral characteristics of i_{trans}, a novel method to determine SOH of TT and GW insulation is proposed that only requires line current measurement. The framework for the proposed methodology is illustrated in Fig. 4-1, it mainly contains 4 steps: 1) Extraction of HF transient current i_{trans} 2) Wavelet Packet Decomposition 3) Calculation of SOH Indicators Through Wavelet Packets Reconstruction.

4.2.1.Step 1: Extraction of HF Transient Current i_{trans}

As presented in the previous section, to extract i_{trans}, a PWM voltage excitation pulse V_{PWM} is applied to the winding and the HF line current i_t is obtained. Here, i_t is the line current that rises at a steady rate due to the winding's inductance L_M, and it is super positioned with of HF transient current i_{trans}, and it can be represented by equation (4.1).

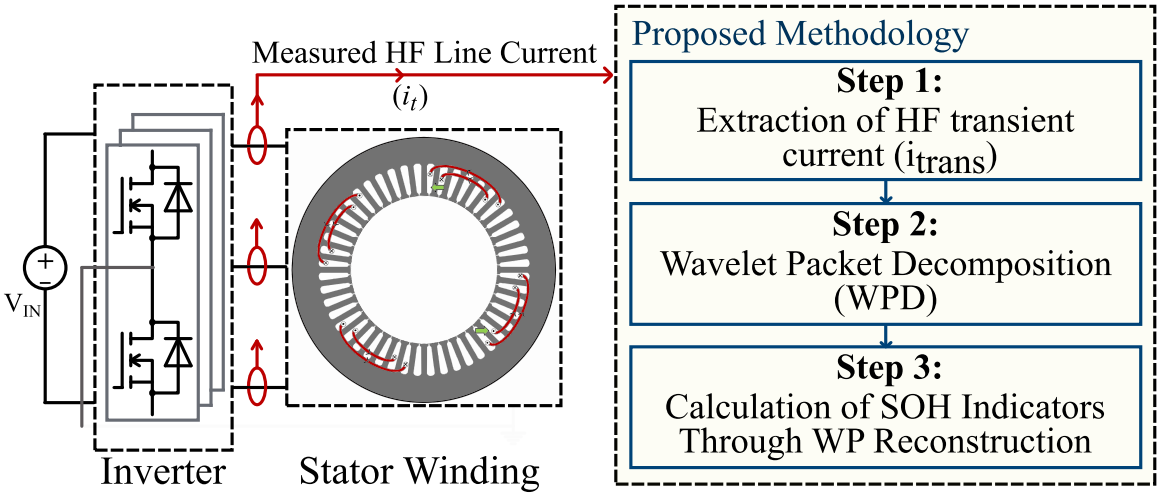

Fig. 4-1 Illustration of proposed WPD based methodology

$$i_{line}(t) = i_{trans}(t) + \frac{1}{L_M}\int_0^t V_{PWM}(t)\,dt \tag{4.1}$$

Here, it is crucial to note that the oscillations in the i_{trans} exists for certain microseconds. Therefore, i_{line} can be acquired for such short duration. Assuming the signal i_{line} is acquired for n samples, the resultant data is $[i_{t1}, i_{t2} \ldots, i_{tn}]$. Thereafter polynomial curve fitting is performed to the data. The fitting is articulated through the general polynomial as equation (4.2). However, considering the nature of the line current i_t, where current saturation occurs only after a certain period, a first-order polynomial is sufficient to capture this linear trend. First order polynomial fitting can be given by equation (4.3).

$$f(t) = p_k t^k + p_{k-1} t^{k-1} + \ldots + p_1 t + p_0 \tag{4.2}$$

$$f(t) = p_1 t + p_0 \tag{4.3}$$

Once the coefficients p_0 and p_1 are obtained, the transient current i_{trans} can be obtained as the equation (4.4).

$$i_{trans}(t) = i_{line}(t) - p_1 t - p_0 \tag{4.4}$$

This allows for the precise separation of i_{trans} from the acquired line current signal i_{line}. Thereafter i_{trans} is further processed using WPD.

4.2.2.Step 2: Wavelet Packet Decomposition

As discussed before, the proposed methodology utilizes WPD to extract important features from the transient current i_{trans}. The WPD is illustrated in Fig. 4-2, it decomposed the signal into approximation and detail coefficient using low-pass filter $h(n)$ and high-pass filter $g(n)$ respectively. The resultant coefficients at level l can be given by equation (4.5) and (4.6).

$$w_{l,2k}(t) = \sum_{n} h(n)\, w_{l-1,k}(2t - n) \tag{4.5}$$

$$w_{l,2k+1}(t) = \sum_{n} g(n)\, w_{l-1,k}(2t - n) \tag{4.6}$$

Here, $w_{l,2k}$ denotes approximation coefficient at level l, obtained by convolving the k^{th} coefficient from the previous level $l-1$, denoted by $w_{l-1,k}$, with a low pass filter $h(n)$. Similarly, convolution of a high pass filter $g(n)$ over the same coefficient $w_{l-1,k}$ provides detail coefficient $w_{l,2k+1}$. The length of these coefficient vector at level l can be given by $n \approx N/2^l$. As shown in Fig. 4-2, this convolution procedure is repeated multiple times to obtain coefficients at different levels. Due to the filtering, each coefficient at level l and position k in the decomposition tree is associated with a particular frequency band $[f_{min}, f_{max}]$, given using equation (4.7).

$$f_{min} = \frac{k}{2^{l+1}} f_s \;,\; f_{max} = \frac{k+1}{2^{l+1}} f_s \tag{4.7}$$

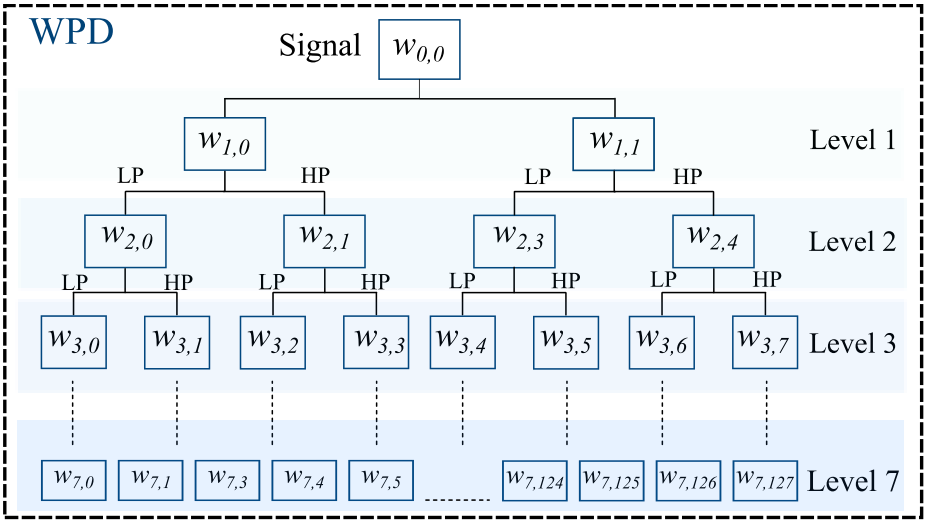

Fig. 4-2 Illustration of extraction of wavelet packets through WPD

Where f_s represents the sampling frequency. This property of WPD facilitates a detailed frequency analysis. Hence, this method utilizes WPD to extract crucial information for condition monitoring. When employing WPD, there are two crucial factors that require proper consideration. The first is the selection of the appropriate base wavelet function and the other is selecting the appropriate level of decomposition. Given the focus of the proposed methodology in identifying deviations near antiresonance frequencies, the selection of level of decomposition should be done in such a way that the antiresonance frequencies f_{CM_ar1} and f_{CM_ar2} are isolated within separate coefficients, which can be satisfied with the condition in equation (4.8) and (4.9).

$$\frac{k_1}{2^{l+1}} f < f_{CM\_ar1} < \frac{k_1}{2^{l+1}} f \tag{4.8}$$

$$\frac{k_2}{2^{l+1}} f < f_{CM\_ar2} < \frac{k_2}{2^{l+1}} f \tag{4.9}$$

Here, $k1 \neq k2$ to ensure f_{CM_ar1} and f_{CM_ar2} are isolated within separate wavelet coefficients. This allows the isolation of specific frequency bands that show a strong correlation with degradation severity or degradation type. Moreover, the resolution of each frequency band $\Delta f(l) = f_{max}(l,k) - f_{min}(l,k)$ should be maintained as high as possible to capture detailed behavior around f_{CM_ar1} and f_{CM_ar2}. Broad frequency bands may encompass frequency components unrelated to the deviations near to the antiresonance frequencies, leading to potential misinterpretation of the relevant features. However, achieving a higher resolution requires higher level of decomposition, which results in increased computational cost. Therefore, the level of decomposition should be optimized to balance resolution of frequency band and computational cost.

For the selection of appropriate base wavelet, three predominant approaches are predominant:1) Maximum energy criterion, 2) Minimum Shannon entropy criterion, and 3) Energy to Shannon entropy ratio (ESER) based criterion. The underlying concept of ESER based criterion is to maximize the ratio of energy to Shannon entropy for given base wavelet. Building upon the foundational principle of the ESER, this method utilizes modified approach that maximizes the sum of normalized ESER values from two distinct coefficient. The base wavelet is selected in such way that the sum of normalized ratio from both the packets is maximized. For a set of base wavelet candidates $\Psi = [\psi_1, \psi_2, \dots, \psi_m]$, the procedure for selection of optimal base wavelet ψ_{opt} can be done using the following steps.

Step 2A: Firstly, for each candidate ψ_w in Ψ, wavelet packet coefficients for the packet of interest WP_j, where j is either 1 or 2 associated with the antiresonance frequencies. Thereafter, for each of these packets, energy, entropy and ESE ratio is computed using equations (4.10)-(4.12).

$$E_{WP_j}(\psi_w) = \sum_{i}^{y} \left| w_{WP_j,i}(\psi_w) \right|^2 \tag{4.10}$$

$$H_{WP_j}(\psi_w) = -\sum_{i}^{y} \frac{\left| w_{WP_j,i}(\psi_w) \right|^2}{E_{WP_j}(\psi_w)} \log\left(\frac{\left| w_{WP_j,i}(\psi_w) \right|^2}{E_{WP_j}(\psi_w)} \right) \tag{4.11}$$

$$ESER_{WP_j}(\psi_w) = \frac{E_{WP_j}(\psi_w)}{H_{WP_j}(\psi_w)} \tag{4.12}$$

Here, y denotes the number of elements within the coefficient vector that are of interest for analysis. For WP_1, which captures low frequency (f_{CM_ar1}) component that exists throughout the duration of signal, y is set to its maximum permissible value. While WP_2 captures high frequency (f_{CM_ar2}) componenet that exists fraction of the original signal hence it is kept small. Approximately the value of y can be obtained as $y \approx N_{hf}/2^l$, where N_{hf} is the number of samples related to initial high frequency oscillations in i_{trans}, and l is level of decomposition.

Step 2B: This step involves performing normalization for each set of ESER values corresponding to WP_j of interest. This step is crucial to ensure the homogeneity of data resulting from ESER ratios from different packets. By normalizing the data, consistent and accurate comparison of ESER can be guaranteed. The normalized ESER ($ESER_{WP_j}^{norm}$) can be obtained from the equation (4.13).

$$ESER_{WP_j}^{norm}(\psi_w) = \frac{ESER_{WP_j}(\psi_w) - \min\left\{ESER_{WP_j}\right\}}{\max\left\{ESER_{WP_j}\right\} - \min\left\{ESER_{WP_j}\right\}} \tag{4.13}$$

Here, $\min\{ESER_{WP_j}\}$ and $\max\{ESER_{WP_j}\}$ represent min and maximum ESER value within the set for packet WP_j. This step results in set of normalized ESER values for each packet WP_j for all wavelet candidates.

Step 2C: The optimal wavelet ψ_{opt} is determined by identifying the wavelet that maximizes the sum of normalized ESER as shown in equation (4.14).

$$\psi_{opt} = \underset{\psi_w \in \Psi}{argmax} \left(ESER_{WP_j}^{norm}(\psi_w) + ESER_{WP_j}^{norm}(\psi_w) \right) \quad (4.14)$$

The chosen wavelet ψ_{opt} is anticipated to offer the optimal balance between energy and entropy for the wavelet packets associated with the antiresonance frequencies, thus enabling insightful analysis.

After identifying the appropriate wavelet packets related to the antiresonance frequencies (WP_1 and WP_2), optimal base wavelet ψ_{opt}, and optimal decomposition level l, they become the standard for processing the signal i_{trans} to obtain wavelet packets that can be further utilized for SOH determination and degradation classification.

4.2.3.Step 3: Calculation of SOH Indicators Through Wavelet Packets Reconstruction

Step 3A: This step involves the calculation of indicators from packets obtained from WPD. These indicators can be tracked throughout the life of a machine and informed decisions on insulation SOH can be made. The first step involves reconstruction of the signal from the packets WP_1 and WP_2.Through this reconstruction procedure, the signal related to a specific frequency band or wavelet packet can be obtained, the procedure is given by the equation (4.15).

$$w_{l,k}(t) = \sum_n \left(h^*(t-2n)\, w_{l+1,2k}(t) + g^*(t-2n)\, w_{l+1,2k+1}(t) \right) \quad (4.15)$$

Here, $w_{l,k}$ denotes k^{th} coefficient at level l, obtained from the coefficients $w_{l+1,k}$ and $w_{l+1,2k+1}$ from the next level $l+1$. Here $h^*(n)$ and $g^*(n)$ represent the reconstruction low pass and high pass filters. Through reconstruction process, signal $i_{WP1,n}$ and $i_{WP2,n}$ related to WP_1 and WP_2 are obtained. Signal $i_{WP1,n}$ represents behavior related to the first antiresonance frequency and $i_{WP2,n}$ represents the behavior related to the second antiresonance frequency. These signals are further processed to compute the indicators, given by equations (4.16)-(4.17). These indicators represent the norm of the signal up to p samples.

$$SOH_{GW} = \sqrt{\sum_{i=1}^{p} |i_{WP1,n}|^2} \quad (4.16)$$

$$SOH_{TT} = \sqrt{\sum_{i=1}^{p} |i_{WP2,n}|^2} \quad (4.17)$$

Here, the value of p represent the samples of interest in the reconstructed signal. For SOH_{TT}, initial high frequency oscillations in i_{trans} are of interest hence the value of p is the number of samples associated with these high frequency oscillations. Similarly, for SOH_{GW}, the value of p can be selected to be maximum as the full signal is of relevance. These indicators can be utilized for SOH determination as well as classifying between TT and GW degradations.

Step 3B: The procedure for simultaneous monitoring of GW and TT degradation is described in Fig. 4-3.As discussed, the GW degradation causes deviations in both HF and LF oscillations at f_{CM_ar1} and f_{CM_ar2}. Therefore, GW degradation has influence on both SOH_{GW} and SOH_{TT}. While the presence of only TT degradation does not affect oscillations at f_{CM_ar1}, and causes deviations in only SOH_{TT}. Hence, firstly, SOH_{GW} should be determined. The deviations in

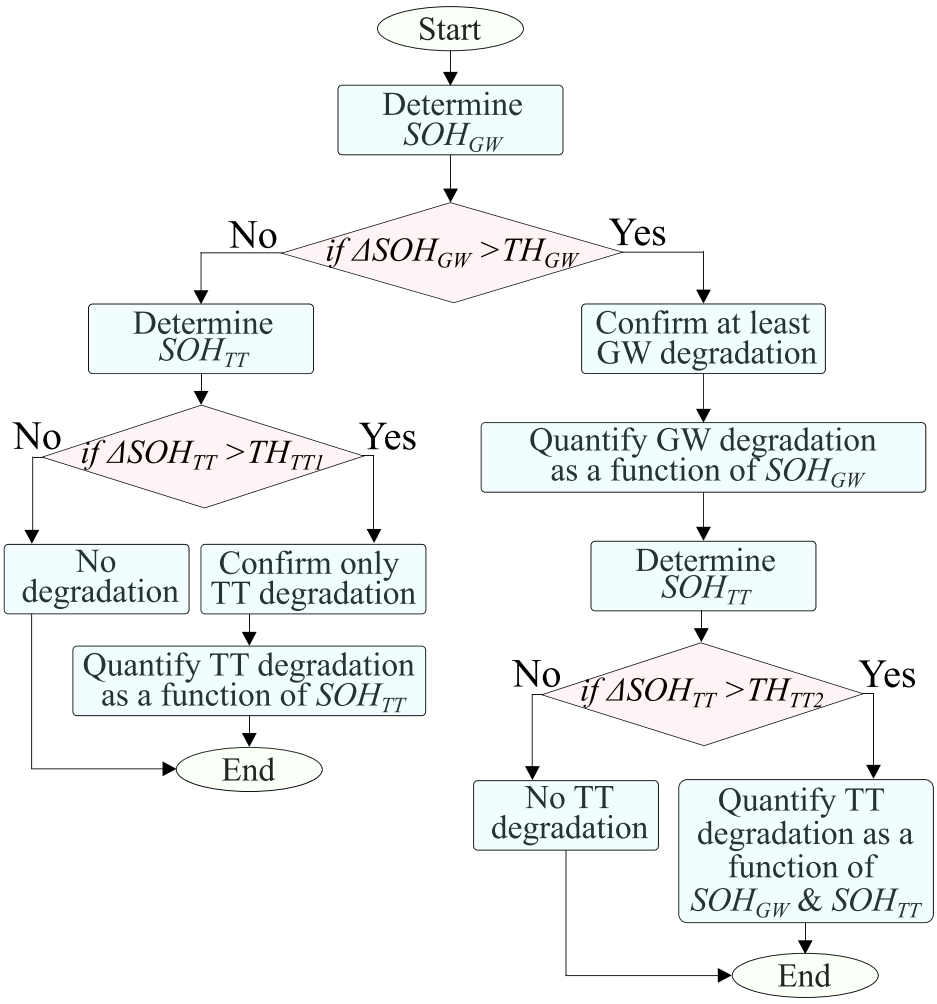

Fig. 4-3 Procedure for condition monitoring

SOH_{GW} greater than threshold TH_{GW} confirms the presence of GW degradation. The severity of GW degradation can then be quantified based on the deviations in SOH_{GW}. Following the identifying of the GW degradation, the indicator SOH_{TT} is determined and utilized to determine if TT degradation exists using the threshold TH_{TT2}. Thereafter, if TT degradation is present, its severity is determined based on the value of SOH_{GW} and SOH_{TT}. Here, it is crucial to note that the GW degradation always causes deviations in SOH_{TT}. Therefore, in scenarios where both GW and TT degradations are present, the SOH_{TT} differs in the scenario when only TT degradation occurs. The value of SOH_{TT} is typically higher in such cases hence appropriate thresholds are required to be established. If the value of SOH_{GW} does not increase, it indicates the absence of GW degradation. In such cases, SOH_{TT} is determined. An increase in SOH_{TT} beyond threshold TH_{TT2} confirms the presence of only TT degradation. Thereafter the severity of TT degradation can then be quantified based on the deviations in SOH_{TT}. Conversely, no increase in SOH_{TT} confirms no insulation degradation or good insulation scenario. Using the information on SOH indicators and their relationship with degradations, appropriate thresholds can be established and utilized for condition monitoring.

4.3 Simulation Results: Validation of the Proposed Methodology

This section demonstrates the efficacy of the proposed methodology through simulation studies. A comprehensive simulation study have been conducted for various degradation scenarios and details on resulting indicators from the proposed method has been presented, this analysis highlights the method's robustness in accurately identifying and classifying insulation degradation. As discussed in Chapter 3, the HF winding model is utilized to simulate various insulation condition scenarios, including 1) good insulation 2) TT insulation degradation 3) GW insulation degradation 4) Overall degradation where both TT and GW insulation degrades. The degradation severity has been varied from 10% to 40% for each scenario and corresponding line currents i_t have been obtained. The currents i_t and i_{trans} are illustrated in Fig. 4-4. Here, i_t and i_{trans} are sampled at the sampling period of 1.2 ns., resulting in sampling frequency f_s of 833 MHz. Thereafter, these currents have been further processed using the proposed methodology to obtain various indicator.

Firstly, using the good insulation scenario, the baseline indicator has to be established. Line current i_t is processed to extact i_{trans}. The next step involves selection of appropriate wavelet packets related to the antiresonance frequencies. As discussed in Chapter 3, the first and second antiresonance frequencies are approximately 1.91 MHz and 23 MHz, respectively. Based on equations (4.7)-(4.9), wavelet packets $w_{7,0}$ and $w_{7,7}$ are selected for analysis. These packets corresponds to frequency bands [0, 3.25] MHz and [19.5, 22.8] MHz respectively, which sufficiently include antiresonance frequencies. For the selection of the appropriate base wavelet function ψ_{opt}, 93 candidate base wavelets from various wavelet families such as Haar, Daubechies, Symlets, Biorthogonals, Coiflets, etc. have been selected. Through the procedure described in the previous subsection, the candidate wavelet has been selected. Out of 93 wavelets mentioned before, 'db19' is selected to be the base wavelet with a ratio of 1.3. Following the determination of appropriate wavelet packets and base wavelet, the reconstruction of wavelet packets is performed. Then reconstructed signals are processed to determine the indicators SOH_{GW} and SOH_{TT}. Similarly, Similarly, for the remained degradation scenarios, the HF transient current i_{trans} is processed to obtain the indicators using the same wavelet packets and base wavelet. These indicators are shown in Fig. 4-5 and Table 4.3. The proposed SOH indicators are highly effective at detecting insulation degradations. The indicator SOH_{GW} is designed to assess degradation in GW insulation. As seen from Fig. 4-5 (a), SOH_{GW} shows an increase as the GW insulation degrades, while remains stable in the case of TT insulation degradation. Notably, it

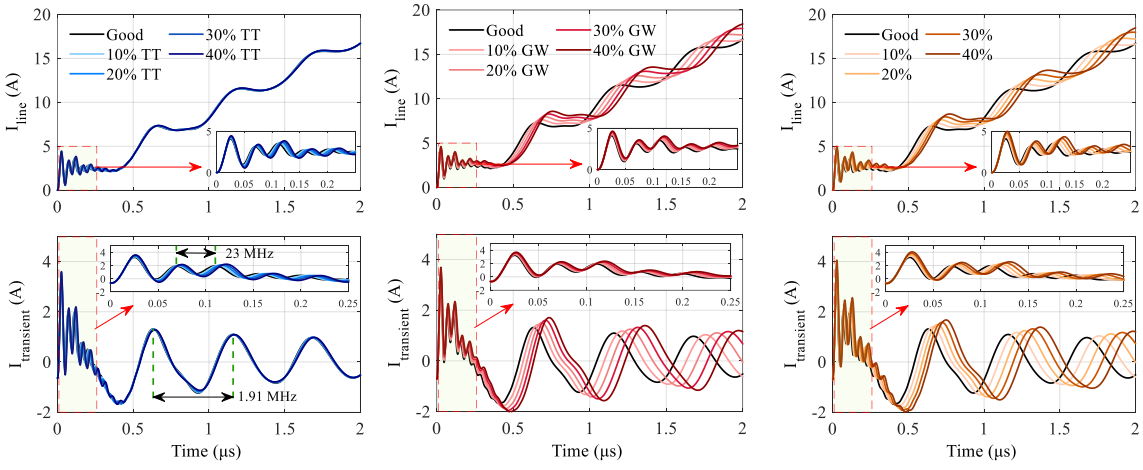

Fig. 4-4 Current i_t and i_{trans} for various degradation scenarios. (a) TT degradation (b) GW degradation (c) Overall (TT and GW) degradation

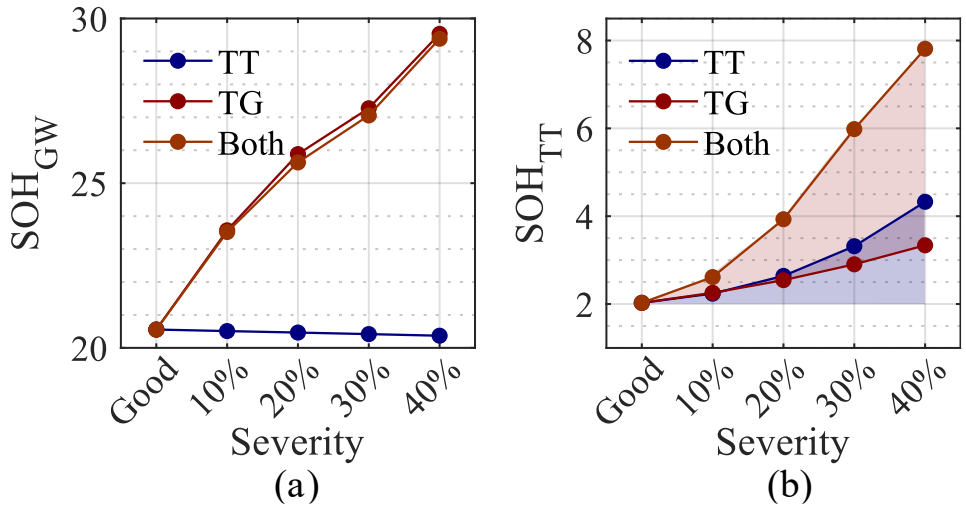

Fig. 4-5. SOH indicators (a) SOH_{GW} (b) SOH_{TT}

Table 4-1 Simulation Results: Indicators for various degradations

Degradation Scenario	**Severity**	SOH_{GW}	SOH_{TT}	**% Change in SOH_{GW}**	**% Change in SOH_{TT}**
Good	0 %	20.56	2.03	-	-
TT Degradation	10%	20.51	2.24	-0.24	10.34
	20%	20.46	2.64	-0.49	30.05
	30%	20.42	3.32	-0.68	63.55
	40%	20.37	4.33	-0.92	113.30
GW Degradation	10%	23.57	2.25	14.64	10.84
	20%	25.88	2.54	25.88	25.12
	30%	27.27	2.90	32.64	42.86
	40%	29.53	3.34	43.63	64.53
Overall (TT and GW) Degradation	10%	23.52	2.61	14.40	28.57
	20%	25.63	3.93	24.66	93.60
	30%	27.06	5.98	31.61	194.58
	40%	29.39	7.81	42.95	284.73

shows greater change for more severe degradation and remain unchanged for TT degradation, reinforcing its reliability as an indicator for GW degradation. Indicator SOH_{TT} is designed for TT degradation detection. As shown in Fig. 4-5 (b), the value of the indicator shows an increase as the TT degradation severity increases. However, the value of the indicator also increases due to the GW degradation scenarios. As discussed in Section II, this is expected due to the fact that the GW degradation also affects the frequency spectrum near to the second antiresonance frequency. However, the indicator is less sensitive to the GW degradation and shows lesser change than in

the case of TT degradation scenario, thereby minimizing the risk of false alarm. Thus, high accuracy can be ensured for TT degradation scenarios. For the most challenging scenario when both TT and GW degradations are present, the proposed indicators are effective as the SOH_{GW} can provide information on the GW insulation. While the SOH_{TT} can be utilized for SOH determination for TT insulation. Using the information on SOH indicators and their relationship with the degradation patterns, precise thresholds can be established. This enables accurate online condition monitoring; these indicators can be tracked over time for insulation SOH determination. Using the information on SOH indicators and their relation with the degradation patterns, precise thresholds can be established. The challenge to establish the relationship between varying degradation types, severities, and the resultant indicators can be addressed through either simulation or hardware based approach. For instance, the machine can be subjected to thermal cycle based aging to obtain a relation between the WPD indicators and the level of degradation or the number of thermal cycles. Once this relation is established, monitoring WPD indicators throughout the machine's operational lifecycle becomes a viable strategy for assessing insulation degradation. Alternatively, a simulation-based approach can be employed, where a high-fidelity model of machine's stator winding, cable can be utilized to simulate various insulation degradation scenarios, thus establishing a link between WPD indicators and insulation degradations without subjecting the machine to actual aging or even without having a physical machine. However, it is important to note the focus of this research is not to propose such an accurate model, but rather to utilize the existing models for investigations on insulation condition monitoring. Moreover, it's crucial to emphasize that the primary focus of this research is not on establishing these relationships but rather on exploring insulation condition monitoring using novel indicators.

4.4 Experimental Results: Validation of the proposed methodology

4.4.1. Experimental Setup

This section explains the laboratory setup utilized for investigations on the proposed methodology. As shown in Fig. 4-6, the setup contains a DC power supply, a SiC MOSFET based inverter, a stator winding, emulation PCBs, connection cables and devices for signal measurement. The degradation of insulation is an irreversible process, and it is not feasible to investigate various types of degradation with varying severity of degradation because of the complexities associated with controlling the desired amount of degradation in specific insulation

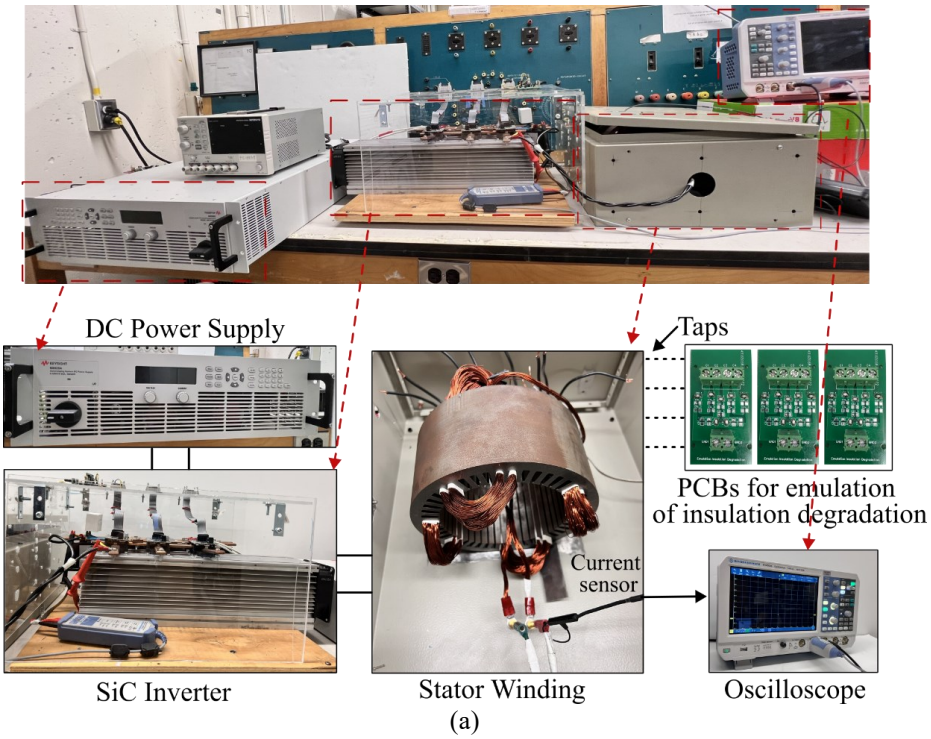

(a)

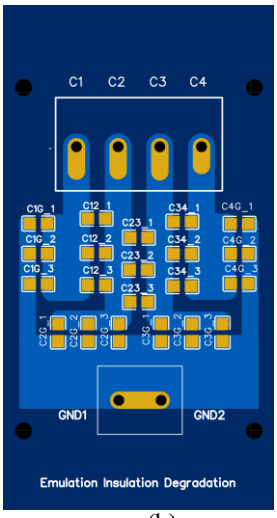

(b)

Fig.4-6 (a) Experimental setup (b) PCBs utilized for emulation of insulation degradation

in the winding. For instance, TT degradation can not be performed without having an effect on the GW insulation. Due to such challenges, various literature adopts emulation of insulation degradation. This offers the advantages such as great control over both the amount of degradation and type of degradation. In such emulation, capacitors are connected to the winding to replicate the insulation degradation. To emulate TT degradation, a capacitor can be connected in parallel to the winding, while GW degradation can be emulated by connecting a capacitor

between winding to the ground. Hence, a custom stator winding with taps has been utilized which allows emulation of insulation degradations, eight taps have been created. Deliberate efforts were made to minimize the length of the taping and reduce additional parasitic, although complete elimination is not possible due to practical constraints. Moreover, custom PCBs have been developed for efficient emulation of both TT and GW degradations. Ceramic capacitors with different values were connected to custom PCBs to emulate various severities of degradation. For various emulation scenarios, line currents i_t are measured using Keysight 30MHz/300A HF Rogowski current probe and R&S RTM3004 500MHz oscilloscope. The measured data contain noise which has been filtered using a low-pass filter with the cutoff frequency of 50MHz.

4.4.2. Test Results and Discussions

Using the experimental setup, the proposed methodology has been investigated. Firstly, for the good insulation scenario, the proposed framework has been followed to obtain the baseline indicators. Using the SiC inverter, a voltage pulse is applied to obtain i_t has been measured and corresponding i_{trans} is calculated, both currents are shown in Fig. 4-7. Here, the sampling period is set to 0.8 ns., resulting in a sampling frequency f_s of 1250 MHz.

As discussed previously, the prominent oscillations of i_{trans} represents the antiresonance

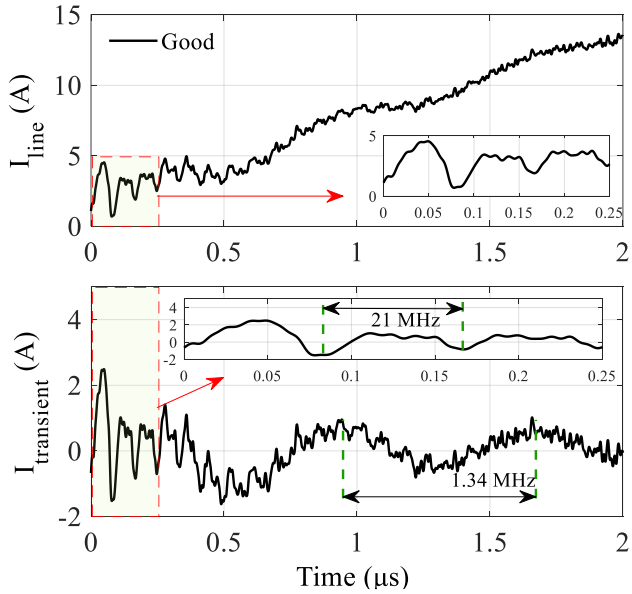

Fig. 4-7 Experimental results: Dominant oscillations in i_t and i_{trans}

frequencies in the CM impedance. The dominant oscillations can be observed at 21MHz and 1.34 MHz. Here, it is crucial to note that these antiresonance frequencies have been deviated from 30MHz and 1.89MHz. This reduction in antiresonance frequencies is expected due to additional inductances in the loop due to connection cables and inverter busbars. The proposed methodology relies on the resultant i_{trans} of the system. Hence for hardware experimentation, the antiresonance frequencies to be considered are 21MHz and 1.34MHz. Now, relevant wavelet packets are selected using equations (11)-(12). Wavelet packets $w_{7,0}$ and $w_{7,2}$ are selected for analysis. These packets coreresponds to frequency bands [0, 4.88] MHz and [9.76, 14.64] MHz respectively. Optimal base wavelet function ψ_{opt} has been selected from 93 candidate base wavelets. The candidate wavelet that maximizes the sum of ESER values for WP_1 and WP_2 is chosen as the optimal wavelet. Out of 93 wavelets mentioned before, 'sym16' is selected to be the base wavelet with a ratio of 1.47. Following the determination of appropriate wavelet packets and base wavelet, the reconstruction is performed. The reconstructed signals are further processed to determine the indicator values. These values work as reference values and for various degradation scenarios, they are expected to show an increase. The emulated degradation scenarios include GW degradation, TT degradation and degradation in both TT and GW insulation. For each of the aforementioned scenarios, two severities 10% and 20% have been emulated. For good insulation degradation scenarios, the total GW insulation measured is about 1.15 nF. Therefore, for 10% GW severity, an additional capacitance of 20 pF has been inserted between the coil and the ground using the taps. Similarly, for 20% GW severity, additional capacitance of 40 pF has been connected. For TT degradation scenario, the initial capacitance measured is 109 pF. Hence, across each coil approximately 10pF and 20 pF capacitors have been connected which represents increase in the TT insulation approximately by 10% and 20%. For the scenario where both insulations are degraded, capacitors representing both TT and GW degradations have been inserted. For each degradation scenario, the indicators have been obtained as described in the procedure. Obtained currents i_t and i_{trans} for various degradation scenarios can be seen in Fig. 4-8. The resultant indicators can be seen in the Table 4.4.

From Fig. 4-8, the deviations in the transient current due to degradations can be observed. The deviation in the transient currents is not very obvious compared to the simulation, this is due to the noise in the measurements. However, the LF oscillations at f_{CM_ar1} show visible deviation while the deviations in HF oscillations at f_{CM_ar2} are not significant. Despite these challenges, the

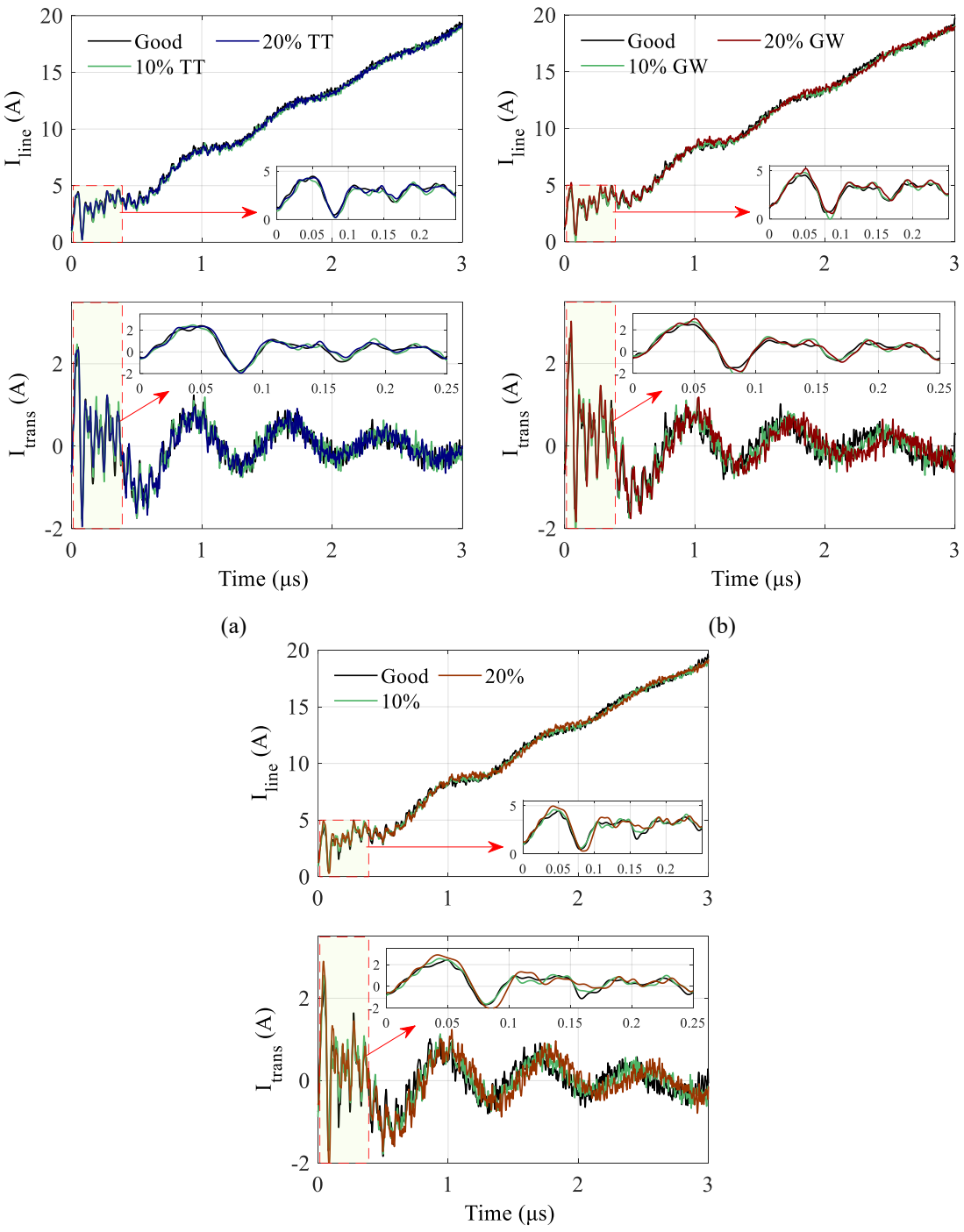

Fig. 4-8 Current i_t and i_{trans} for various degradation scenarios. (a) TT degradation (b) GW degradation (c) Overall (TT and GW) degradation

proposed method performs quite well. The indicators show similar trends to the simulation results. For good insulation scenario, the value of SOH_{GW} is 2.03 while the value of SOH_{TT} is

25.14. For TT degradation scenario, the value of SOH_{TT} increases with increasing level degradation severity, while SOH_{GW} remains constant. For GW degradation scenario, the value of both the indicators increases. The indicator SOH_{TT} show lesser change than in the TT degradation scenario while the indicator SOH_{GW} show major deviation as the degradation severity increases, the finding matches the simulation results. For the scenario of both the degradation, the indicators further confirm the trend, SOH_{TT} and SOH_{GW} both increase with degradation severity.

Table 4-2 Experimental Results: Indicator for Various Degradations

Degradation Scenario	**Severity**	$\boldsymbol{SOH_{GW}}$	$\boldsymbol{SOH_{TT}}$	**% Change in $\boldsymbol{SOH_{GW}}$**	**% Change in $\boldsymbol{SOH_{TT}}$**
Good	0 %	25.14	2.03	-	-
TT Degradation	10%	24.62	2.18	-2.07	7.39
	20%	25.20	2.89	0.24	42.36
GW Degradation	10%	26.69	2.50	6.17	23.15
	20%	26.95	2.73	7.20	34.48
Both TT and GW Degradation	10%	26.70	2.10	6.21	3.45
	20%	28.69	3.03	14.12	49.26

The consistency between the experimental results and simulation results highlights the ability of the proposed method and indicator's capabilities in condition monitoring. However, there still some discrepancies between the hardware and simulations. These discrepancies are due to the fact the emulation of insulation degradation does not represent the same scenario of actual degradation with great accuracy. The additional connections to the winding through taps, introduce additional parasitic and new connections that are not present in the actual degradation. Previously various literature reported some limitations of emulation of insulation degradations. Despite these limitations, emulation remains the most viable method for the investigation and validation of condition monitoring methodologies. It provides a repeatable, controlled environment to investigate insulation condition monitoring techniques, which is indispensable in the absence of extensive real degradation data. Hence, while the experimental setup presents an emulation of degradation rather than actual degradation, the observed trends indicators prove the efficacy of the proposed method's effectiveness. Moreover, the simulation results discussed before, where in the degradation is closer to the actual degradation, provides confidence in the proposed methodology and indicators as reliable approach for condition monitoring.

4.5 Summary

A novel insulation condition monitoring method is proposed that utilizes antiresonance oscillation in HF line currents to determine the overall SOH of TT and GW insulation. The proposed method utilizes wavelet packet decomposition (WPD) to extract crucial indicators for insulation SOH determination. The detailed steps for the utilization of the proposed approach have been discussed in this chapter. Simulation and experimental investigations have been conducted for the validation of the proposed methodology. Simulation based investigations have been conducted using HF winding model, where in different types and severity of degradations have been simulated. This includes multiple degradation scenarios with varying degradations severities, including good insulation, GW insulation degradation, TT insulation degradation and overall degradation where both TT and GW insulation degrades. Experimental tests have been performed on a laboratory setup, where in multiple degradations have been emulated and results have been discussed. The preliminary results are promising.

Chapter 5: A Novel Noise-Adaptive Insulation Condition Monitoring Methodology

This chapter propose a methodology that utilizes a machine learning (ML) algorithm to quantify the insulation degradation by utilizing the features obtained by processing high-frequency (HF) line current. To extract features from the HF line current, wavelet scattering transform (WST) is utilized. The proposed condition monitoring framework has a unique capability to quantify insulation degradations even with varied levels of measurement noise. Within this chapter, firstly, an overview of the proposed methodology is provided. Thereafter, a comprehensive framework for the ML-based insulation condition monitoring, which addresses data acquisition, data augmentation, feature extraction as well as training and testing various ML algorithms, is introduced. Thereafter, the efficacy of the proposed approach is validated with extensive simulation and experimental tests, and the performance in detecting insulation degradation is confirmed by various results under different measurement noises.

5.1 Overview of the Proposed Methodology

The proposed methodology utilizes the fact that the capacitance of the insulation changes due to degradation, which results in variation in the high-frequency (HF) impedance of the winding. This variation can be detected by identifying deviations in the HF line current. This chapter proposes a methodology to extract and utilize features from this HF line current to quantify degradation. The key steps of the proposed methodology are illustrated in Fig. 5-1.

Step 1: Extraction of HF Transient Current (i_{trans})

To extract information on degradation, a typical PWM voltage pulse from the inverter is applied to the winding and the HF line current (i_{line}) is measured. The excitation is a typical inverter voltage pulse which can be considered as HF excitation to the winding, with excitation frequency that extends up the frequency of $f_{max} = 1/\min(t_r, t_f)$. Here, t_r is rise time and t_f is fall time of the PWM pulse. Due to such HF excitation, the resultant i_{line} contains HF components which are a function of HF impedance of the winding, this current can be represented by equation (5.1)

$$i_{line}(t) = i_{trans}(t) + \frac{1}{L_M}\int_0^t V_{PWM}(t)\,dt \tag{5.1}$$

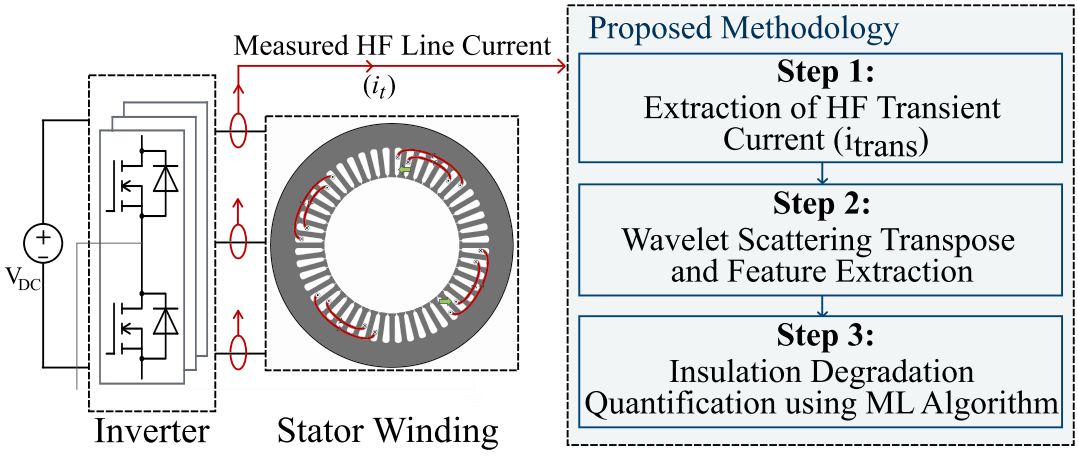

Fig. 5-1 Overview of the key steps involved

Here, i_{line} rises at a steady rate due to the winding's inductance L_M, V_{PWM} is a voltage excitation pulse, and i_{trans} represents the HF transient current which mainly represents current through the high-frequency coupling paths. The HF impedance of the winding change is due to capacitance increase caused by insulation degradation, the capacitance increases can be up to 40-50%. These changes in impedance cause variation in current i_{trans}. Hence, the proposed approach utilizes the current i_{trans}, to identify the changes in winding's HF impedance. The current i_{line} is acquired for only a few microseconds due to short duration of HF oscillations. This current is further processed to mitigation of the steady increase in i_{line}. A first-order polynomial is sufficient to capture this linear trend, this is represented by equation (5.2). After determination of coefficients p_0 and p_1, i_{trans} can be obtained using equation (5.3).

$$f(t) = p_1 t + p_0 \tag{5.2}$$

$$i_{trans}(t) = i_{line}(t) - p_1 t - p_0 \tag{5.3}$$

Extracted i_{trans} is further processed using wavelet scattering transform (WST) to extract crucial features. These features are further processed and utilized for quantification of insulation condition.

Step 2: Wavelet Scattering Transform and Feature Extraction

As discussed, the proposed methodology utilizes wavelet scattering transform (WST) to extract crucial features from the transient current i_{trans}. The WST is a powerful feature extraction method that decomposes signal through multilevel hierarchical structure using wavelet filters,

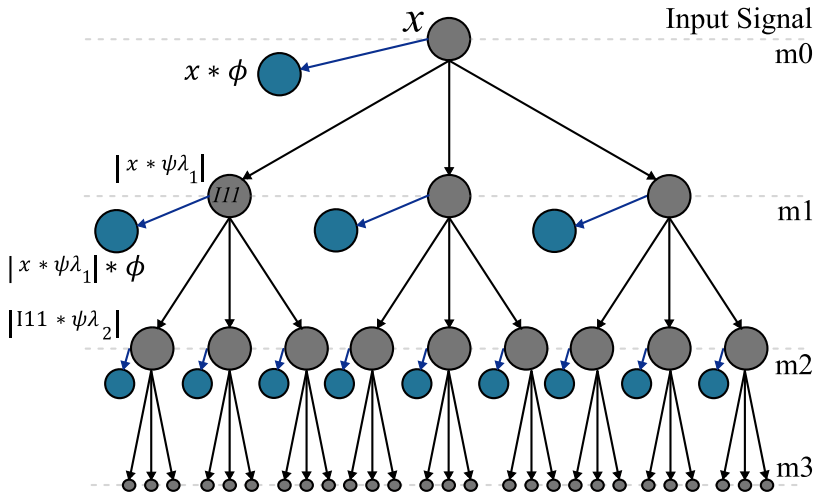

Fig. 5-2 Illustration of extraction of scattering coefficients through WST

modulus operation and low pass filter [23]. The features extracted through this process are referred to as scattering coefficients, Fig. 5-2 illustrates the multilevel structure and extraction of scattering parameters, where the blue nodes represent the scattering parameters.

Considering the time-domain signal $x(t)$, the zero-order scattering coefficient S_0x can be obtained using equation (5.4) by applying low pass filter that performs averaging. While the first order coefficients and second order coefficients can be obtained using equation (5.5) and equation (5.6) respectively.

$$S_0x(t) = x * \phi(t) \tag{5.4}$$

$$S_1x(t,\lambda_1) = |x * \psi_{\lambda_1}| * \phi(t) \tag{5.5}$$

$$S_2x(t,\lambda_1,\lambda_2) = ||x * \psi_{\lambda_1}| * \psi_{\lambda_2}| * \phi(t) \tag{5.6}$$

Here, $\phi(t)$ represents a low pass filter, ψ_{λ_1} and ψ_{λ_2}represents the wavelet filter banks for the first and second order transform respectively. These filter banks typically use Morlet wavelet $\psi(t)$ as mother wavelet, while $*$ represent the convolution operation. To obtain the first order scattering coefficients S_1x, the signal is convolved with wavelets ψ_{λ_1} to obtain wavelet coefficients. Thereafter, modulus of these wavelet coefficients is computed and convolved with the low pass filter $\phi(t)$. This procedure can be repeated for any level m as shown in equation (5.7).

$$S_m x(t, \lambda_1, \cdots, \lambda_2) = ||x * \psi_{\lambda_1}| \cdots * \psi_{\lambda_m}| * \phi(t) \tag{5.7}$$

The extracted coefficients are essentially features, they are further processed before being utilized for training of ML algorithms. The resultant n scattering coefficients are denote as $[S_1, S_2, \cdots, S_n]$, where each scattering coefficient S_i represents a vector $[c_1^i, c_2^i, \cdots, c_l^i]$. Firstly, the norm of each scattering coefficient S_i is computed, which can be described as shown in equation (5.8). This operation results in a new set $[\|S_1\|, \|S_2\|, \cdots, \|S_n\|]$, where each $\|S_i\|$ is a scaler value that represents the norm of scattering coefficient S_i.

$$\|S_i\| = Norm(S_i) = \sum_{j=1}^{l} (c_j^i)^2 \tag{5.8}$$

The efficacy of the extracted scattering coefficients including the total number of scattering coefficients n and their size l, are driven by three critical parameters: (1) maximum order of scattering transform m_{max} (2) quality factor Q_m and (3) maximum log-scale parameter J. The maximum order of scattering transform m_{max} determines the depth of the transform and directly affects the total number of scattering coefficients. Quality factor Q_m represents the number of wavelet filters per octave in the filter bank ψ_{λ_m} at order m . For instance, the first order filter bank (ψ_{λ_1}) may use 8 wavelets per octave ($Q_1 = 8$). A higher value of Q_m implies high resolution frequency, more features and increased computation cost while the lower value of Q_m represents low resolution frequency analysis, fewer features and lower computation cost. The other parameter that requires proper consideration is a maximum log-scale parameter J, which determines the averaging scale $T = 2^J$ of the filter. Intuitively, the parameter determines the maximum size or width of the wavelets being used, higher value enables extraction of slower or low frequency variations, while a lower value leads to extraction of high frequency variations. Hence, optimization of parameter J for any problem is crucial to extract important features as well as to reduce computation cost. Even if the higher computational cost is not a barrier, the number of resultant scattering coefficients and their size affect the performance of a ML algorithm. For instance, sparse data may lead to overfitting, or failure in pattern learning. Hence, it is crucial to optimize these parameters while keeping ML algorithms in consideration. Therefore, the selection of parameters m_{max}, Q_m and J along with their impact on performance of ML algorithms is further discussed in the next section.

Step 3: Insulation Degradation Quantification using ML Algorithm

The insulation degradation level is quantified by utilizing the processed features from the previous step. This step involves feeding the processed feature set $[\|S_1\|, \|S_2\|, \cdots, \|S_n\|]$ into the pretrained ML algorithm f, parametrized by coefficients θ. This relation can be mathematically formulated as equation (5.9).

$$y = f([\|S_1\|, \|S_2\|, \cdots, \|S_n\|]\,; \theta) \tag{5.8}$$

Here, y represents the degradation level quantified by a pretrained ML algorithm f. Such quantification of insulation degradation allows efficient monitoring of insulation condition throughout the lifespan of the machine and hence appropriate maintenance actions, or preventive measures can be taken.

The performance of the ML model remains a key priority, hence the training and selection of appropriate ML algorithm is very crucial. Although any ML algorithm could be utilized, simpler ML algorithms are more preferred due to reduced computation requirements. The following section provides structured end-to-end framework for utilization of the proposed methodology.

5.2 Framework for Proposed Methodology

This section presents an end-to-end framework designed for developing insulation condition monitoring using the proposed ML based approach. Comprehensive overview provided on the processes involved, which includes data acquisition, data augmentation, feature extraction, ML Model training, and testing or deployment of ML model. The framework is provided in Fig. 5-3, it comprises two phases: the offline training phase and the online monitoring phase.

5.2.1.Offline Training Phase

During the offline training phase, the primary objective is to develop a well-trained ML model capable of quantifying insulation degradation with great accuracy. This phase includes the following processes.

Data Acquisition:

The requirement of data is a fundamental necessity for any ML model. As discussed, the proposed methodology relies on processing the HF line current (i_{line}) to quantify the insulation degradation level. Therefore, it is essential to obtain data on i_{line} and corresponding level of insulation degradation. Such data can be acquired through experiments or simulations.

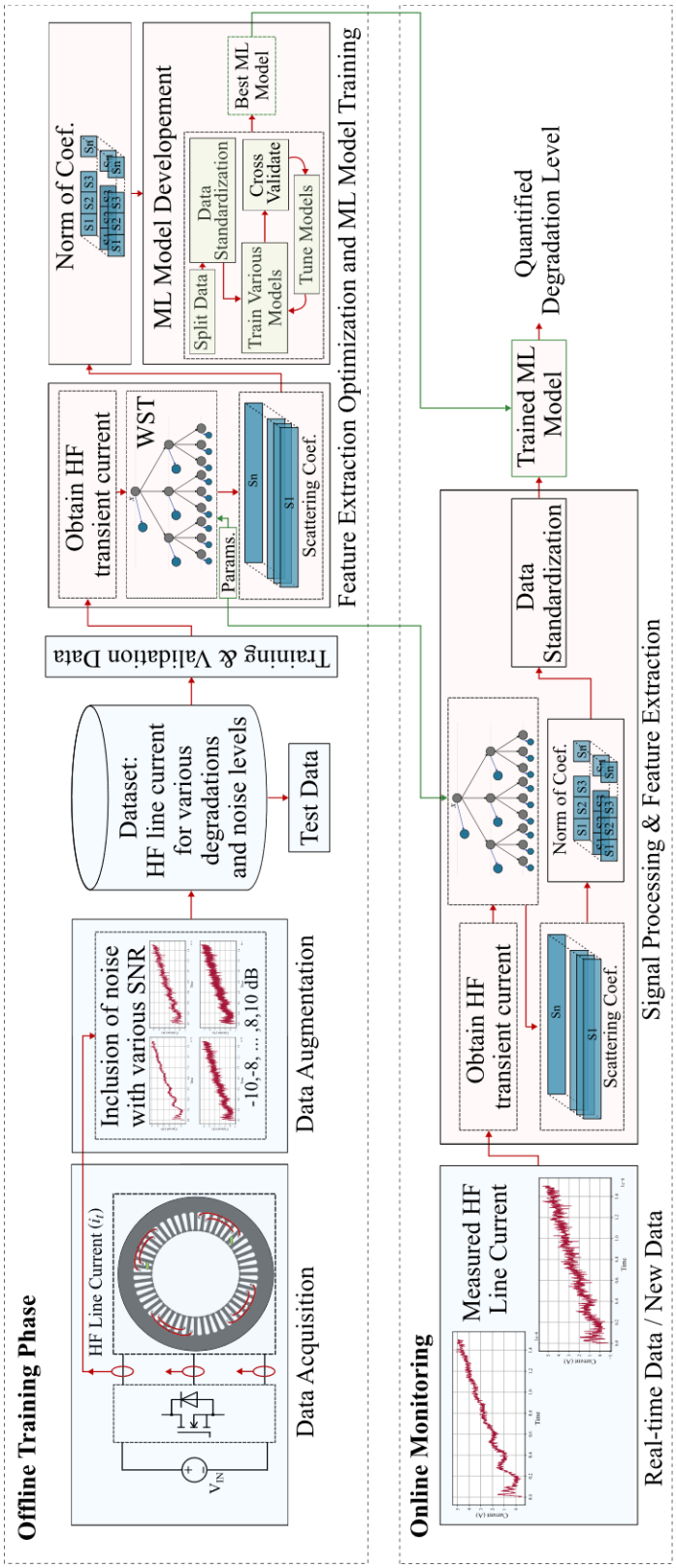

Fig. 5-3 End-to-end framework for the proposed methodology

For instance, a simulation based approach can be used where an HF stator winding model has been developed and utilized to obtain this data. To acquire data through an experiment, various insulation degradation scenarios can be emulated on a real motor and corresponding HF line current can be measured. Another experimental approach involves subjecting a stator winding to accelerated thermal aging, where in the HF line current can be obtained for varying numbers of thermal cycles or degradation levels. However, the winding gets permanently damaged in such process.

Data Augmentation:

The proposed methodology aims to quantify insulation degradations under varying levels on noise in i_t. Hence, it is important to ensure that the dataset contains all the variability expected within the ML model's scope of operation, including different degradation severities and noise levels. However, the acquired data lacks varying noise levels because the simulated data is free of noise and the hardware acquired data does not include varying levels of noise and degradation severities. Given the lack of such data, data augmentation is employed where noise is deliberately injected, in order to obtain line current signal with various signal-to noise (SNR) levels. Using such data augmentation, data is enriched with various noise levels, which is crucial for ML model training. The augmented dataset contains line currents signals for various degradations with varying SNR levels. This data can be divided into two subsets: 1) training and validation data, which is utilized for the training and performance validation of the ML model and 2) test data, which is to evaluate the performance of the finalized ML model on new data, ensuring its robustness and generalizability to unseen data. Although separate test data is not strictly required, it may play a important role in additional validation of the final ML model.

Feature Extraction Optimization and ML Model Training:

The primary objective of this step is to optimize feature extraction procedure and obtain a well-trained ML model that can be subsequently utilized for online monitoring stage to quantify insulation condition. Firstly, key steps 1) and 2) of the proposed methodology are employed for each data point in the augmented dataset to extract the feature set $[\|S_1\|, \|S_2\|, \cdots, \|S_n\|]$. The next step is to prepare the extracted features for the ML model. Firstly, standardization of each feature set in the data is performed. This process is shown in equation (5.10).

The standardization process which adjusts the features to have zero mean and unit variance, ensuring the same across all features.

$$S_{i,std} = \frac{S_i - \mu_i}{\sigma_i} \tag{5.10}$$

Here, S_i represents individual feature set, μ_i and σ_i represents mean and standard deviation over the feature set S_i in the data. The standardized data is further utilized for ML model development. However, the performance of the ML model gets affected by the extracted features. The effectiveness of extracted features depends on the WST parameters (m_{max}, Q_m, J), they affect the number of scattering coefficients and their size. Hence, the tuning of these parameters is directly linked to the ML model development. The ML model development phase comprises of training, parameter tuning and performance validation of various ML models. The best performing model is deemed to be most capable and further utilized for online condition monitoring. Although any ML model can be selected, the proposed approach works with even simpler algorithms like linear regression. Upon completion of this stage, optimal values of WST parameters (m_{max}, Q_m, J) are established, and trained ML model is ready for online monitoring.

5.2.2.Online Monitoring Phase

The stage involves online quantification of insulation condition using the pretrained ML model. Throughout the lifetime of the machine, the measured HF line current may indicate varying levels of degradation with inherent noise variability. This data undergoes the same feature extraction procedure described in steps 1) and 2) of the methodology. The values of WST parameters (m_{max}, Q_m, J) remains as finalized during the offline phase. Thereafter, as shown in step 3) of the proposed approach, the extracted features are further analyzed by the pretrained ML model to quantify insulation condition. Such quantification of insulation condition enables a safe operation of the machine through timely maintenance and fault preventive control.

5.3 Simulation-Based Validation and Results

This section presents the validation of the proposed methodology through simulation-based investigations. The proposed methodology and framework discussed in the previous sections have been followed and results have been presented. The data on HF line current for varying levels of degradation and noise have been acquired through simulation for validation. An HF model of the stator winding can be developed using multiconductor transmission line (MCTL) approach and utilized to obtain the data. This model uses ladder circuits for representing frequency dependent resistance and inductance of the winding, while capacitances are used to represent various insulation materials. The developed simulation model has been validated through experiments in prior work.

To acquire data, the developed HF model is utilized to simulate various insulation degradation cases. As discussed, various literature assert that the degradation causes an increase in the insulation capacitance, this increase can be up to 40-50%. Hence, to acquire data, this research work simulates degradations up to 40%, in increments of 0.5%. For each degradation scenario, a PWM voltage excitation pulse V_{PWM} of 500V amplitude is applied and corresponding i_t is obtained. The generated dataset comprises 80 distinct measurements of i_t, each representing a unique degradation scenario. However, this data lacks noisy variability.

In data augmentation stage, the initial dataset has been further processed to incorporate noise. For each datapoint in the dataset, random noise is added to obtain current signal with various SNR levels, ranging from -10 dB to 10 dB, in increments of 2 dB. For example, Fig. 5-4 shows

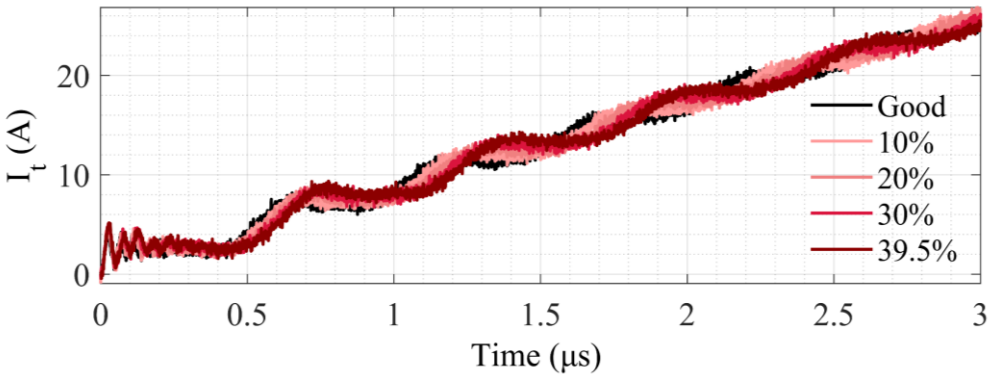

Fig. 5-4 Line current for various degradation scenarios (SNR: 10)

line current for various degradation scenarios for SNR=10 dB. It is important to ensure that the dataset covers the entire range of SNR levels. This augmentation of dataset significantly increases the size of initial dataset to 960 datapoints, each corresponding to a unique degradation scenario and noise level.

Following data augmentation, the next stage focuses on optimization of the feature extraction procedure and developing a well-trained ML model. As discussed, optimal selection of WST parameters (m_{max}, Q_m, J) and optimal ML model selection are interdependent. Hence, for various combinations of WST parameters, multiple ML models are trained and evaluated. To reduce the computational cost, deliberately simpler ML models have been selected including linear regression, lasso regression, elastic net and decision tree regression models. The performance of ML models is evaluated through k-fold cross validations to ensure robust validation and minimal bias in performance evaluation.

The influence of WST parameters on validation performance of decision tree regression model is shown in Fig. 5-5, and it shows that the minimum validation error obtained with parameters $m_{max} = 2, J = 11$ and $Q_m = 9$. Table 5.1 provides the summary on the validation performance of various ML models through various matrices like mean absolute error (MAE), mean squared error (MAE), coefficient of determination score (R^2). The decision tree regression model provides the best performance with the mean absolute error (MAE) of 0.65%. Nevertheless, other models also demonstrate great performance. For instance, the lasso regression model and elastic net regression models display similar performance, with MAE values of 1.25% and 1.31%. By analyzing such results, the optimal WST parameters and the best performing ML model is selected to be utilized for the online monitoring phase. Here, the WST parameters are determined to be $m_{max} = 2, J = 11$ and $Q_m = 9$, while the decision tree model is identified as optimal model for online monitoring phase.

In the online monitoring phase, the finalized ML model is deployed for real-time monitoring of insulation condition. The measured HF line current may represent any degradation level and noise level in it, which undergoes processing through the proposed approach, and the developed ML model processes these features to quantify the degradation level. Excellent validation results provide confidence in the proposed approach. However, to thoroughly test the approach, the developed model has been tested on an entirely new dataset which mimics the data in online

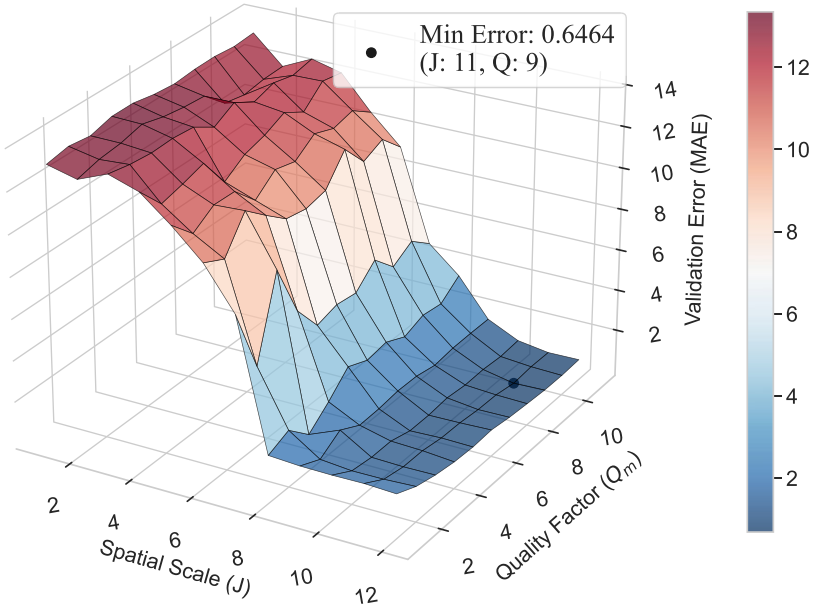

Fig. 5-5 Simulation Results: Validation error for decision tree model for various WST parameters (m_{max}=2)

Table 5-1 Simulation Results: Validation Performance Metrics of ML Models

ML Model	Mean Absolute Error (MAE)	Mean Squared Error (MSE)	R^2 Score
Linear Reg.	1.49	0.0422	0.9675
Lasso Reg.	1.25	0.0418	0.9586
Elastic Net Reg.	1.31	0.0449	0.9555
Decision Tree	0.64	0.0114	0.9912

monitoring phase. The test dataset comprises four test scenarios, each with a unique SNR level: -6.5, -2.5, 2.5, and 6.5 dB. Each test scenario contains 80 different HF line currents, each representing a unique degradation of up to 40%. So, the resultant test dataset comprises 320 unique HF line currents. As discussed, the decision tree model performed the best during the training and validation phase, and corresponding test results are summarized in Table 5.2. In Fig. 5-6, the predicted value of degradation by the decision tree model against the true degradation value, illustrating the error distribution for the test data. Each data point is in close proximity to the ground truth, indicating that the model achieves good performance with low mean error across the test data. Detailed performance metrics are shown in Table 5.2. Here, the 'overall' row presents the aggregated performance for the complete test data. All of the models performed

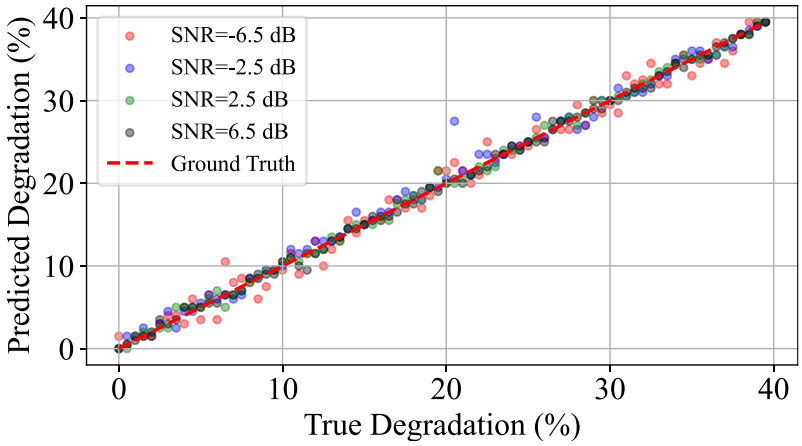

Fig. 5-6 Error distribution of predictions from the decision tree model

Table 5-2 Simulation Results: Performance Metrics of ML Models on Test Dataset

ML Model	Test Data	MAE	MSE	R^2 Score
Linear Reg.	SNR: 6.5	0.90	1.26	0.9906
	SNR: 2.5	1.31	2.50	0.9812
	SNR: -2.5	1.66	4.23	0.9683
	SNR: -6.5	2.12	6.44	0.9517
	Overall	1.50	3.61	0.9729
Lasso Reg.	SNR: 6.5	0.39	0.24	0.9982
	SNR: 2.5	0.74	0.96	0.9928
	SNR: -2.5	1.06	1.89	0.9858
	SNR: -6.5	1.41	3.04	0.9772
	Overall	0.90	1.53	0.9885
Elastic Net Reg.	SNR: 6.5	0.40	0.24	0.9982
	SNR: 2.5	0.72	0.91	0.9932
	SNR: -2.5	1.08	1.90	0.9857
	SNR: -6.5	1.40	3.01	0.9774
	Overall	0.90	1.51	0.9886
Decision Tree	SNR: 6.5	0.33	0.25	0.9981
	SNR: 2.5	0.46	0.37	0.9973
	SNR: -2.5	0.66	1.22	0.9909
	SNR: -6.5	1.00	1.61	0.9879
	Overall	0.61	0.86	0.9935

quite well. The linear regression model shows a quite good overall MAE of 1.50% and R^2 score of 0.9729. Moreover, the Lasso model and Elastic Net model perform slightly better, with overall MAEs of 0.9%. As expected from the validation results, the decision tree model performs comparatively better with the overall MAE of 0.61% and R^2 score of 0.9935. Nonetheless, all the models show a great capability in the quantification of insulation degradation, showcasing

the proposed approach's efficacy. The ability to quantify insulation degradation even in the presence of significant noise illustrates the robustness of the model and its suitability for real world applications with varying noise levels.

5.4 Experimental Validation and Results

5.4.1. Experimental Setup

This section explains the laboratory setup utilized to acquire data through experiments for validation of the proposed approach. As shown in Fig. 5-7, the setup contains a DC source, an inverter, a hairpin stator winding, degradation emulation PCBs, voltage probe, current probe, and an oscilloscope.

To emulate insulation degradation, commonly additional capacitors to the winding capacitors are connected to replicate the capacitance increase caused by insulation degradation. To emulate GW degradation, capacitors can be connected between winding to the ground while to emulate turn insulation degradation capacitors can be connected in parallel to the winding. This research work employs a similar emulation-based approach to acquire data on HF line current for varying levels of degradations. To accommodate emulation, the stator winding has been modified to have nine tapings on one of the phases and custom PCBs have been developed for insulation degradation emulation. The PCBs enable connection and disconnection of different ceramic capacitors between the taps. The location of the taps and connection of emulation PCBs are illustrated in Fig. 5-8. External capacitances C_{GW} are utilized to emulate GW degradation while C_{TT} are utilized to emulate turn insulation degradation.

As discussed, the insulation capacitance may increase up to about 40-50% due to degradation. Hence, data is acquired for 40 different scenarios, capacitance increase ranging from 0 to 39%, in increments of 1%. For each 1% increment in degradation, additional capacitances of 13.5 pF is connected to the tapings and the ground to emulate GW degradation by increasing the capacitance C_{GW}. Simultaneously, additional capacitance of 56 pF is connected between the taps to emulate each 1% turn insulation degradation by increasing the capacitance C_{TT}. To acquire i_t, Keysight 30MHz/300A HF Rogowski current probe and R&S RTM3004 500MHz oscilloscope have been utilized

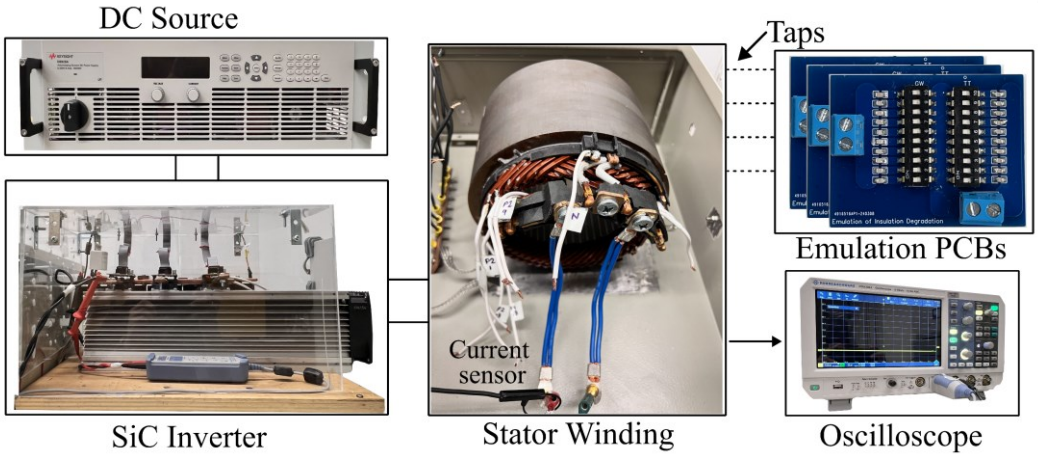

Fig. 5-7 Experimental setup

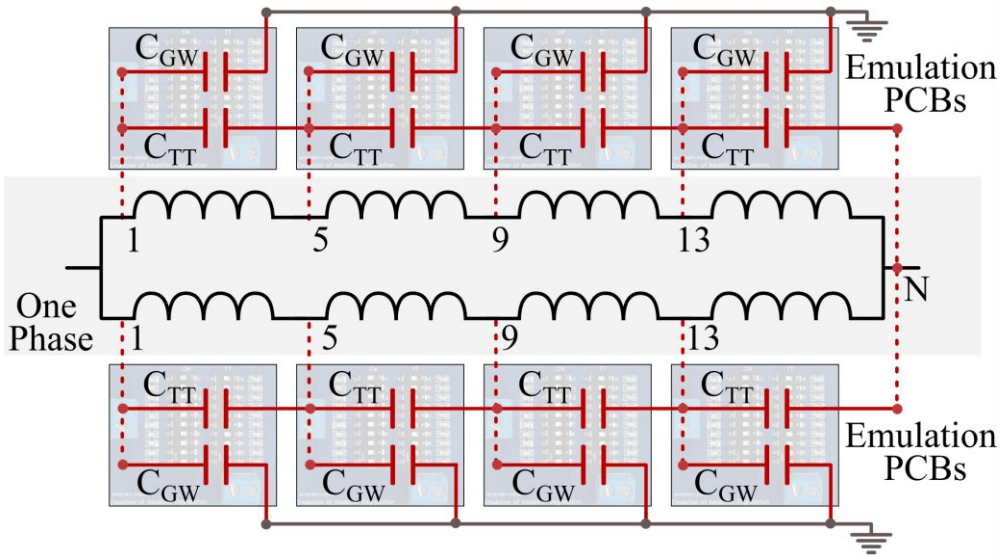

Fig. 5-8 Illustration of emulation of insulation degradation

5.4.2.Experimental Results and Discussions

The discussed experimental setup has been utilized to acquire data for validation of the proposed methodology. For each previously discussed degradation scenario, a PWM voltage excitation pulse V_{PWM} of 400V is applied to the winding and corresponding HF line current i_t is obtained. Hence, the dataset comprises 40 unique measurements of i_t. For this dataset, the proposed methodology and framework have been followed. The data augmentation process is the same as explained in the previous subsection. For each datapoint in the dataset, random noise is added with various SNR levels, ranging from -10 dB to 10 dB, in increments of 2 dB. Hence, the

augmentation of dataset contains 480 datapoints, each corresponding to a unique degradation scenario and noise level.

The next stage involves optimization of feature extraction and development of a well-trained ML model, this primarily involves optimal selection of WST parameters and ML model. This is achieved through evaluating multiple ML models for various combinations of WST parameters. The validation performance of ML models is evaluated using k-fold cross validation. Considered ML models are the same. The validation performance is summarized in Table 5.3. Similar to a previous study, the decision tree model shows the best performance with MAE of 0.65%, for WST parameters $m_{max} = 2$, $J = 13$ and $Q_m = 7$. Other ML models also show commendable performance with MAE lower than 1.5%. Considering the performance, the selected WST parameters are $m_{max} = 2$, $J = 13$ and $Q_m = 7$, and the decision tree model is selected as the optimal model for online monitoring phase.

Table 5-3 Experimental Results: Validation Performance Metrics of ML Models

ML Model	MAE	MSE	R^2 Score
Linear Reg.	1.38	0.0331	0.9738
Lasso Reg.	1.23	0.0266	0.9737
Elastic Net Reg.	1.35	0.0314	0.9689
Decision Tree	0.45	0.01	0.9922

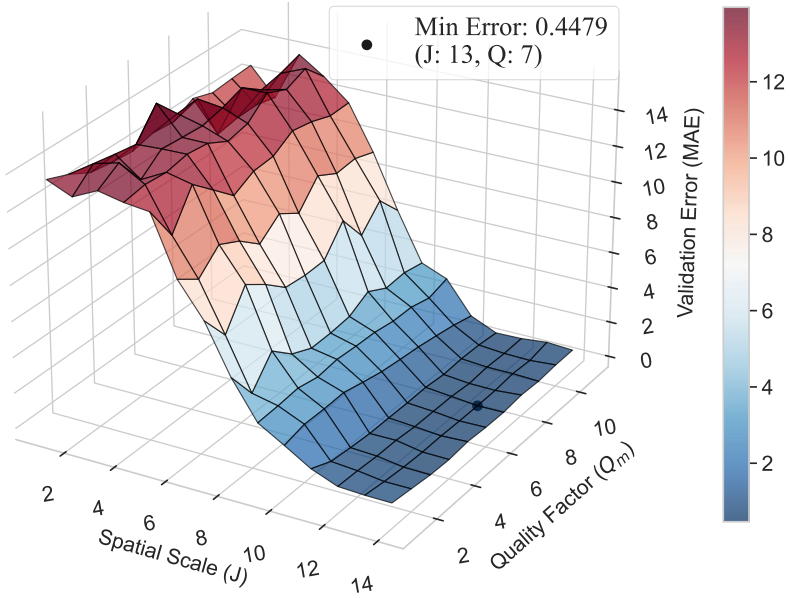

Fig. 5-9 Experimental Results: Validation error for decision tree model for various WST parameters (m_{max}=2)

Even though the validation performance is promising, the model has been tested on a completely new dataset comprising 160 unique HF line currents. The performance matrices of all models on the test dataset are summarized in Table 5.4. The test dataset includes four scenarios, each with unique SNR levels: -6.5, -2.5, 2.5, and 6.5 dB, comprising 40 unique line currents

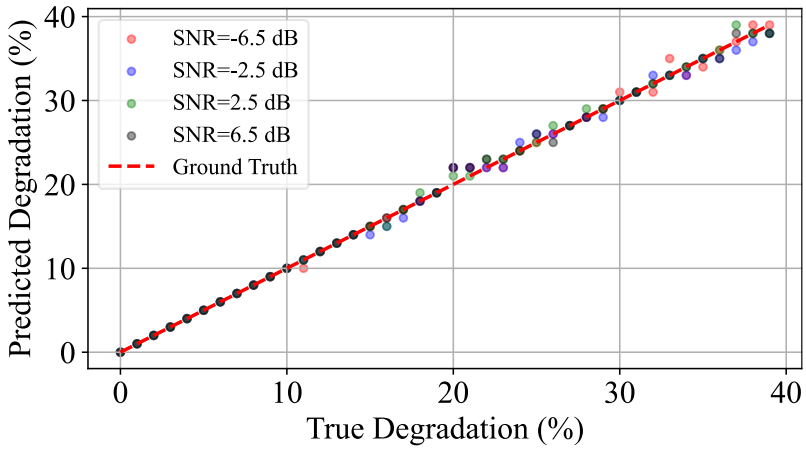

Fig. 5-10 Error distribution of predictions from the decision tree model

Table 5-4 Experimental Results: Performance Metrics of ML Models on Test Dataset

ML Model	Test Data	MAE	MSE	R^2 Score
Linear Reg.	SNR: 6.5	1.15	2.1717	0.9837
	SNR: 2.5	1.30	2.4909	0.9813
	SNR: -2.5	1.75	4.4853	0.9663
	SNR: -6.5	2.44	8.9497	0.9328
	Overall	**1.66**	**4.5244**	**0.9660**
Lasso Reg.	SNR: 6.5	0.75	0.9391	0.9930
	SNR: 2.5	0.80	1.0582	0.9921
	SNR: -2.5	0.97	1.4874	0.9888
	SNR: -6.5	1.23	2.2388	0.9832
	Overall	**0.93**	**1.4309**	**0.9893**
Elastic Net Reg.	SNR: 6.5	0.82	1.1275	0.9915
	SNR: 2.5	0.87	1.2402	0.9907
	SNR: -2.5	1.05	1.7115	0.9872
	SNR: -6.5	1.25	2.3258	0.9825
	Overall	**1.00**	**1.6012**	**0.9880**
Decision Tree	SNR: 6.5	0.23	0.2750	0.9979
	SNR: 2.5	0.23	0.2750	0.9979
	SNR: -2.5	0.40	0.4500	0.9966
	SNR: -6.5	0.30	0.4000	0.9970
	Overall	**0.29**	**0.3500**	**0.9974**

representing various degradation scenarios. The distribution of error for the decision tree model is shown in Fig. 5-10, the predicted values of degradation are in close proximity with the true values. As expected from the validation results, the decision tree model performs the best with an overall MAE of 0.29%, which is extremely accurate. As the noise level increases, the performance degrades, which is expected. In summary, these models show a great capability to handle varying noise levels, validating the proposed methodology and the framework.

5.5 Summary

This chapter proposed a data-driven methodology for quantification of insulation degradation using only HF line current. Moreover, the proposed methodology has a unique capability to quantify degradations under various noise levels in the measured signal. Measured HF line current is processed through wavelet scattering transform for feature extraction, these features are further fed into the trained ML algorithm to quantify degradation. A structured framework has been developed for the efficient implementation of the proposed method, which discusses data acquisition, data augmentation, feature extraction as well as training of ML algorithms. For validation of proposed approach, simulation and hardware based studies have been conducted, they utilize random wound and hairpin wound machines respectively. The simulation based study proves the efficacy of the opposed approach with a mean absolute error (MAE) of about 0.61% on a test dataset comprises 320 unique HF line current, each representing different degradation and noise level. Experimental results further validate the approach, achieving even better MAE of about 0.29% on test dataset comprising 160 datapoints. The results for different severities of degradations and different noise levels from two different studies not only prove the proposed approach's efficacy in quantification of insulation degradation but also its ability to handle different noise levels in the measured signal.

Chapter 6:Conclusions and Future Works

6.1 Conclusions

This Ph.D. thesis primarily focuses on the development of novel stator winding insulation condition monitoring methodologies. The main contributions and conclusions of this thesis are presented as follows.

In Chapter 1, the introduction to the insulation condition monitoring and literature review on the topic have been presented. In existing literature there exists mainly two types of insulation condition monitoring methodologies suitable where low cost and minimal complexity are paramount. There exist two different kind of methodologies that are especially suited for systems requiring low cost and minimal complexity: 1) leakage current measurement and 2) line current measurement based methodologies. Among these, line current measurement based methodologies are identified as the most suitable for practical applications. Thereafter, the research gaps and limitations of the existing literature are identified. Thereafter the problem statement, research objectives and the overall structure of the thesis are discussed.

In chapter 2, the primary focus is on the development of HF modeling of the stator winding for investigations on insulation condition monitoring. In this chapter, an MCTL based HF modeling model has been developed. The developed model considers frequency dependent resistances, inductances and mutual coupling between the turns. The modeling procedure and calculation of various parameters have been discussed in detail. The developed model is validated through comparison of simulated CM impedance, DM impedances and voltage distribution with actual measurements from hardware. The results show good match between simulation and hardware. The developed model is crucial for investigations on condition monitoring methodologies.

Chapter 3 addresses a limitation identified in the existing literature related to limited understanding on the influence of insulation degradations on HF line currents, CM impedance and DM impedance. Using the developed model in the previous chapter, this chapter conducts a detailed investigations of how various types of insulation degradation influence HF line currents and CM/DM impedances. Based on the investigations, it was found that the transient line current exhibits unique behavior characterized by initial high-frequency oscillations followed by lower-

frequency oscillations. These oscillations are directly linked to the antiresonance frequencies of the CM impedance, which can be reflective of insulation condition. Hence, the chapter proposes the utilization of prominent oscillations which are at antiresonance frequencies of CM impedance for condition monitoring.

In Chapter 4, a novel insulation condition monitoring technique has been proposed, which employs wavelet packet decomposition (WPD) to analyze HF line current and extract indicators for monitoring the state of health (SOH). Existing approaches fall short in simultaneous condition monitoring of TT and GW insulation. However, the proposed technique can provide the SOH indicators of TT and GW insulation simultaneously through the analysis of line current. The detailed steps for the utilization of the proposed approach have been discussed. The results have been validated through simulations and experiments. Overall, the investigation and the results conclude that the proposed method is robust and accurate for determining the SOH of TT and GW insulations simultaneously.

Chapter 5 presents a novel data-driven methodology for insulation condition monitoring, which utilizes a ML algorithm to analyze features extracted from HF line currents using wavelet scattering transform (WST). The proposed methodology has a unique capability to quantify degradations under various noise levels in the measured signal. A structured framework has been developed for the efficient implementation of the proposed method, which discusses data acquisition, data augmentation, feature extraction as well as training of ML algorithms. For validation of proposed approach, simulation and hardware based studies have been conducted, studies show great mean absolute error of about 0.61% in simulation based study and 0.29% in experiments. The results proved the methodology's ability to effectively quantify different severities of insulation degradation under various noise levels.

6.2 Future Works

Chapter 2 focused on the development of HF modeling of the stator winding for investigations on insulation condition monitoring. In this chapter, an MCTL based HF modeling model has been developed and validated. Some discrepancies between the simulation and hardware and simulation have been discussed. These discrepancies can be due to the unknown position of wires inside the slot, approximation of dielectric properties of insulation, negligence of nonidealities, negligence of frequency dependent end-winding modeling, core loss

representation, etc. As part of the future work, investigations and efforts should aim to address these discrepancies to improve the accuracy of the HF model. Improved model can lead to more reliable and accurate investigations on condition monitoring methodologies.

Chapter 3 presents investigations on the influence of TT and GW insulation degradations on the CM impedance, DM impedance and HF line current. Thereafter, it emphasizes on the potential utilization of the HF line current oscillations for monitoring insulation condition. The investigations have been conducted under assumption of uniform degradation in the winding. However, future research can explore more complex scenarios and anomaly conditions to gain deeper insights into insulation degradation mechanisms. For instance, investigations on scenarios where only a few specific turns of the winding exhibit higher degradation compared to other locations in the winding.

Chapter 4 and chapter 5 presents novel insulation condition monitoring methodologies. The proposed methodologies have been validated through emulating insulation degradation. The emulation of insulation degradation is not completely accurate and may not represent actual degradation with great accuracy, which can be addressed. As part of the future work, the approaches can be further validated for real insulation degradation scenarios caused by thermal exposure. Moreover, the methodology can be further investigated for its suitability for real world application, where in the influence of various factors, such as operating conditions, temperature, current sensor performance, influence of the rotor and complex aging scenarios can be investigated. Currently, due to limited hardware capability, the methodology has been validated through processing data offline. As part of the future work, the methodology can be validated through online implementation. Additionally, the on the proposed methodologies can be investigated to reduce computation cost. For instance, the limitations data drive approach is that it requires more computational resources due to the high number of features and the application of the wavelet scattering transform (WST) for feature extraction. Potential future work may focus on reducing these computational resources through feature reduction techniques or simplifying feature extraction. Addressing aforementioned aspects will enhance the reliability and applicability of the proposed method.

References

[1]International Energy Agency, *Global EV Outlook 2023: Catching up with Climate Ambitions*. in Global EV Outlook. OECD, 2023. doi: 10.1787/cbe724e8-en.

[2]Trasport Canada, “Zero-emission vehicles,Accessed: Jun. 07, 2024. [Online]. Available: https://tc.canada.ca/en/road-transportation/innovative-technologies/zero-emission-vehicles

[3]“Financial assistance for a new electric vehicle,”. Accessed: Jun. 07, 2024. [Online]. Available: https://www.quebec.ca/en/transports/electric-transportation/financial-assistance-electric-vehicle/new-vehicle

[4]N. R. Canada, “Updated Projections of Canada’s Public Charging Infrastructure Needs.” Accessed: Jun. 07, 2024. [Online]. Available: https://natural-resources.canada.ca/energy-efficiency/transportation-alternative-fuels/resource-library/updated-projections-canadas-public-charging-infrastructure-needs/24504

[5]“Technical Feature: The Porsche Taycan,” Porsche Newsroom. Accessed: Jun. 08, 2024. [Online]. Available: https://newsroom.porsche.com/en_AU/2021/products/technical-feature-the-porsche-taycan-23670.html

[6]J. Hong *et al.*, “Thermal Runaway Prognosis of Battery Systems Using the Modified Multiscale Entropy in Real-World Electric Vehicles,” *IEEE Trans. Transp. Electrification*, vol. 7, no. 4, pp. 2269–2278, Dec. 2021, doi: 10.1109/TTE.2021.3079114.

[7]S. Dey, S. Mohon, P. Pisu, and B. Ayalew, “Sensor Fault Detection, Isolation, and Estimation in Lithium-Ion Batteries,” *IEEE Trans. Control Syst. Technol.*, vol. 24, no. 6, pp. 2141–2149, Nov. 2016, doi: 10.1109/TCST.2016.2538200.

[8]S. Dey, H. E. Perez, and S. J. Moura, “Model-Based Battery Thermal Fault Diagnostics: Algorithms, Analysis, and Experiments,” *IEEE Trans. Control Syst. Technol.*, vol. 27, no. 2, pp. 576–587, Mar. 2019, doi: 10.1109/TCST.2017.2776218.

[9]X. Hu, K. Zhang, K. Liu, X. Lin, S. Dey, and S. Onori, “Advanced Fault Diagnosis for Lithium-Ion Battery Systems: A Review of Fault Mechanisms, Fault Features, and Diagnosis Procedures,” *IEEE Ind. Electron. Mag.*, vol. 14, no. 3, pp. 65–91, Sep. 2020, doi: 10.1109/MIE.2020.2964814.

[10]Z. Wang, C. Song, L. Zhang, Y. Zhao, P. Liu, and D. G. Dorrell, “A Data-Driven Method for Battery Charging Capacity Abnormality Diagnosis in Electric Vehicle Applications,” *IEEE Trans. Transp. Electrification*, vol. 8, no. 1, pp. 990–999, Mar. 2022, doi: 10.1109/TTE.2021.3117841.

[11]B. Guan and X. Zhen, “Noninvasive Online Capacitor Monitoring Method for Three-Level Converter Based on Active Neutral-Point Current Adjustment,” *IEEE Trans. Ind. Electron.*, vol. 71, no. 5, pp. 4320–4329, May 2024, doi: 10.1109/TIE.2023.3283714.

[12]X.-S. Pu, T. H. Nguyen, D.-C. Lee, K.-B. Lee, and J.-M. Kim, “Fault Diagnosis of DC-Link Capacitors in Three-Phase AC/DC PWM Converters by Online Estimation of Equivalent Series Resistance,” *IEEE Trans. Ind. Electron.*, vol. 60, no. 9, pp. 4118–4127, Sep. 2013, doi: 10.1109/TIE.2012.2218561.

[13]B. Gou, Y. Xu, Y. Xia, Q. Deng, and X. Ge, “An Online Data-Driven Method for Simultaneous Diagnosis of IGBT and Current Sensor Fault of Three-Phase PWM Inverter in Induction Motor Drives,” *IEEE Trans. Power Electron.*, vol. 35, no. 12, pp. 13281–13294, Dec. 2020, doi: 10.1109/TPEL.2020.2994351.

[14]Z. Gao, C. Cecati, and S. X. Ding, “A Survey of Fault Diagnosis and Fault-Tolerant Techniques—Part I: Fault Diagnosis With Model-Based and Signal-Based Approaches,” *IEEE Trans. Ind. Electron.*, vol. 62, no. 6, pp. 3757–3767, Jun. 2015, doi: 10.1109/TIE.2015.2417501.

[15]A. Choudhary, S. Fatima, and B. K. Panigrahi, “State-of-the-Art Technologies in Fault Diagnosis of Electric Vehicles: A Component-Based Review,” *IEEE Trans. Transp. Electrification*, vol. 9, no. 2, pp. 2324–2347, Jun. 2023, doi: 10.1109/TTE.2022.3209166.

[16]G. Niu, X. Dong, and Y. Chen, “Motor Fault Diagnostics Based on Current Signatures: A Review,” *IEEE Trans. Instrum. Meas.*, vol. 72, pp. 1–19, 2023, doi: 10.1109/TIM.2023.3285999.

[17]I. Zamudio-Ramirez, R. A. Osornio-Rios, J. A. Antonino-Daviu, H. Razik, and R. Romero-Troncoso, “Magnetic Flux Analysis for the Condition Monitoring of Electric Machines: A Review,” *IEEE Trans. Ind. Inform.*, vol. 18, no. 5, pp. 2895–2908, May 2022, doi: 10.1109/TII.2021.3070581.

[18]W. Lang, Y. Hu, C. Gong, X. Zhang, H. Xu, and J. Deng, “Artificial Intelligence-Based Technique for Fault Detection and Diagnosis of EV Motors: A Review,” *IEEE Trans. Transp. Electrification*, vol. 8, no. 1, pp. 384–406, Mar. 2022, doi: 10.1109/TTE.2021.3110318.

[19]“Report of Large Motor Reliability Survey of Industrial and Commercial Installations, Part I,” *IEEE Trans. Ind. Appl.*, vol. IA-21, no. 4, pp. 853–864, 1985, doi: 10.1109/TIA.1985.349532.

[20]“Report of Large Motor Reliability Survey of Industrial and Commercial Installations, Part II,” *IEEE Trans. Ind. Appl.*, vol. IA-21, no. 4, pp. 865–872, 1985, doi: 10.1109/TIA.1985.349533.

[21]“Report of Large Motor Reliability Survey of Industrial and Commercial Installations: Part 3,” *IEEE Trans. Ind. Appl.*, vol. IA-23, no. 1, pp. 153–158, Jan. 1987, doi: 10.1109/TIA.1987.4504880.

[22]Y. Xing *et al.*, “Fluorinated PEEK and XLPE as Promising Insulation Candidates for the Propulsion System of All-electric Aircraft,” *IEEE Trans. Dielectr. Electr. Insul.*, pp. 1–1, 2022, doi: 10.1109/TDEI.2022.3157899.

[23]C. Liu, X. Zheng, M. Yin, and X. Cheng, “Design of high thermal conductivity insulation adhesive (H-class) for low voltage motor,” *IEEE Trans. Dielectr. Electr. Insul.*, vol. 23, no. 4, pp. 1907–1914, Aug. 2016, doi: 10.1109/TDEI.2016.7556461.

[24]Z. Lei *et al.*, “Surface modified nano-SiO 2 enhances dielectric properties of stator coil insulation for HV motors,” *IEEE Trans. Dielectr. Electr. Insul.*, vol. 27, no. 3, pp. 1029–1037, Jun. 2020, doi: 10.1109/TDEI.2020.008736.

[25]M. R. Khowja, G. Vakil, S. S. Ahmad, R. Ramanathan, C. Gerada, and M. Benarous, “Life Characterization of PEEK and Nanofilled Enamel Insulated Wires Under Thermal Ageing,” *IEEE Access*, vol. 12, pp. 39470–39483, 2024, doi: 10.1109/ACCESS.2024.3374637.

[26]T. A. Huynh and M.-F. Hsieh, “Improvement of Traction Motor Performance for Electric Vehicles Using Conductors With Insulation of High Thermal Conductivity Considering Cooling Methods,” *IEEE Trans. Magn.*, vol. 57, no. 2, pp. 1–5, Feb. 2021, doi: 10.1109/TMAG.2020.3021127.

[27]P. Giangrande, V. Madonna, S. Nuzzo, and M. Galea, “Moving Toward a Reliability-Oriented Design Approach of Low-Voltage Electrical Machines by Including Insulation Thermal Aging Considerations,” *IEEE Trans. Transp. Electrification*, vol. 6, no. 1, pp. 16–27, Mar. 2020, doi: 10.1109/TTE.2020.2971191.

[28]X. Zhou, P. Giangrande, Y. Ji, W. Zhao, S. Ijaz, and M. Galea, “Insulation for Rotating Low-Voltage Electrical Machines: Degradation, Lifetime Modeling, and Accelerated Aging Tests,” *Energies*, vol. 17, no. 9, p. 1987, Apr. 2024, doi: 10.3390/en17091987.

[29]Greg C. Stone; Ian Culbert; Edward A. Boulter; Hussein Dhirani, "Evaluating Insulation Materials and Systems," in Electrical Insulation for Rotating Machines: Design, Evaluation, Aging, Testing, and Repair, IEEE, 2014.

[30]“Advanced Insulation and Wire Wrap Systems for 800V+ Next Gen E-Motors | IEEE Resource Center.” Accessed: Jun. 08, 2024. [Online]. Available: https://resourcecenter.ieee.org/education/webinars/iesweb0250

[31]T. Petri, M. Keller, and N. Parspour, “The Insulation Resilience of Inverter-Fed Low Voltage Traction Machines: Review, Challenges, and Opportunities,” *IEEE Access*, vol. 10, pp. 104023–104049, 2022, doi: 10.1109/ACCESS.2022.3210348.

[32]X. Hu, J. Han, X. Tang, and X. Lin, “Powertrain Design and Control in Electrified Vehicles: A Critical Review,” *IEEE Trans. Transp. Electrification*, vol. 7, no. 3, pp. 1990–2009, Sep. 2021, doi: 10.1109/TTE.2021.3056432.

[33]M. Ghassemi, “Accelerated insulation aging due to fast, repetitive voltages: A review identifying challenges and future research needs,” *IEEE Trans. Dielectr. Electr. Insul.*, vol. 26, no. 5, pp. 1558–1568, Oct. 2019, doi: 10.1109/TDEI.2019.008176.

[34]I. Aghabali, J. Bauman, P. J. Kollmeyer, Y. Wang, B. Bilgin, and A. Emadi, “800-V Electric Vehicle Powertrains: Review and Analysis of Benefits, Challenges, and Future Trends,” *IEEE Trans. Transp. Electrification*, vol. 7, no. 3, pp. 927–948, Sep. 2021, doi: 10.1109/TTE.2020.3044938.

[35]T. Adamson *et al.*, “An 800-V High-Density Traction Inverter—Electro-Thermal Characterization and Low-Inductance PCB Bussing Design,” *IEEE J. Emerg. Sel. Top. Power Electron.*, vol. 10, no. 3, pp. 3013–3023, Jun. 2022, doi: 10.1109/JESTPE.2020.3042211.

[36]“Ajedium™ PEEK Slot liners reduce eMotor length(-13% for stack length), decrease stator/rotor mass (-6.3%), & improve eMotor efficiency (2.1 %) vs NKN | LinkedIn.” Accessed: Jun. 10, 2024. [Online]. Available: https://www.linkedin.com/pulse/ajedium-peek-slot-liners-reduce-emotor-length-13-stack-brian-baleno/

[37]“Failures in Three-Phase Stator Windings.” Accessed: Jun. 10, 2024. [Online]. Available: https://easa.com/resources/failures-in-three-phase-stator-windings

[38]K. Gyftakis, M. Sumislawska, D. Kavanagh, D. Howey, and M. McCulloch, “Dielectric Characteristics of Electric Vehicle Traction Motor Winding Insulation under Thermal Ageing,” *IEEE Trans. Ind. Appl.*, pp. 1–1, 2015, doi: 10.1109/TIA.2015.2495296.

[39]S. Diaham, M.-L. Locatelli, and T. Lebey, “Improvement of Polyimide Electrical Properties During Short-Term of Thermal Aging,” in *2008 Annual Report Conference on Electrical Insulation and Dielectric Phenomena*, Quebec City, QC, Canada: IEEE, Oct. 2008, pp. 79–82. doi: 10.1109/CEIDP.2008.4772840.

[40]T. K. Saha, M. Darveniza, Z. T. Yao, D. J. T. Hill, and G. Yeung, “Investigating the effects of oxidation and thermal degradation on electrical and chemical properties of power transformers insulation,” *IEEE Trans. Power Deliv.*, vol. 14, no. 4, pp. 1359–1367, Oct. 1999, doi: 10.1109/61.796229.

[41]M. Farahani, E. Gockenbach, H. Borsi, K. Schafer, and M. Kaufhold, “Behavior of machine insulation systems subjected to accelerated thermal aging test,” *IEEE Trans. Dielectr. Electr. Insul.*, vol. 17, no. 5, pp. 1364–1372, Oct. 2010, doi: 10.1109/TDEI.2010.5595537.

[42]P. A. Panagiotou, K. N. Gyftakis, N. Lophitis, M. D. McCulloch, and D. A. Howey, “Investigation of traction motor windings’ insulation capacitance at switching frequencies under accelerated thermal stress,” in *2017 IEEE 11th International Symposium on Diagnostics for Electrical Machines, Power Electronics and Drives (SDEMPED)*, Tinos, Greece: IEEE, Aug. 2017, pp. 537–543. doi: 10.1109/DEMPED.2017.8062407.

[43]“IEC 60034-18-21:2012 | IEC Webstore.” Accessed: Jun. 11, 2024. [Online]. Available: https://webstore.iec.ch/publication/112

[44]“IEEE Standard Test Procedure for Thermal Evaluation of Systems of Insulating Materials for Random-Wound AC Electric Machinery.” IEEE. doi: 10.1109/IEEESTD.2016.7466454.

[45]Y. Ji, P. Giangrande, W. Zhao, V. Madonna, H. Zhang, and M. Galea, “Determination of Hotspot Temperature Margin for Rectangular Wire Windings Considering Insulation Thermal Degradation and Partial Discharge,” *IEEE Trans. Transp. Electrification*, vol. 10, no. 1, pp. 2057–2069, Mar. 2024, doi: 10.1109/TTE.2023.3283393.

[46]Y. Ji, P. Giangrande, W. Zhao, V. Madonna, H. Zhang, and M. Galea, “Determination of Hotspot Temperature Margin for Rectangular Wire Windings Considering Insulation Thermal Degradation and Partial Discharge,” *IEEE Trans. Transp. Electrification*, vol. 10, no. 1, pp. 2057–2069, Mar. 2024, doi: 10.1109/TTE.2023.3283393.

[47]V. Grau and R. W. De Doncker, “The Effects of Steep Voltage Slopes on Insulation Systems of Coil Windings caused by Next Generation Power Semiconductor Devices,” in *2019 IEEE Electrical Insulation Conference (EIC)*, Calgary, AB, Canada: IEEE, Jun. 2019, pp. 26–29. doi: 10.1109/EIC43217.2019.9046515.

[48]G. L. Skibinski, R. J. Kerkman, and D. Schlegel, “EMI emissions of modern PWM AC drives,” *IEEE Ind. Appl. Mag.*, vol. 5, no. 6, pp. 47–80, Dec. 1999, doi: 10.1109/2943.798337.

[49]“IEC 60034-18-41:2014 | IEC Webstore.” Accessed: Jun. 11, 2024. [Online]. Available: https://webstore.iec.ch/publication/118

[50]Y. Xie, J. Zhang, F. Leonardi, A. R. Munoz, and M. W. Degner, “Investigation of Surge Voltage Propagation in Inverter-Driven Electric Machine Windings,” *IEEE Trans. Ind. Electron.*, vol. 70, no. 10, pp. 9811–9822, Oct. 2023, doi: 10.1109/TIE.2022.3220863.

[51]Y. Xie, J. Zhang, F. Leonardi, A. Munoz, M. Degner, and F. Liang, “Voltage Stress Modeling and Measurement for Random-Wound Machine Windings Driven by Inverters,” *IEEE Trans. Ind. Appl.*, pp. 1–1, 2020, doi: 10.1109/TIA.2020.2986184.

[52]Y. Xie, J. Zhang, F. Leonardi, A. R. Munoz, M. W. Degner, and F. Liang, “Voltage Stress Modeling and Measurement for Random-Wound Windings Driven by Inverters,” in *2019 IEEE International Electric Machines & Drives Conference (IEMDC)*, San Diego, CA, USA: IEEE, May 2019, pp. 1917–1924. doi: 10.1109/IEMDC.2019.8785133.

[53]S. Sundeep, J. Wang, A. Griffo, and F. Alvarez-Gonzalez, “Antiresonance Phenomenon and Peak Voltage Stress Within PWM Inverter Fed Stator Winding,” *IEEE Trans. Ind. Electron.*, vol. 68, no. 12, pp. 11826–11836, Dec. 2021, doi: 10.1109/TIE.2020.3048286.

[54]S. Sundeep, J. Wang, and A. Griffo, “Prediction of Transient Voltage Distribution in Inverter-fed Stator Winding, Considering Mutual Couplings in Time Domain,” in *2020 IEEE Energy Conversion Congress and Exposition (ECCE)*, Detroit, MI, USA: IEEE, Oct. 2020, pp. 517–524. doi: 10.1109/ECCE44975.2020.9235981.

[55]W. R. Finley, C. A. Wilson, and R. R. Burke, “Storage of electric motors,” in *Conference Record of 1995 Annual Pulp and Paper Industry Technical Conference*, Vancouver, BC, Canada: IEEE, 1995, pp. 74–81. doi: 10.1109/PAPCON.1995.404849.

[56]M. Ariannik, A. A. Razi-Kazemi, and M. Lehtonen, “Effect of cumulative moisture content on degradation of transformer paper insulation,” *IEEE Trans. Dielectr. Electr. Insul.*, vol. 24, no. 1, pp. 611–618, Feb. 2017, doi: 10.1109/TDEI.2016.006006.

[57]J. Botts and R. Wolford, “Water Immersion Testing of Form-Wound Coil Insulation,” *IEEE Trans. Electr. Insul.*, vol. EI-4, no. 3, pp. 77–82, Sep. 1969, doi: 10.1109/TEI.1969.299062.

[58]T. Kumazawa, M. Oishi, and M. Todoki, “High-humidity deterioration and internal structure change of epoxy resin for electrical insulation,” *IEEE Trans. Dielectr. Electr. Insul.*, vol. 1, no. 1, pp. 133–138, Feb. 1994, doi: 10.1109/94.300240.

[59]R. Soltani, E. David, and L. Lamarre, “Impact of humidity on dielectric response of rotating machines insulation system,” *IEEE Trans. Dielectr. Electr. Insul.*, vol. 17, no. 5, pp. 1479–1488, Oct. 2010, doi: 10.1109/TDEI.2010.5595549.

[60]Y. Ji *et al.*, “Partial Discharge Investigation Under Humidity Conditions via Dissipation Factor and Insulation Capacitance Tip-Up Test,” *IEEE Trans. Dielectr. Electr. Insul.*, vol. 29, no. 4, pp. 1483–1490, Aug. 2022, doi: 10.1109/TDEI.2022.3171197.

[61]Y. Ji *et al.*, “Investigation on Humidity Effect on Partial Discharge Considering Thermal Aging,” in *2022 International Conference on Electrical Machines (ICEM)*, Valencia, Spain: IEEE, Sep. 2022, pp. 2325–2330. doi: 10.1109/ICEM51905.2022.9910815.

[62]P. Neti *et al.*, “Online detection of endwinding contamination in industrial motors,” in *2011 Electrical Insulation Conference (EIC).*, Annapolis, MD: IEEE, Jun. 2011, pp. 265–270. doi: 10.1109/EIC.2011.5996159.

[63]I. Tsyokhla, A. Griffo, and J. Wang, “Online Condition Monitoring for Diagnosis and Prognosis of Insulation Degradation of Inverter-Fed Machines,” *IEEE Trans. Ind. Electron.*, vol. 66, no. 10, pp. 8126–8135, Oct. 2019, doi: 10.1109/TIE.2018.2885740.

[64]F. Niu *et al.*, “An Online Groundwall Insulation Monitoring Method Based on Transient Characteristics of Leakage Current for Inverter-Fed Motors,” *IEEE Trans. Power Electron.*, vol. 37, no. 8, pp. 9745–9753, Aug. 2022, doi: 10.1109/TPEL.2022.3157571.

[65]D. Zheng and P. Zhang, “An Online Groundwall and Phase-to-Phase Stator Insulation Monitoring Method for Inverter-Fed Machine,” *IEEE Trans. Ind. Electron.*, vol. 68, no. 6, pp. 5303–5313, Jun. 2021, doi: 10.1109/TIE.2020.2988218.

[66]D. Zheng, G. Lu, and P. Zhang, “A Noninvasive Interturn Insulation Condition Monitoring Method Based on the Common-Mode Impedance Spectrum of Inverter-Fed Machines,” *IEEE Trans. Ind. Appl.*, vol. 57, no. 5, pp. 4786–4795, Sep. 2021, doi: 10.1109/TIA.2021.3094176.

[67]D. Zheng, G. Lu, Y. Wu, Q. Zhang, and P. Zhang, “Online Detection and Classification of Interturn and Groundwall Insulation Aging Based on Broadband Common-Mode Impedance Spectrum,” *IEEE Trans. Ind. Electron.*, vol. 71, no. 3, pp. 3142–3153, Mar. 2024, doi: 10.1109/TIE.2023.3265024.

[68]W. R. Jensen, E. G. Strangas, and S. N. Foster, “A Method for Online Stator Insulation Prognosis for Inverter-Driven Machines,” *IEEE Trans. Ind. Appl.*, vol. 54, no. 6, pp. 5897–5906, Nov. 2018, doi: 10.1109/TIA.2018.2854408.

[69]P. Zhang, K. Younsi, and P. Neti, “A novel online stator ground-wall insulation monitoring scheme for inverter-fed AC motors,” in *2013 IEEE Energy Conversion Congress and Exposition*, Denver, CO, USA: IEEE, Sep. 2013, pp. 3541–3547. doi: 10.1109/ECCE.2013.6647167.

[70]K. Younsi *et al.*, “On-line capacitance and dissipation factor monitoring of AC stator insulation,” *IEEE Trans. Dielectr. Electr. Insul.*, vol. 17, no. 5, pp. 1441–1452, Oct. 2010, doi: 10.1109/TDEI.2010.5595545.

[71]P. Nussbaumer, M. A. Vogelsberger, and T. M. Wolbank, “Induction Machine Insulation Health State Monitoring Based on Online Switching Transient Exploitation,” *IEEE Trans. Ind. Electron.*, vol. 62, no. 3, pp. 1835–1845, Mar. 2015, doi: 10.1109/TIE.2014.2361114.

[72]C. Zoeller, M. A. Vogelsberger, R. Fasching, W. Grubelnik, and T. M. Wolbank, “Evaluation and Current-Response-Based Identification of Insulation Degradation for High Utilized Electrical Machines in Railway Application,” *IEEE Trans. Ind. Appl.*, vol. 53, no. 3, pp. 2679–2689, May 2017, doi: 10.1109/TIA.2017.2661718.

[73]H. Li, Y. Gu, D. Xiang, P. Zhang, P. Yue, and Y. Cui, “Online Condition Monitoring of Line-End Coil Insulation for Inverter-Fed Machine by Switching Oscillation Mode Decomposition,” *IEEE Trans. Ind. Electron.*, vol. 69, no. 11, pp. 11697–11708, Nov. 2022, doi: 10.1109/TIE.2021.3120491.

[74]D. Xiang, H. Li, H. Yan, Y. Zheng, N. Zhao, and B. Liu, “Online Monitoring of Incipient Turn Insulation Degradation for Inverter-Fed Machine Using Sensitive Tail Component in PWM Switching Oscillations,” *IEEE Trans. Power Electron.*, vol. 36, no. 8, pp. 8730–8742, Aug. 2021, doi: 10.1109/TPEL.2021.3049809.

[75]G. Zanuso and L. Peretti, “Evaluation of High-Frequency Current Ringing Measurements for Insulation Health Monitoring in Electrical Machines,” *IEEE Trans. Energy Convers.*, vol. 37, no. 4, pp. 2637–2644, Dec. 2022, doi: 10.1109/TEC.2022.3182364.

[76]G. Zanuso and L. Peretti, “Accelerated Aging Procedure and Online Method for Stator Insulation Monitoring of Induction Motors,” *IEEE Trans. Energy Convers.*, vol. 38, no. 1, pp. 685–692, Mar. 2023, doi: 10.1109/TEC.2022.3214061.

[77]R. Leuzzi, V. G. Monopoli, L. Rovere, F. Cupertino, and P. Zanchetta, “Analysis and Detection of Electrical Aging Effects on High-Speed Motor Insulation,” *IEEE Trans. Ind. Appl.*, vol. 55, no. 6, pp. 6018–6025, Nov. 2019, doi: 10.1109/TIA.2019.2929013.

[78]R. E. Adjaye and K. J. Cornick, “Distribution of switching surges in the line-end coils of cable-connected motors,” *IEE J. Electr. Power Appl.*, vol. 2, no. 1, pp. 11–21, Feb. 1979, doi: 10.1049/ij-epa.1979.0002.

[79]M. Toudji, G. Parent, S. Duchesne, and P. Dular, “Determination of Winding Lumped Parameter Equivalent Circuit by Means of Finite Element Method,” *IEEE Trans. Magn.*, vol. 53, no. 6, pp. 1–4, Jun. 2017, doi: 10.1109/TMAG.2017.2671423.

[80]V. Mihaila, S. Duchesne, and D. Roger, “A simulation method to predict the turn-to-turn voltage spikes in a PWM fed motor winding,” *IEEE Trans. Dielectr. Electr. Insul.*, vol. 18, no. 5, pp. 1609–1615, Oct. 2011, doi: 10.1109/TDEI.2011.6032831.

[81]F. Perisse, P. Werynski, and D. Roger, “A New Method for AC Machine Turn Insulation Diagnostic Based on High Frequency Resonances,” *IEEE Trans. Dielectr. Electr. Insul.*, vol. 14, no. 5, pp. 1308–1315, Oct. 2007, doi: 10.1109/TDEI.2007.4339494.

[82]Yifan Tang, “Analysis of steep-fronted voltage distribution and turn insulation failure in inverter-fed form-wound AC motor,” *IEEE Trans. Ind. Appl.*, vol. 34, no. 5, pp. 1088–1096, Oct. 1998, doi: 10.1109/28.720449.

[83]P. Bidan, T. Lebey, G. Montseny, and J. Saint-Michel, “Transient voltage distribution in inverter fed motor windings: experimental study and modeling,” *IEEE Trans. Power Electron.*, vol. 16, no. 1, pp. 92–100, Jan. 2001, doi: 10.1109/63.903993.

[84]G. Suresh, H. A. Toliyat, D. A. Rendusara, and P. N. Enjeti, “Predicting the transient effects of PWM voltage waveform on the stator windings of random wound induction motors,” *IEEE Trans. Power Electron.*, vol. 14, no. 1, pp. 23–30, Jan. 1999, doi: 10.1109/63.737589.

[85]O. Magdun, A. Binder, A. Rocks, and O. Henze, “Prediction of common mode ground current in motors of inverter-based drive systems,” in *2007 International Aegean Conference on Electrical Machines and Power Electronics*, Bodrum, Turkey: IEEE, Sep. 2007, pp. 806–811. doi: 10.1109/ACEMP.2007.4510552.

[86]Y. Xie, J. Zhang, F. Leonardi, A. R. Munoz, M. W. Degner, and F. Liang, “Modeling and Verification of Electrical Stress in Inverter-Driven Electric Machine Windings,” *IEEE Trans. Ind. Appl.*, vol. 55, no. 6, pp. 5818–5829, Nov. 2019, doi: 10.1109/TIA.2019.2937068.

[87]Y. Xie, J. Zhang, F. Leonardi, A. Munoz, M. Degner, and F. Liang, “Voltage Stress Modeling and Measurement for Random-Wound Machine Windings Driven by Inverters,” *IEEE Trans. Ind. Appl.*, pp. 1–1, 2020, doi: 10.1109/TIA.2020.2986184.

[88]Y. Xie, J. Zhang, F. Leonardi, A. R. Munoz, and M. W. Degner, “Investigation of Surge Voltage Propagation in Inverter-Driven Electric Machine Windings,” *IEEE Trans. Ind. Electron.*, vol. 70, no. 10, pp. 9811–9822, Oct. 2023, doi: 10.1109/TIE.2022.3220863.

[89]C. Petrarca, A. Maffucci, V. Tucci, and M. Vitelli, “Analysis of the Voltage Distribution in a Motor Stator Winding Subjected to Steep-Fronted Surge Voltages by Means of a Multiconductor Lossy Transmission Line Model,” *IEEE Trans. Energy Convers.*, vol. 19, no. 1, pp. 7–17, Mar. 2004, doi: 10.1109/TEC.2003.821834.

[90]S. Sundeep, J. Wang, A. Griffo, and F. Alvarez-Gonzalez, “Antiresonance Phenomenon and Peak Voltage Stress Within PWM Inverter Fed Stator Winding,” *IEEE Trans. Ind. Electron.*, vol. 68, no. 12, pp. 11826–11836, Dec. 2021, doi: 10.1109/TIE.2020.3048286.

[91]D. A. Hewitt, S. Sundeep, J. Wang, and A. Griffo, “High Frequency Modeling of Electric Machines Using Finite Element Analysis Derived Data,” *IEEE Trans. Ind. Electron.*, vol. 71, no. 2, pp. 1432–1442, Feb. 2024, doi: 10.1109/TIE.2023.3260357.

[92]S. Sundeep, J. Wang, and A. Griffo, “Holistic Modeling of High-Frequency Behavior of Inverter-Fed Machine Winding, Considering Mutual Couplings in Time Domain,” *IEEE Trans. Ind. Appl.*, vol. 57, no. 6, pp. 6044–6057, Nov. 2021, doi: 10.1109/TIA.2021.3105954.

[93]G. Lupo, C. Petrarca, M. Vitelli, and V. Tucci, “Multiconductor transmission line analysis of steep-front surges in machine windings,” *IEEE Trans. Dielectr. Electr. Insul.*, vol. 9, no. 3, pp. 467–478, Jun. 2002, doi: 10.1109/TDEI.2002.1007711.

[94]M. K. Hussain and P. Gomez, “Optimized dielectric design of stator windings from medium voltage induction machines fed by fast front pulses,” *IEEE Trans. Dielectr. Electr. Insul.*, vol. 24, no. 2, pp. 837–846, Apr. 2017, doi: 10.1109/TDEI.2017.006249.

[95]A. Patel, “Modeling and Detection of Stator Winding Insulation Degradation in VSI-fed Electric Machines Under High dv/dt”.

[96]S. Sundeep “Peak Voltage Stress in Inverter-Fed Machines and its Mitigation Measures” Accessed: Jun. 11, 2024. [Online]. Available: https://etheses.whiterose.ac.uk/31941/

[97]Ansys Inc. (Version 2023R2) “Maxwell Help.pdf.”

[98]Synflex Elektro GmbH “SynWire type 180, Copper Wire, round, enamelled, self bonding” Accessed: Jun. 11, 2024. [Online]. Available: https://www.synflex.com/en/product-range/winding/synwire-winding-wire/detail/synwire-type-180-copper-wire-round-enamelled-self-bonding-321/

[99]V. Madonna, P. Giangrande, W. Zhao, H. Zhang, C. Gerada, and M. Galea, “Electrical Machines for the More Electric Aircraft: Partial Discharges Investigation,” *IEEE Trans. Ind. Appl.*, vol. 57, no. 2, pp. 1389–1398, Mar. 2021, doi: 10.1109/TIA.2020.3046434.

[100]S. Savin, S. Ait-Amar, and D. Roger, “Turn-to-turn capacitance variations correlated to PDIV for AC motors monitoring,” *IEEE Trans. Dielectr. Electr. Insul.*, vol. 20, no. 1, pp. 34–41, Feb. 2013, doi: 10.1109/TDEI.2013.6451339.

[101]“Wire Testing: NEMA, ASTM or IEC Standards Wire Testing From Eltek,” ELTEK International Laboratories. Accessed: Jun. 18, 2024. [Online]. Available: https://elteklabs.com/test-capabilities/material-tests/wire-testing/

[102]A. Boglietti, A. Cavagnino, and M. Lazzari, “Experimental High-Frequency Parameter Identification of AC Electrical Motors,” *IEEE Trans. Ind. Appl.*, vol. 43, no. 1, pp. 23–29, 2007, doi: 10.1109/TIA.2006.887313.

[103]J. Anden and S. Mallat, “Deep Scattering Spectrum,” *IEEE Trans. Signal Process.*, vol. 62, no. 16, pp. 4114–4128, Aug. 2014, doi: 10.1109/TSP.2014.2326991.

[104]H. Li, Y. Gu, D. Xiang, P. Zhang, P. Yue, and Y. Cui, “Online Condition Monitoring of Line-End Coil Insulation for Inverter-Fed Machine by Switching Oscillation Mode Decomposition,” *IEEE Trans. Ind. Electron.*, vol. 69, no. 11, pp. 11697–11708, Nov. 2022, doi: 10.1109/TIE.2021.3120491.

[105]D. Zheng, G. Lu, and P. Zhang, “An Improved Online Stator Insulation Monitoring Method Based on Common-Mode Impedance Spectrum Considering the Effect of Aging Position,” *IEEE Trans. Ind. Appl.*, vol. 58, no. 3, pp. 3558–3566, May 2022, doi: 10.1109/TIA.2022.3160131.

[106]D. Xiang, H. Li, H. Yan, Y. Zheng, N. Zhao, and B. Liu, “Online Monitoring of Incipient Turn Insulation Degradation for Inverter-Fed Machine Using Sensitive Tail Component in PWM Switching Oscillations,” *IEEE Trans. Power Electron.*, vol. 36, no. 8, pp. 8730–8742, Aug. 2021, doi: 10.1109/TPEL.2021.3049809.

[107]Sang Bin Lee, Jinkyu Yang, K. Younsi, and R. M. Bharadwaj, “An online groundwall and phase-to-phase insulation quality assessment technique for AC-machine stator windings,” *IEEE Trans. Ind. Appl.*, vol. 42, no. 4, pp. 946–957, Jul. 2006, doi: 10.1109/TIA.2006.876077.